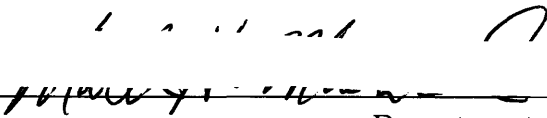


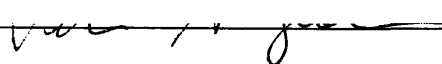
**SHORT WAVELENGTH LASER GAIN STUDIES  
IN PLASMAS PRODUCED BY  
A SMALL ND:GLASS SLAB LASER**

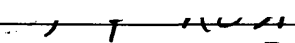
**Martin Heinrich Muendel**  
A.B., Princeton University (1986)

Submitted to the Department of Physics  
in partial fulfillment of  
the requirements for the degree of Doctor of Philosophy  
at the Massachusetts Institute of Technology

February 1994

Signature of Author   
Department of Physics  
January 7, 1994

Certified by   
Professor Peter L. Hagelstein  
Thesis supervisor

Accepted by   
Professor George F. Koster  
Chairman, Physics Graduate Committee

MASSACHUSETTS INSTITUTE  
OF TECHNOLOGY

FEB 08 1994

LIBRARY

©1994 Martin Heinrich Muendel. All rights reserved.

The author hereby grants to MIT permission to reproduce and to distribute publicly paper and electronic copies of this thesis document in whole or in part.

# SHORT WAVELENGTH LASER GAIN STUDIES IN PLASMAS PRODUCED BY A SMALL ND:GLASS SLAB LASER

Martin Heinrich Muedel

Submitted in February 1994 in partial fulfillment of the requirements  
for the degree of Doctor of Philosophy in Physics  
at the Massachusetts Institute of Technology

## ABSTRACT

A high-power, high-repetition-rate Nd:glass laser system was developed and used to study a collisionally pumped x-ray laser scheme near 200 Å. The laser system used a commercial oscillator injecting 60-psec modelocked pulses at 1053 nm into a Nd:glass zig-zag slab amplifier which was developed for this project. The amplifier was capable of producing 2-J, near-diffraction-limited pulses at repetition rates of up to 0.3 Hz. Single-pass gains of up to 7.5 were measured with storage efficiencies of 3-4%, and the gain profile was flat to within 10%. Use of air cooling and subhertz repetition rates alleviated thermal distortion, stringent coolant channel sealing requirements, and optical surface degradation. An optical system was designed which incorporated flattop rectangular beams and relay imaging to generate 15- $\mu\text{m}$ -wide, uniform line foci on the target.

The focused laser radiation was used to generate linear plasma columns suitable for amplified-spontaneous-emission laser output near 200 Å. An electron collisionally pumped scheme in Ni-like Nb, analogous to previously demonstrated Ni-like schemes at higher  $Z$ , was investigated experimentally. A solid Nb target was irradiated with modelocked trains of pump pulses; a gain at 204 Å of about  $5\text{ cm}^{-1}$  in a length of 3 mm at pump energies of 1.1 J/pulse was inferred from experiments in which the line focus length was varied. Comparable amounts of gain were seen following the second and third pump pulses, suggesting that an x-ray cavity might be feasible using this pumping scheme. Supporting evidence for gain was observed in the angular and temporal dependence of the emission. The measured gain was low compared to predictions, and the pump laser power appeared therefore to have been insufficient to achieve a high gain-length product.

Theoretical work supporting the experimental efforts included calculation of ionization and recombination rate coefficients, development of a hydrodynamics model for the plasma cooling phase between pulses, and study of the extension of nonlinear four-wave-mixing and tripling processes to the soft x-ray regime.

Thesis supervisor: Associate Professor Peter L. Hagelstein



# Acknowledgments

I wish to thank for their contributions to this thesis the following people: my advisor, Peter Hagelstein; the past and present members of the x-ray laser group, including Santanu Basu, Michele Bierbaum, John Paul Braud, Mary Ellen Butts, Ike Chuang, Kevin Delin, Cris Eugster, Marc Fleury, James Goodberlet, Sumanth Kaushik, Lisbeth Lauritzen, Deborah Manning, Ann Morgenthaler, Janet Pan, Tim Savas, and Dan Tauber; the members of the MIT Optics and FEL groups; the personnel of the LLNL Laser Program, particularly Mike Perry, Mike Campbell, Kim Budil, and Frank Patterson; Professor Louis Smullin; my thesis readers, Professors Michael Feld and David Pritchard; and my parents, family and friends for inspiration and encouragement.

I also wish to acknowledge the National Science Foundation, the Newport Research Corporation, and the SPIE for graduate fellowship support, as well as the DOE, Lincoln Laboratories, LLNL, and NRL for funding or supporting the laboratory effort.



# Contents

<b>1</b>	<b>Introduction</b>	<b>11</b>
1.1	X-ray laser overview . . . . .	11
1.2	Overview of this thesis . . . . .	13
1.3	Notes on terminology . . . . .	14
<b>2</b>	<b>Pump laser architecture</b>	<b>17</b>
2.1	Pulsed laser physics overview . . . . .	18
2.2	Selection of laser materials . . . . .	23
2.3	Laser architecture . . . . .	25
2.4	Repetition rate considerations; use of slab amplifier . . . . .	28
<b>3</b>	<b>Modelocked/<math>Q</math>-switched oscillator and preamplifier</b>	<b>31</b>
3.1	Oscillator . . . . .	31
3.2	Active modelocking theory . . . . .	35
3.3	$Q$ -switch dynamics . . . . .	38
3.4	Observed oscillator performance . . . . .	40
3.5	Preamplifier . . . . .	41
<b>4</b>	<b>Zig-zag slab amplifier</b>	<b>45</b>
4.1	Introduction . . . . .	45
4.2	Overall layout . . . . .	47
4.3	Slab geometry . . . . .	47
4.4	Slab fabrication . . . . .	49
4.5	Parasitics . . . . .	49
4.6	Flashlamps and electrical system . . . . .	52
4.7	Pump cavity design . . . . .	54
4.8	Thermal design and performance . . . . .	56
4.9	Mechanical construction . . . . .	58
4.10	Gain and storage efficiency measurements . . . . .	61

<b>5</b>	<b>Optical system</b>	<b>63</b>
5.1	Overview . . . . .	63
5.2	Non-gaussian beam propagation . . . . .	65
5.3	Cylindrical focusing optic . . . . .	71
<b>6</b>	<b>Collisionally excited x-ray laser theory overview</b>	<b>75</b>
6.1	Collisionally excited schemes . . . . .	75
6.2	Results from x-ray laser gain model . . . . .	86
6.3	Overview of relevant plasma physics . . . . .	87
6.4	Pump light absorption . . . . .	90
6.5	Electron temperature during pump pulse . . . . .	93
6.6	Target configuration . . . . .	98
6.7	Ionization balance . . . . .	101
<b>7</b>	<b>One-dimensional hydrodynamics model</b>	<b>107</b>
7.1	Background and assumptions . . . . .	107
7.2	Hydrodynamic equations . . . . .	110
7.3	Simulation code . . . . .	113
7.4	Analytic expressions for $N(R)$ and $V(R)$ . . . . .	115
7.5	Results and discussion . . . . .	117
<b>8</b>	<b>Experimental studies</b>	<b>127</b>
8.1	Introduction . . . . .	127
8.2	Instrumentation and diagnostics . . . . .	128
8.3	Spectroscopy . . . . .	132
8.4	Gain studies . . . . .	142
8.5	Discussion . . . . .	154
<b>9</b>	<b>Nonlinear x-ray conversion in plasmas</b>	<b>157</b>
9.1	Introduction . . . . .	157
9.2	Basic equations . . . . .	161
9.3	Scaling relations . . . . .	162
9.4	Matrix elements . . . . .	166
9.5	Numerical evaluation for Na-like K . . . . .	167
9.6	Phase matching . . . . .	172
9.7	Conversion of 155 Å laser by FWM and tripling . . . . .	174
9.8	Conclusion . . . . .	179
<b>10</b>	<b>Conclusion</b>	<b>181</b>
10.1	Results of this thesis . . . . .	181
10.2	Future directions . . . . .	182



<b>Bibliography</b>	<b>187</b>
<b>A Flashlamp driver circuit schematics</b>	<b>193</b>
<b>Biographical note</b>	<b>199</b>



# Chapter 1

## Introduction

### 1.1 X-ray laser overview

The study of x-ray lasers has been pursued since the 1960's with the goal of extending to the soft x-ray regime many of the techniques and applications of current visible and ultraviolet lasers. A practical x-ray laser would be useful in areas where current laser sources have met the diffraction limit, such as microscopy, holography, and lithography, as well as in other areas with specific wavelength requirements, such as spectroscopy, photoelectron studies, and materials science.

To date, x-ray lasers have been demonstrated only in the laboratory and only at relatively modest output levels [1]. Because the x-ray laser concepts have been proven valid, however, there has been heightened interest recently in demonstrating a compact, inexpensive x-ray laser suitable for research or commercial applications—a tool rather than a research topic in itself. This thesis and the other efforts in our group are devoted to the development of such an x-ray laser.

Of the various approaches to x-ray lasers, the electron-collisional excitation

pumped scheme has had the greatest success in developing high gain-length products and has in fact been driven into saturation [2]. The lasing medium in this scheme is a high-temperature, high-density plasma; the upper laser state is radiatively metastable and is pumped by electron-ion collisions, whereas the lower laser state experiences rapid radiative decay, leading to an inversion.

To date, all electron-collisional pumped experiments at other institutions have used very highly stripped ions and consequently very high energy pump sources (typically lasers designed for inertial confinement fusion). One of the first x-ray lasers to be demonstrated, for example, was in collisionally pumped Ne-like Se in 1984 at 206 Å, using the Lawrence Livermore National Laboratory's Nova laser at one kJ pump energy [3]. Since then, similar x-ray lasers have been demonstrated at both lower pump energies and shorter wavelengths, but the energies remain above about 100 J. Since pump lasers of this class are multi-million-dollar devices, and because they typically have cool-down times between shots of many minutes to several hours, they are unlikely to yield x-ray lasers of sufficiently low cost and high repetition rate to serve as practical laboratory tools.

Our group's goal, therefore, has been to demonstrate gain in a collisionally pumped plasma using a small, lower intensity pump laser with a high repetition rate, which would be within our means—and those of other small laboratories—in cost and complexity. A given x-ray laser scheme may be scaled to lower pump intensity by decreasing the atomic number  $Z$  of the ion. This should in principle reduce the pump energy from several kJ to several J, at the cost of increasing the x-ray laser wavelength from around 50 Å to around 200 Å. While other groups have investigated the downscaling of other laser schemes, our work is the first attempt to scale the collisionally pumped scheme to dramatically lower pump energies.

## 1.2 Overview of this thesis

This thesis concerns two related projects: the development of a high-power, high-repetition-rate Nd:glass laser system, and the use of that system to study collisionally pumped x-ray laser gain near 200 Å.

Most of the laser development effort was devoted to the construction of a large Nd:glass zig-zag slab amplifier. This device represents the state of the art in high-peak-power, high-repetition-rate amplifiers. The use of this amplifier gives our laser system a higher repetition rate by an order of magnitude than comparable systems. The system generates up to 2 J in 60 psec pulses at several shots per minute.

The x-ray laser effort involved both experimental and analytical studies. Analytical and numerical models were developed for the plasma expansion and the ionization balance. Laser-produced plasmas were studied with a soft x-ray spectrometer, and measurements of stimulated gain were made. A gain of about  $5 \text{ cm}^{-1}$  was measured for a plasma column of length 3 mm.

Chapters 2-5 describe the development of the laser system. Chapter 2 is largely a summary of some design issues in high-peak-power solid-state lasers and of the methodology by which the present laser architecture was chosen. Chapter 3 addresses the design of the Nd:YLF oscillator and preamplifier. Chapter 4 discusses the development of the high-power Nd:glass slab amplifier system, and Chapter 5 summarizes the optical system design.

Chapters 6-8 discuss the x-ray laser studies that were undertaken. Chapter 6 gives a qualitative description of the collisional x-ray laser mechanism, then presents some analyses of the laser-plasma interaction and the plasma dynamics. Chapter 7 contains a model of the plasma expansion and cooling. Chapter 8 describes the experimental apparatus and the relevant spectroscopy, then discusses the experimental results.

Chapter 9 is a theoretical analysis of four-wave mixing schemes for frequency converting an x-ray laser. This work was undertaken as an exercise through which to learn how processes currently useful in the visible might scale to the soft x-ray regime. Schemes for frequency tripling and near-doubling are presented; specific examples are evaluated for input wavelengths in the 150-200 Å range.

### 1.3 Notes on terminology

Some conventions and background information should be explained:

1. Temperatures and energies are expressed in eV, and x-ray wavelengths in Å; all other units are cgs.
2. Ionic charge states are indicated by their isoelectronic sequence; thus, “Ni-like Nb” is used, rather than “Nb XIV” or “thirteen-times ionized niobium.” This is done because the isoelectronic sequence (i.e. the number of electrons remaining on the ion) is much more relevant to the ionic energy level structure than is the number of electrons that have been removed.
3. The filling order of the periodic table changes when moderately high ionization stages are reached; all subshells of a principal quantum number are filled before the next principal quantum number is begun. Thus, the plasma analogs of the closed-shell noble gases become He-like, Ne-like, Ni-like, and Nd-like. Analogous of the alkali metals (single electron outside a closed shell) are Li-like, Na-like, Cu-like, and Pr-like.
4. Various forms of the ionic charge are used at different times.  $Z$  is taken, in general, to be the actual number of protons in the nucleus.  $Z_c$  is the

ion charge state, i.e. the number of electrons that have been removed.

$Z_{\text{eff}}$  is an effective charge felt by the valence electron; it models the partial charge screening by the inner electrons.

5. The expression “x-ray laser” is used loosely; technically, 200 Å is considered part of the extreme ultraviolet, and 100 Å demarcates the beginning of the soft x-ray regime. It has become common usage to refer to lasers involving highly stripped ions as x-ray lasers.
6. The Nd:glass laser is often referred to as the “pump laser,” although strictly speaking, the upper x-ray laser state is pumped by electron collisions, and the Nd:glass laser should be called a “driver laser.”
7. The expression  $\overline{3d}$  indicates a hole in an otherwise closed  $3d$  shell, i.e. a  $3d^9$  configuration.





# Chapter 2

## Pump laser architecture

The pump laser system consists of a  $Q$ -switched/modelocked Nd:YLF oscillator, a double-pass Nd:glass or Nd:YLF preamplifier, and a large triple-pass Nd:glass slab power amplifier. The considerations that entered this design are discussed in this chapter. Details on these components and the optical system will be given in the following chapters.

The requirements for the laser system were determined by the x-ray laser physics (Chapter 6). The desired output is a train of up to 5 mode-locked pulses spaced by several nanoseconds; the specific requirements are listed in Table 2.1 together with the achieved system performance.

	Requirement	Achieved
Energy per pulse	1 J	2 J
Pulse duration	100 psec	60-120 psec
Interpulse time	5-10 nsec	7.5 nsec
Beam quality ( $\times$ diff lim)	$\sim 2\times$	$\sim 2\times$
Repetition rate	0.1 Hz	0.03 Hz

Table 2.1: Laser system requirements and achieved performance. The repetition rate is to be increased to 0.3 Hz.

## 2.1 Pulsed laser physics overview

The general theory of high energy pulsed laser amplification in four level solid state media is useful in understanding the design of the pump laser. Some aspects of this topic are summarized here; more exhaustive treatments are found in Koechner [4] and Brown [5].

### Time scales and gain formulation

Relevant time scales are as follows:

$$\tau_{F,u} = \text{fluorescence decay time of upper laser state} \sim 100\text{-}500 \mu\text{sec}$$

$$W_p^{-1} = \text{inverse pumping rate} \sim \tau_{F,u} \text{ typically}$$

$$\tau_{F,l} = \text{fluorescence decay time of lower laser state} \sim 1\text{-}10 \text{ nsec}$$

$$\tau_p = \text{laser pulse duration} \sim \text{nsec to psec} (\sim 10\text{-}100 \text{ psec for our system})$$

The inverse pumping rate is typically chosen to be comparable to the upper level decay time, because pumping at a lower rate is inefficient due to fluorescence losses, and pumping at a higher rate demands unnecessarily high peak powers from the pumping source (flashlamps, diode arrays, etc.). Both of these times are taken to be large compared with the pulse duration, so that pumping and fluorescence do not have an appreciable effect on the upper level population during the laser pulse.

The lower level lifetime is important because it determines whether bottlenecking will occur as the laser medium saturates. If the pulse duration is long compared with the lower level lifetime, then the lower state population remains essentially zero throughout the pulse and the full energy stored in the upper laser state can be extracted. If the pulse duration is short, the lower state will fill up during the pulse, reducing the gain; less stored energy can be extracted.

The small signal gain coefficient  $\alpha$  is proportional to the stored energy density in the upper laser state:

$$\alpha = \beta E_{st} \text{ [cm}^{-1}\text{]}$$

where  $\beta$  is the specific gain, typically expressed in  $[\text{cm}^{-1}/\text{J}/\text{cm}^3]$ , which is related to the stimulated emission cross section  $\sigma$  by

$$\beta = \sigma/h\nu.$$

The saturation fluence can be defined as

$$E_s = \frac{h\nu}{\gamma\sigma} = \frac{1}{\gamma\beta} \text{ [J}/\text{cm}^2\text{]}$$

where  $\gamma$  is the bottlenecking parameter, equal to one for long pulses  $\tau_p \gg \tau_{F,l}$  and equal to two for short pulses  $\tau_p \ll \tau_{F,l}$ , under the assumption of equal degeneracies of the upper and lower levels. Often in the literature, the specific gain is specified by its reciprocal, the long-pulse saturation fluence.

Following the derivation of Frantz and Nodvik [6], the pulse energy gain can be found to be

$$G = \frac{E_s}{E_{in}} \ln \left( 1 + (e^{E_{in}/E_s} - 1)e^{\alpha\ell} \right)$$

for an amplifier of pumped length  $\ell$  and input fluence  $E_{in}$ . This expression is valid from small signals up to full saturation. The limiting cases are, for small signal gain,

$$G = G_0 = e^{\alpha\ell},$$

valid while  $G_0 E_{in} \ll E_s$ , and for full saturation,

$$G = 1 + \left( \frac{E_s}{E_{in}} \right) \alpha\ell,$$

valid while  $E_{in} \gg E_s$ .

## ASE and parasitic lasing

The specific gain (or equivalently the long-pulse saturation fluence) turns out to characterize the energy storage capacity of laser media as well as their gain. Typically the energy storage is limited by the onset of amplified spontaneous emission (ASE) and parasitic lasing. ASE denotes the single-pass amplification of upper state fluorescence photons, which causes stored energy to be used up in this amplification and so appears as a gradual gain-dependent gain reduction. The severity of ASE is strongly dependent upon the lasing geometry because it depends on the expectation value of the gain-length product (hence the number of stimulated photon emissions) of a ray starting from a random point in the medium and emitted in a random direction. Clearly long, thin media (e.g. rods) are preferable to short, bulky media (thick disks or slabs).

Parasitic lasing occurs when ASE rays reflected internally off the lasing surfaces, or externally off mounting fixtures, pump cavities, optics, etc., experience enough gain to offset reflective losses and hence continue to propagate indefinitely, saturating the gain medium. The onset of parasitics is typically sudden, and the amplifier gain is seen to clamp sharply at some level. Parasitics are also very dependent upon geometry and additionally upon the reflectivity and nature of the lasing medium surfaces. Fine-ground surfaces are probably somewhat better than polished surfaces in avoiding parasitics, but the fact that they scatter the ASE strangely does not in itself defeat parasitics: the path of the parasitic ray need not be well-defined and closed upon itself, but need merely keep going for a large number of traversals. Better are refractive index-matched boundaries that effectively couple ASE out of the lasing to be absorbed externally. Coolant water ( $n = 1.33$ ) and water-ethylene glycol solutions ( $n = 1.38$ ) in contact with the lasing index-match much better than air or gas, and they have an absorption coefficient of around  $0.2 \text{ cm}^{-1}$  around

a wavelength of 1  $\mu\text{m}$ . Also, absorbing glasses can be glued on unused lasant surfaces with essentially perfect index matching, thus completely eliminating ASE rays from those surfaces.

In practice, it has been found that laser rods in flooded cavities can reach single-pass small signal gains in the range of about 50-100. Less advantageous geometries with large polished surfaces such as disks or slabs typically clamp at single-pass gains of 5-10.

The small-signal gain and hence the energy storage capacity are therefore limited by these processes. If the gain clamps at  $G_c$ , the maximum stored energy density  $E_{st}$  is given by

$$E_{st}\ell = \ln G_c/\beta = E_s \ln G_c \sim \begin{cases} E_s \times 2 & \text{for disks or slabs} \\ E_s \times 4 & \text{for rods} \end{cases}$$

Thus, low-gain materials are preferable in applications where high energy storage is desirable (e.g. high energy amplifiers). High-gain materials are more useful in low-energy oscillators, where they will offer a low lasing threshold. Typical values of  $E_{st}$  are up to 0.5-1.0 J/cm<sup>3</sup> in Nd:glass lasers and up to around 0.1 J/cm<sup>3</sup> in small Nd-doped crystalline lasers.

## Self-focusing

An important constraint on high power laser design is that imposed by small-scale self-focusing, in which third-order self-phase-modulation of the laser beam causes intensity-dependent phase disturbances. This effect causes small intensity perturbations to grow unstably and develop into high-intensity beam filaments within the laser medium, leading to bulk damage. This effect was thoroughly investigated in the 1970's during the development of very high power Nd:glass laser systems for internal confinement fusion at Lawrence Livermore National Laboratory, and is discussed in detail in the LLNL Laser

Project annual reports [7] as well as in Brown [5]. The total nonlinear phase delay experienced by a ray traversing an optical medium is given by the  $B$  integral,

$$B = \frac{2\pi\gamma}{\lambda} \int_0^\ell I(\ell) d\ell$$

where

$$\gamma = \frac{4\pi n_2}{c n} = 4.19 \times 10^{-3} \frac{n_2}{n} [\text{cm}^2/\text{W}]$$

$n$  = linear refractive index of medium

$n_2$  = nonlinear refractive index [esu]

$I(\ell)$  = beam intensity at position  $\ell$  in the optical medium [ $\text{W}/\text{cm}^2$ ]

$\lambda$  = lasing wavelength.

Note that the present usage of  $\gamma$  as a nonlinear coefficient differs from that given earlier as a bottlenecking parameter.

$B$  also governs the growth rate of ripple intensities, according to

$$I_{\text{ripple}} \approx I_{\text{initial ripple}} e^B;$$

because of this, the typical rule of thumb of laser workers is to keep  $B$  smaller than about 1 or 2. In very clean environments with very high quality optics, the low number of scatter sites may allow operation at somewhat higher values of  $B$ , but at substantial risk should any dust or contamination be introduced into the system. Our system is designed to run at a total  $B$ , summed through the system, of about 1.

In most calculations, we assume that the media are lossless, so for passive media,

$$B = I_0 \times \ell \times \frac{2\pi\gamma}{\lambda},$$

and for nonsaturated, high gain amplifiers

$$B = I_0 \times \ell_{e\text{-folding}} \times \frac{2\pi\gamma}{\lambda},$$

where  $\ell_{e\text{-folding}} = 1/\alpha$ . Clearly it is desirable to operate amplifiers at the highest possible gain to minimize the  $e$ -folding distance, and in general, to keep the laser intensity low by using as large a cross-sectional area as practical in all optics. Some optical materials are designed specifically to have the lowest possible values of  $n_2$  (e.g. fluorophosphate and fluoroberyllate laser glasses as well as certain terbium-doped Faraday rotator glasses).

## 2.2 Selection of laser materials

The Nd: family of laser materials was used in the present system for the following reasons: these materials have high energy storage capability, they are readily available, well characterized, and easily worked with, and their wavelength is suitable for our needs. In this section, characteristics of some Nd: materials are summarized and the reasons for our materials choices presented. Relevant numerical data for Nd: laser materials of interest are tabulated by Koechner [4] and Brown [5].

### Available Nd: laser materials

Laser glasses have lower gains by a factor of ten or more than their crystalline counterparts; this is due to the fact that the Nd: ions are not located in specific sites with respect to glass constituent atoms, so that they each see different electric fields and Stark shifts. This also accounts for their correspondingly broader linewidth, and for why the glasses can be more heavily (and more uniformly) doped without any strain developing. The upper limit on the doping comes from a decrease in fluorescent lifetime above about 5% doping.

Glasses have excellent optical properties, are isotropic, can be fabricated to virtually unlimited size, and can be polished easily to high optical quality.

Because of their low gain, glasses have very high energy storage capacity. Their thermal and physical properties, however, are generally inferior to those of crystals. For high energy, large aperture, low repetition rate pulsed amplifiers (and for very short pulse, bandwidth-limited lasers) Nd:glass is an appropriate material.

For low energy, high repetition rate applications such as oscillators, crystalline laser materials are desirable. They have high gain, high thermal conductivity and strength. However, they are expensive and difficult to fabricate with high optical quality, especially in larger sizes. Also, doping in crystals tends to be non-uniform.

## Materials selection

For our purposes, it is evident that crystalline laser materials alone are not sufficient to give the required output. Given the limitations on available sizes and on energy storage capability due to parasitic lasing (because of the high gain), crystalline lasers can store only up to  $\sim 1$  J at the most. Moreover, extracting 1 J in a 100 ps pulse would lead to a catastrophically high  $B$  integral because of the high intensity in the small available cross-sectional area of a crystalline rod.

It is therefore necessary to use a large glass amplifier for the final stage of the laser system. The lower gain and larger available size allow more energy to be stored, and the larger size also allows a large cross-sectional area and lower intensity to reduce the  $B$  integral. For the oscillator and as many amplification stages as possible, it is preferable to use crystalline laser materials with their higher gains and repetition rates. It is assumed that the desired output pulses will be no shorter than about 5 psec, because of the limited gain bandwidths of crystalline laser materials. A Nd-based laser generating pulse widths of a few



psec will need either to be all Nd:glass or else to use supplemental nonlinear bandwidth generation by an optical fiber or bulk medium.

Nd:YAG oscillators are frequently used with Nd:silicate glass amplifiers and Nd:YLF oscillators with Nd:phosphate glass. Phosphate glass has the advantages of higher gain and lower non-linear coefficient over silicate glass; for that reason, YLF/phosphate glass is the combination of choice in most current large, high power, high energy laser systems. Nd:YLF also has the advantage over Nd:YAG in that it has a higher saturation fluence and hence energy storage capability, so that it can be used further in the amplifier chain before being replaced by glass.

## 2.3 Laser architecture

Various options present themselves for the overall architecture of the laser system. To ensure a stable, reliable source of pulses, the “front end” should be a relatively low power TEM<sub>00</sub> modelocked oscillator generating pulses of durations adjustable from  $\sim 50$  to  $> 200$  psec. This could easily be done with a CW active-modelocked Nd:YLF oscillator, but such lasers, at  $\sim 5$  W and 8 nsec round trip time, generate only around 40 nJ per pulse. At a small incremental cost, it is possible to *Q*-switch/modelock a Nd:YLF oscillator to generate pulses of 50-100  $\mu$ J. Our system uses a commercial oscillator of this type (Lumonics AML series), which is described in more detail in Chapter 3.

For our amplifier system, a master-oscillator/power-amplifier (MOPA) configuration, consisting of a double-passed rod pre-amplifier (double pass gain of 1000) and an off-axis multipass large glass power amplifier (net gain of 100), was found to be appropriate. A summary of the considerations that entered this decision follows.

The amplifier system must then have a gain of about  $10^5$ . Three general ap-

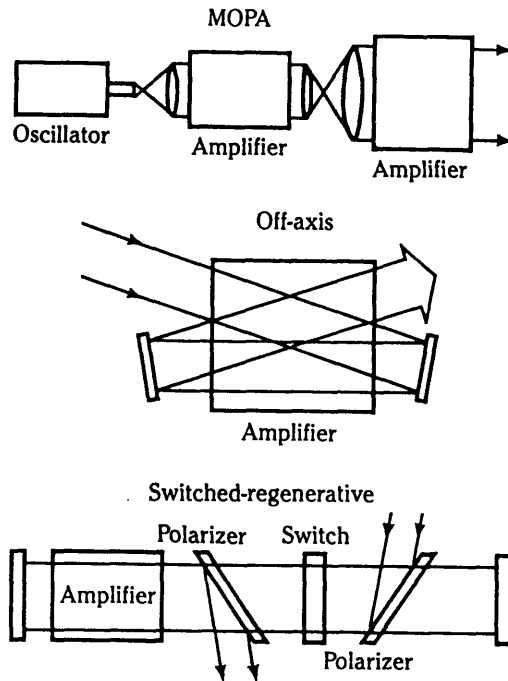


Figure 2.1: Amplifier configurations (from [7])

proaches to achieving this amplification are shown in Figure 2.1: a MOPA, an off-axis multipassing configuration, and a switched-regenerative configuration.

In the MOPA configuration, the beam passes linearly through a chain of amplifier stages with suitable optics for beam expansion, relay imaging, spatial filtering and isolation between stages. This approach requires a great deal of hardware: for our purposes, four rod amplifiers, or three rods and one disk, plus associated optics and electronics. It can be made more economical by doublepassing the amplifier heads using a polarizer with a polarization-rotating element (waveplate or Faraday rotator). Doublepassing a Faraday isolator is an attractive option because it provides doubled isolation against backward-propagating radiation in the amplifier chain.

Off-axis angular multipassing is an economical means to achieve several passes through a gain medium. Achieving two passes requires only a small

amount of extra clear aperture. Arranging three or more passes requires more optical complexity and clear aperture. A drawback to this technique is that the beam may need to propagate over longer distances than otherwise, in order to give spatial separation of the incoming and outgoing beams. If non-gaussian beams are used, there will be more ripple buildup due to diffraction. This problem can be alleviated by relay imaging optics.

The final approach to generating high amplification is by regenerative amplification [8] or its variants (e.g. injection seeding). In these techniques, only one amplifier head is used; it has an oscillator cavity around it, with a fast Pockels cell switch. The Pockels cell prevents self oscillation until the inversion in the amplifier is maximized; then a short pulse from the oscillator is injected and the Pockels cell is opened rapidly. The pulse overpowers the self-lasing of the cavity and circulates repeatedly through the amplifier until the desired amplification is reached or all the energy is extracted from the gain medium; then the Pockels cell is closed rapidly and the amplified pulse is switched out. This method is elegant, can have high net gain, and can extract almost all of the stored energy in the laser medium.

However, for the present purposes it has several shortcomings. First, the Pockels cell must have a large clear aperture and therefore a high capacitance, requiring the switching of kilovolts and kiloamps in nanoseconds. The driver electronics, as well as the Pockels cell itself, would be prohibitively expensive. Also, at 100 psec or less, if all the stored energy is extracted from a glass amplifier, typically the  $B$  integral limit will be far exceeded and optical damage will occur. The Pockels cell could be set to switch out the pulse before the limit is reached, but the system would then not be fail-safe. A final drawback is that the appropriate Pockels cell crystals (KD\*P) have high nonlinear coefficients, reducing the allowable output power for a given amplifier size.

## 2.4 Repetition rate considerations; use of slab amplifier

In order to achieve the desired shot rate of several shots per minute, a zig-zag slab power amplifier was used. The limiting element on the rate remains a conventional rod preamplifier stage, which is to be upgraded.

The most conventional implementation of our MOPA scheme would require a glass rod preamplifier of about 10 mm diameter and 200 mm length generating a single pass gain of  $\sim 35$ , and a large glass rod power amplifier of about 25 mm diameter and 200 mm length with a single pass gain of  $\sim 10$ . Both rods would be operating in double pass using a quarter-wave plate or Faraday rotator; this would, however, make the requirement for cooling time between shots very severe.

Thermal constraints on rod amplifiers arise from lensing and birefringence. Thermal lensing in phosphate glass can be alleviated by the use of athermal glass compositions (i.e. special glasses in which the temperature coefficient of optical pathlength is about zero). In crystals, no such option exists, but the thermal conductivities are much higher so the thermal gradients are less. Additionally, Nd:YLF has a particularly low optical pathlength temperature coefficient.

Thermal birefringence is not a concern in systems where the output polarization is unimportant, but for polarization-double-passed systems, it is critical for the rod to cool until the birefringence becomes small, otherwise the output will have a Maltese cross pattern and some radiation will be injected backward toward the oscillator. The thermal time constant of the rod is given by

$$\tau = \frac{r_0^2 c \rho}{K},$$

where  $r_0$  is the rod radius,  $c$  the specific heat,  $\rho$  the mass density, and  $K$  the

thermal conductivity. For the 10 mm preamp rod,  $\tau \sim 50$  sec; for the 25 mm power amp rod,  $\tau \sim 300$  sec. The latter is far too long for our needs; therefore the power amplifier stage uses a zig-zag slab.

The zig-zag slab amplifier geometry, discussed further in Chapter 4, cancels thermal lensing and reduces thermal birefringence at moderate repetition rates. Slabs of the size of interest to us can be run at 1 Hz or more. The geometry is also particularly amenable to multipassing and to generating rectangularly symmetric output beams for forming line foci. Because of the relatively low parasitic threshold of slabs, it is necessary to use three passes to achieve a gain of 100.

The present Lumonics laser includes a double-pass 9.5 mm  $\times$  200 mm athermal phosphate glass (LHG-8) rod preamplifier with a shot rate of twice per minute. As will be discussed in Chapter 3, an 8 mm  $\times$  75 mm *c*-axis Nd:YLF rod with which to replace this rod has been acquired and tested at repetition rates up to 0.3 Hz.



# Chapter 3

## Modelocked/ $Q$ -switched oscillator and preamplifier

### 3.1 Oscillator

This chapter discusses the low-power laser system used to generate short pulses for amplification in the zig-zag slab. Although this system was a commercial unit, it required substantial modification in order to perform to specification. A complete set of design calculations was done for the modelocked/ $Q$ -switched oscillator and the unit modified accordingly. Also, the preamplifier was upgraded to run with a high-repetition-rate Nd:YLF rod. The optical system was also rebuilt; the improved design is discussed in Chapter 5.

As mentioned in the preceding chapter, it was decided to use a simultaneously modelocked and  $Q$ -switched oscillator. In this type of system the modelocking can provide pulses of durations ranging from several picoseconds to around a nanosecond, depending on the choice of gain medium, the type of modelocking (passive or active), the strength with which it is applied, and the presence of intracavity etalons. The  $Q$ -switching allows the trans-

fer of most of the stored energy in the laser rod into an envelope containing 10-100 modelocked pulses, depending upon the ratio of gain to loss; in this way it can generate individual pulses with energies approaching millijoules. CW-modelocked lasers, by comparison, generate individual pulses with nanojoule energies and therefore need another stage of regenerative amplification. Essentially, modelocked/ $Q$ -switched lasers combine the modelocking and the regenerative amplification into one stage.

Simultaneously modelocked and  $Q$ -switched oscillators were investigated in the 1970's for use as the front end for large fusion-class lasers at the Lawrence Livermore National Laboratory [9]. In the first efforts, using CW pumping of Nd:YLF and active modelocking and  $Q$ -switching, it was discovered that the  $Q$ -switch build-up time (a few microseconds) is too short for the modelocking to go to completion (typically hundreds of microseconds to milliseconds). To remedy this, in subsequent investigations the  $Q$ -switch loss was reduced during the "off" portion of the cycle to allow the oscillator to lase CW at a low level for several milliseconds and allow a transform-limited pulse to develop. It was found that using such a prelased, active modelocked system generated pulses that were very stable from shot to shot, with pulse energy fluctuations less than 5% and consistently transform-limited pulse forms without substructure.

Passive modelocking (and hybrid passive-active) has also been investigated for use in  $Q$ -switched systems. It has the advantage of being simple and inexpensive. For our purposes, it has two shortcomings compared with active modelocking: less reliable modelocking (80%-90% of shots typically produce good, clean pulse trains) and shorter pulse durations than required for our purposes. The pulses can be stretched using an intracavity etalon, but it has been found that such pulses still often exhibit short time-scale substructure limited only by the gain bandwidth, so that the pulses are not transform



limited. Since our amplifier chain is susceptible to damage by small-scale self-focusing, which is proportional to the intensity, it is vital that pulses of a given maximum energy neither be too short nor have short time-scale substructure with high peak intensities.

In recent years it has become popular for workers in laser-plasma physics to use very stable CW-modelocked lasers with regenerative amplifiers. These systems are mainly useful for chirped-pulse amplification (CPA) systems; the signal is accessible while at the nanojoule level for pulse stretching in a single-mode fiber, whereas the output of a modelocked,  $Q$ -switched laser is expected to be above the danger limit of a fiber. A signal can be stretched to around half a nanosecond, amplified to the intensity limit of the amplifier chain, then recompressed (with some loss) to any pulse length down to the bandwidth limit, typically a picosecond or less. For pulses of  $\sim 60$  psec duration, the potential benefit of CPA is probably only a factor of 3-5 increase in output energy. A modelocked,  $Q$ -switched oscillator is probably the most economical and practical choice for our present system. CPA can still be implemented using other means for bandwidth generation and pulse stretching, as is currently planned for a modification to generate 10-15 psec pulses.

Usually the crystalline media Nd:YAG or Nd:YLF are used in active modelocked,  $Q$ -switched systems because of their high gain and low lasing threshold. Nd:glass can be used to give a shorter pulse duration due to its greater bandwidth. However, it needs to be pumped much harder than YAG or YLF and also suffers much more from thermal effects which in turn make it modelock less reliably.

An active modelocked,  $Q$ -switched Nd:YLF oscillator was procured from Lumonics, Inc.; it did not, however, initially perform to specifications. Therefore the system was analyzed according to the work of Kuizenga [9] and stan-

dard  $Q$ -switching theory [10], and using the Lumonics components with correctly adjusted parameters, the oscillator was made to run according to its specifications.

The main problem with the system initially was that although it was *designed* to prelase it did not in fact do so. Prelasing serves three purposes: it allows a stable, transform-limited pulse to develop, reliably and repeatedly. It also clamps the oscillator gain at a level corresponding to the  $Q$ -switched loss when off, so that when the  $Q$ -switch is opened there is a precisely set amount of stored energy available, and the  $Q$ -switched pulse energies and build-up times are very consistent. In non-prelased  $Q$ -switched systems, flashlamp fluctuations can cause a varying level of stored energy and initial gain, so that the build-up time and pulse energy tend to vary over  $\sim 10\%$ . Finally, the prelase serves as a valuable diagnostic of the modelocking. When a laser goes above threshold, relaxation oscillations occur on a 10- $\mu$ sec time scale between the laser field and the storage medium. In a non-modelocked, multimode laser, oscillations occur in each axial mode independently and the result is a very noisy, irregular laser output; this can be seen in our prelase if the modelocker is turned off. In a single-axial-mode laser, the oscillations are of relatively constant frequency and are smoothly exponentially damped. In a well mode-locked laser, the modes are tightly coupled so that they go through their relaxation oscillations together, and the output (prelase output in our case) resembles the smooth decay of the single-mode laser. If the cavity length is slightly detuned from the modelocker RF frequency, then driven relaxation oscillations occur throughout the prelase. By observing the prelase waveform on a slow oscilloscope, one can diagnose and optimize the modelocking behavior of the oscillator. Unfortunately the prelase is very sensitive to slight disturbances. Very high frequency electrical noise from the amplifier flashlamp

triggers, for example, was coupled in to the oscillator through the  $Q$ -switch voltage and caused spontaneous relaxation oscillation outbursts. This could only be alleviated by slowing down the  $Q$ -switch with a parallel capacitor.

## 3.2 Active modelocking theory

The modelocking behavior of the laser is determined almost entirely by the prelude. The  $Q$ -switched portion of the pulse is short relative to timescales for alteration of the modelocking behavior, and the  $Q$ -switching dynamics are independent of the nature of the short pulses being  $Q$ -switched, so the modelocking and  $Q$ -switching processes are decoupled and may each be considered independently. The modelocking during the prelude can be predicted using the general theory of active modelocking [9], where the central limit theorem causes a Gaussian pulse shape to develop with a steady-state pulsewidth

$$\tau_p = \frac{(2 \ln 2)^{1/2}}{\pi} \frac{1}{\theta_m^{1/2}} \frac{1}{f_m^{1/2}} \left( \frac{g}{\Delta f^2} + \frac{1}{\Delta f_e^2} \right)^{1/4}$$

where

$g$  = roundtrip saturated amplitude gain

$f_m$  = modulation frequency = 133 MHz for our system

$\Delta f$  = effective linewidth = 376 GHz for YLF

$\Delta f_e$  = intracavity etalon bandwidth =  $\frac{2c}{\pi n} \frac{1}{n^2 - 1}$  for an uncoated substrate  
 = 87 GHz for a 2 mm SiO<sub>2</sub> etalon

$\theta_m$  = modulation depth, for modulator transmission  $T(t) = \cos(\theta_m \sin \omega_m t)$   
 = 1.16 rad measured for our system at maximum RF power

The amplitude gain  $g$  is found from setting

$$GL = e^{2g} L \equiv 1$$

Mode	Current
CW	53 A
ML CW	58 A
ML QS	66 A

Table 3.1: Oscillator thresholds

so

$$g = -(1/2) \ln L,$$

where  $L$  is the cavity loss.

The pulsewidth is not very dependent on  $g$  for the non-etalon case, and almost completely independent of it with an etalon inserted, so a rough estimate for  $g$  suffices. The cavity losses come from the following: the output coupler ( $R = 60\%$ ), the modelocker, the  $Q$ -switch (blocking), and the various other optical surfaces in the cavity (there are 48 other AR-coated surfaces per round trip, so at  $R \sim 0.3\%$  each, we estimate a transmission of 85%).

The modelocker and  $Q$ -switch losses are estimated by considering the impact upon the lasing threshold when these items are turned on. The oscillator lamp current dial setting is proportional to the current, and the lamp power is proportional to  $i^{3/2}$ , according to the current-voltage relation for flashlamps,  $v \sim i^{1/2}$  [11]. The rod gain coefficient at threshold is roughly proportional to the lamp power, since the lamp pulse is long compared to the fluorescent lifetime and the pumping is essentially CW. Typical thresholds are given in Table 3.1.

The modelocker transmission can be found to be 88.3%, and that of the  $Q$ -switch to be 83.2%. For the  $Q$ -switch, this value can be compared with that predicted by considering the  $Q$ -switch voltage, set at 950 V: for the material KD\*P, this voltage corresponds to a retardation of  $\lambda/12$ , which in double pass gives a predicted transmission of 75%. The observed transmission is higher

because there are Brewster angle surfaces which partly repolarize the radiation between passes through the  $Q$ -switch (in the case of complete repolarization the predicted transmission is 87%).

Now the gain is given by

$$g = -(1/2) \ln(.6 \times .85 \times .883 \times .832) = .491$$

The expected pulsewidths are

$$\tau_p = \begin{cases} 41 \text{ psec with no etalon} \\ 103 \text{ psec with 2 mm etalon} \end{cases}$$

The required buildup time to reach steady state can also be estimated from Kuizenga [9]: for the case of no etalon, the time for the pulse duration to come within 5% of its steady state value is given by

$$t_{\text{buildup}} = \frac{.38}{\theta_m f_m} \frac{\Delta f}{\sqrt{g}} \times T = 1320 \times 7.5 \text{ nsec} = 10 \mu\text{sec},$$

where  $T$  is the cavity round-trip time.

This is much larger than the duration of a  $Q$ -switched pulse and demonstrates that prelasng is necessary to allow the modelocking to go to completion. Note that the actual prelasng duration is several milliseconds, which is much more than necessary to complete the modelocking; the reason for such a long prelasng is to allow relaxation oscillations to damp out. The pulse bandwidth has a similar buildup time to go from broadband noise to a transform limited width corresponding to the gaussian of duration  $\tau_p$ . If the pulse is extracted before the modelocking has gone to completion it will be both longer in duration (typically) and wider in bandwidth than the steady state; it will have noisy substructure with the potential for intensity spikes which are dangerous for optical components.

The buildup time with the etalon is much quicker. It is given by

$$t_{\text{buildup}} = \frac{.38}{\theta_m f_m} \times \Delta f_e \times T = 1.6 \mu\text{sec}.$$

Therefore we expect the pulsewidth with the etalon installed to be more robust and stable against perturbations to the system, as it can recover faster. Indeed it is observed that the prelude is far less sensitive to cavity length changes and electrical noise in this case.

Note that the longer pulses could also be generated simply by lowering the RF power (i.e.  $\theta_m$ ) rather than by installing the etalon. However this will make the buildup much longer rather than shorter, and the modelocking less robust. In general, it is preferable to modulate as hard as possible and to control the pulselength by adding bandwidth limiters (etalons or waveplates).

### 3.3 $Q$ -switch dynamics

The  $Q$ -switched behavior can be analyzed using the formulation of Siegman [10]. Basically, for our precluded oscillator, the  $Q$ -switch loss during the prelude will determine the gain and hence the inversion in the YLF rod. Having a high  $Q$ -switch loss will result in a high inversion and thus a fast build-up and short, high energy output pulse envelope. Originally the  $Q$ -switch was set at 1.4 kV, which would have generated a pulse train of energy greater than 10 mJ, far above the damage limit of the cavity optical components had the system been driven all the way into the precluded regime. To correct this problem, the voltage was reduced to 950 V by lowering the supply voltage and removing two avalanche transistors from the string of five.

The  $Q$ -switching dynamics are governed by the initial inversion ratio  $r$ , the fractional loss per round trip  $\delta_c$ , and the cavity round trip time  $T$ . The inversion ratio is given by

$$r = \frac{N}{N_{th}} = \frac{\ln G}{\ln G_{th}} = \frac{g}{g_{th}}.$$

The threshold gain  $g_{th}$  is that required to offset all losses in the cavity, with the

$Q$ -switch transmitting; the actual initial gain  $g$  is that found in the previous section, with the  $Q$ -switch blocking:

$$r = \frac{\ln(.6 \times .85 \times .883 \times .832)}{\ln(.6 \times .85 \times .883)} = 1.23$$

The fractional loss is  $\delta_c = \ln(1/L) = .80$ , and the cold cavity decay time is  $\tau_c = T/\delta_c = 7.5/.8 \text{ nsec} = 9.4 \text{ nsec}$ . Now the pulse intensity  $e$ -folding time is given by

$$\tau_{e\text{-folding}} = \frac{9.4 \text{ ns}}{r - 1} = 4.08 \text{ nsec}$$

Typically the prelude is run at a level of about 1/1500 that of the peak of the output, so that about 8  $e$ -foldings, or 320 nsec, are expected from the time the  $Q$ -switch is opened to the pulse peak.

The extraction efficiency for  $r = 1.23$  is  $\eta = 34\%$ , from a plot given by Siegman [10]. Calculating the stored energy in the rod contained within the gaussian beam radius  $w_0/\sqrt{2}$  gives a value of 27 mJ, so that 9 mJ should be extracted. Of this, about 5.4 mJ should be in the beam coupled out by the output coupler.

The pulse envelope width can also be estimated. We have

$$\tau_{\text{pulse envelope}} = \frac{r \eta(r)}{r - 1 - \ln r} \tau_c = 171 \text{ nsec}$$

These quantities were each measured on the laser with the new  $Q$ -switch settings, and the experiments agreed with the predicted values within  $\sim 10\%$  when the laser was run at an output energy of 5 mJ.

Both the laser manual and our experience with damaged oscillator rods, however, recommend against operating the laser regularly at total pulse energies above about 3 mJ. The cause has not been pinpointed, but over time a damage site consistently begins to develop in the middle of one of the AR coatings of the oscillator rod. The laser threshold rises concurrently, and eventually the oscillator lases multi-transverse-mode. The total fluence through the rod

is calculated to be  $0.3 \text{ J/cm}^2$ , which is comfortably below the damage limit. We have handled the problem by acquiring a second rod and always keeping one rod repolished and recoated, ready to substitute for the other when it damages. Typical lifetimes seem to be several months of heavy use. Unfortunately, a complete system realignment is needed upon replacement of the rod.

To prolong the rod lifetime, therefore, the oscillator is being operated at  $3 \text{ mJ/pulse}$ . Since it was impractical to lower the  $Q$ -switch voltage any further, the  $Q$ -switch crystal was instead misaligned slightly; a misalignment of a few degrees reduces the pre-lase loss enough that the output energy drops to  $3 \text{ mJ}$ . The buildup time and pulse envelope duration are lengthened correspondingly. The energy contained in a single mode-locked pulse is about  $50 \mu\text{J}$  under these conditions.

### 3.4 Observed oscillator performance

Following the correction of the oscillator, the pulsewidth was measured by J. Goodberlet using both second-harmonic generation (SHG) and interferometric autocorrelation techniques. For the case with no etalon, the pulsewidth was found to be  $61 \text{ psec}$ , whereas with a  $2 \text{ mm}$  etalon it was found to be  $120 \text{ psec}$ . An SHG autocorrelation measurement with no etalon is shown in Figure 3.1.

The pulsewidths were very consistent from shot to shot, and the interferometric measurement demonstrated that the pulses were not chirped. The pulses were probably longer than predicted either because of etalon effects off the many surfaces in the cavity, or because the diffraction efficiency of the acousto-optic modulator could have been lower than we originally measured, depending upon the laser alignment.

The  $Q$ -switched envelope was also observed, using a slow photodiode and



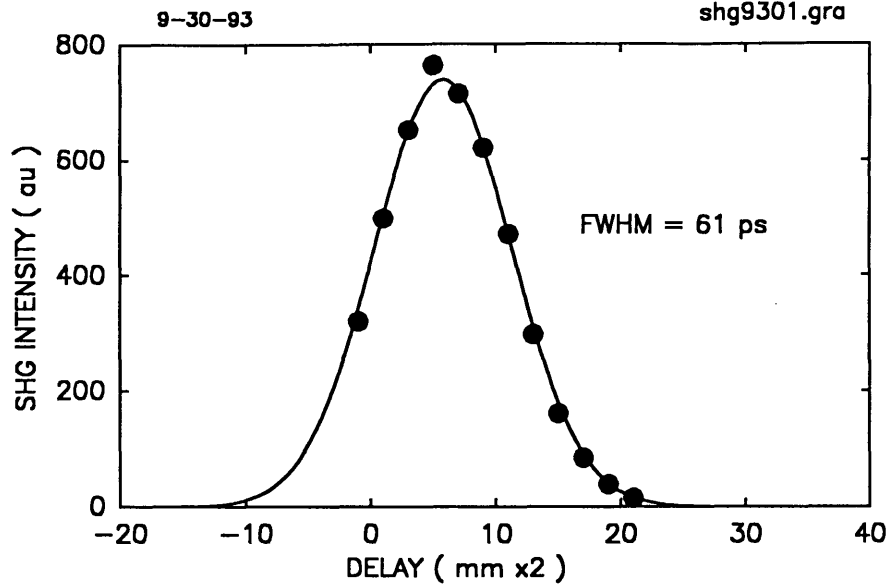


Figure 3.1: Autocorrelation measurement of modelocked pulse width

oscilloscope; it is shown in Figure 3.2. The width is measured to be 200 nsec at an integrated pulse energy of 3.2 mJ.

### 3.5 Preamplifier

The preamplifier head contains a 9.5 mm  $\times$  200 mm LHG-8 Nd:glass rod pumped by four xenon flashlamps at up to 2000 J (2.0 kV). The double-pass gain of this head was measured by the author and M. Bierbaum; the results are shown in Figure 3.3.

Since this glass rod limits the system repetition rate to one shot per 30 seconds, it was decided to replace it with a Nd:YLF rod with a repetition rate near 1 Hz. Nd:YLF is uniaxial and is normally grown in an  $a$ -axis orientation, so that the two polarizations in the rod offer gain at 1053 nm ( $E \parallel a$ ) and 1047 nm ( $E \parallel c$ ). An advantage of this orientation is that the natural birefringence between the  $a$  and  $c$  axes overwhelms any thermally induced birefringence. Unfortunately, the 1047 nm line has the higher gain by 50%, so

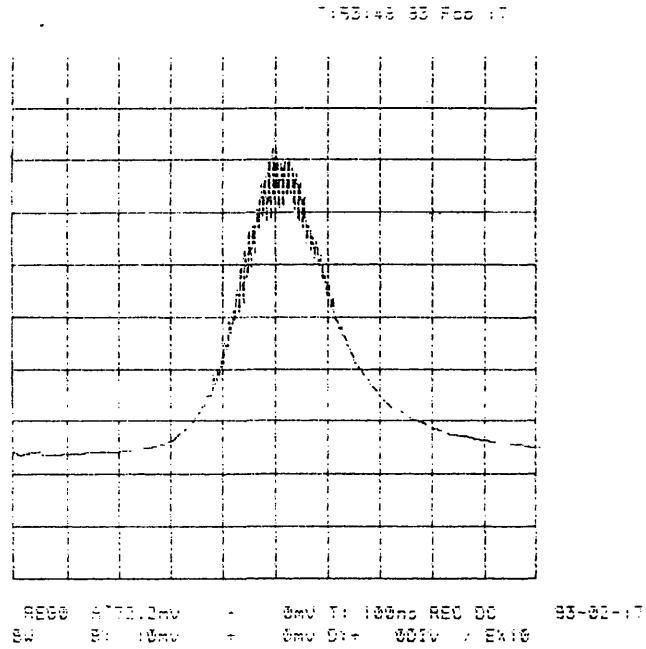


Figure 3.2:  $Q$ -switched pulse envelope. The  $Q$ -switch is activated at the left edge of the trace.

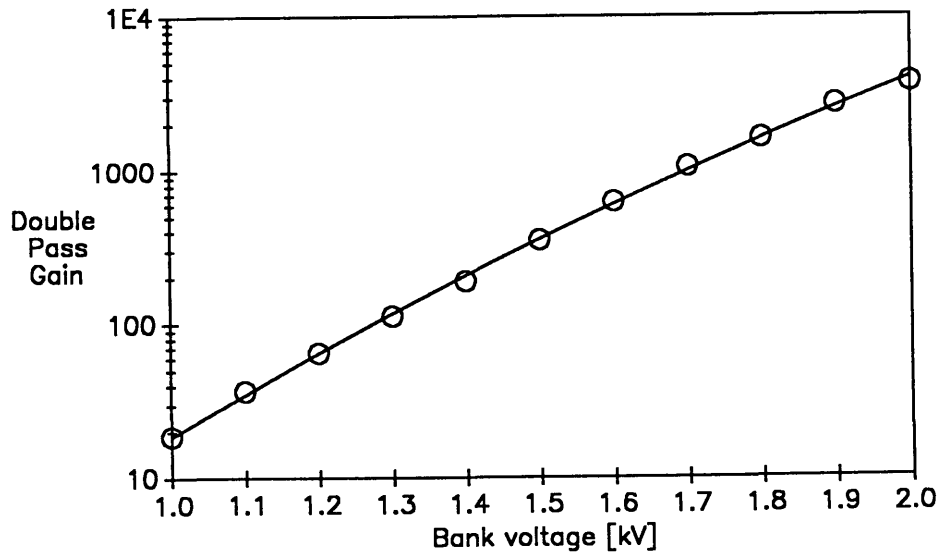


Figure 3.3: Double-pass gains of Nd:glass preamplifier

that the parasitic limit for both lines is determined by the gain at 1047 nm. Since this gain is likely to clamp at about 100 in single pass, the maximum possible gain at 1053 nm will be around  $100^{2/3} \sim 20$ .

Since a gain of 20 is too low for our purposes, a *c*-axis rod was used; in this orientation, the 1047 nm gain direction lies transverse to the rod, and the parasitic limit is determined by the 1053 nm gain. Moreover, both rod polarizations are now oriented for gain at 1053 nm, which simplifies double-passing (it can be done with a quarter-wave plate rather than necessarily with a Faraday rotator). The rod was specially fabricated by Litton Airtron; at 8 mm × 76 mm, it represents the current state of the art in YLF crystal size. It was mounted installed in the preamplifier head using stainless steel adapter tubes mimicking the Nd:glass rod size, and a single-pass gain of 75 was measured at a lamp energy of 1280 J (1.6 kV). No thermal distortion was seen at repetition rates of 0.3 Hz. This first rod was subsequently found to have high internal scatter, however, and was replaced with a second rod that appears to be of higher optical quality.

The Nd:YLF rod can in theory be used at energies over 100 mJ for 60 psec pulses, because its gain is high and its nonlinear index low. The rod will be in saturation at these energies; if a train of pulses is being amplified, the amplification will decrease during the train. This effect can be lessened, in a double-pass system, by passing the entire train through one pass before making the second pass. It can be completely eliminated by reducing the input energy of the earlier pulses in a prescribed manner. For a two-pulse train, as is needed by our collisionally-pumped x-ray laser scheme, the input energy of the first pulse can be decreased by slowing the transition speed of the pulse-selecting Pockels cell with a parallel capacitor and adjusting the timing of the cell. In this way, the first-pulse input can be optimized to give any desired relative

values of the two output pulse energies.

# Chapter 4

## Zig-zag slab amplifier

### 4.1 Introduction

This chapter summarizes the design and performance of the Nd:glass zig-zag slab amplifier head. Several aspects of this unit are novel: it gives our system a higher repetition rate than comparable systems currently in use for high-intensity laser-plasma studies; it is the first large glass laser to be cooled by a forced-gas flow; and, to our knowledge, it has demonstrated the highest single-pass gain of any slab amplifier. A further benefit of the slab architecture, for x-ray laser applications, is that the rectangular symmetry of the beam profile and the uniformity of the gain across the beam simplify the generation of a uniform line focus.

Since suitable systems were not available commercially, the amplifier head, flashlamp electrical system, and cooling system needed to be designed and built. Much of this work was done during a yearlong visit with the Laser Program of the Lawrence Livermore National Laboratory.

A history of zig-zag slab development appears in Koechner [4]. Briefly, the zig-zag concept was patented by Martin and Chernoch [12] at General Electric

in 1972; subsequently, slab laser development efforts began in 1979 in R. Byer's group at Stanford [13], and in 1985 in the High Average Power laser group at LLNL [14]. Various other groups have also reported slab laser development; our design, however, was influenced most strongly by the LLNL and Stanford efforts.

To date, most slab lasers have been developed for long-pulse operation in welding, materials processing, and other high-average-power applications. Some of the LLNL and Stanford efforts were also directed toward producing laser-plasma x-ray sources for x-ray lithography; these used pulse durations down to about 1 nsec but were, in general, still not limited by intensity damage but rather by thermal effects.

Operation in the 60 psec regime at high intensity causes  $B$  integral and beam propagation issues to become important. Techniques from the fusion laser field must be applied: the slab is designed to be proportionately wider and shorter, and to operate at the highest gain; the optical system is designed to create a clean, flat-top beam and preserve it by spatial filtering and relay imaging.

Other slab lasers run at 10-100 Hz and are therefore water-cooled, raising issues of degradation of the large optical surfaces by coolant exposure and sealing of the edges of the optical surfaces. Since for x-ray lasers and similar plasma experiments, the target must be replaced and realigned on each shot, repetition rates under 1 Hz are adequate. The reduced repetition rate requirement allows forced-air cooling, which avoids the problems associated with water cooling.

In Table 4.1, the observed slab amplifier performance is summarized along with the original goals. It can be seen that most of the original goals were exceeded.

	Goal	Achieved
Peak power	10 GW	33 GW
Energy per pulse	1 J (100 psec)	2 J (60 psec)
Maximum 1-pass gain	4	7.5
Storage efficiency	3%	4%
Beam quality ( $\times$ diff lim)	$\sim 2\times$	$\sim 1.5\times$
Repetition rate	0.3 Hz	0.3 Hz

Table 4.1: Slab amplifier goals and achieved performance

## 4.2 Overall layout

A schematic of the slab amplifier head is shown in Figure 4.1. The slab is mounted vertically and pumped from both sides by pairs of flashlamps in reflective pump cavities. A rectangular beam propagates down the length of the slab. Antireflection-coated glass blast shields protect the slab in the event of a flashlamp explosion and also serve as ducts for the cooling air flow.

## 4.3 Slab geometry

A schematic of the beam propagation through the slab is shown in Figure 4.2. The beam enters the slab nearly straight-on and is refracted by the wedged ends so that it zig-zags down the length of the slab by total internal reflection from the large faces. The beam is directed by external optics to pass through the slab three times to give the required gain.

The wedge angles and beam axis angles are determined by the requirements of Brewster-angle entry and unit slab fill. The requisite wedge angle is found to be  $(\tan^{-1} n)/2 = 28.4^\circ$  for Nd:phosphate glass, and the external angle of approach of the beam is  $4.9^\circ$  from the slab axis. Fourteen bounces occur per pass; the pumped region covers a length of 12 bounces.

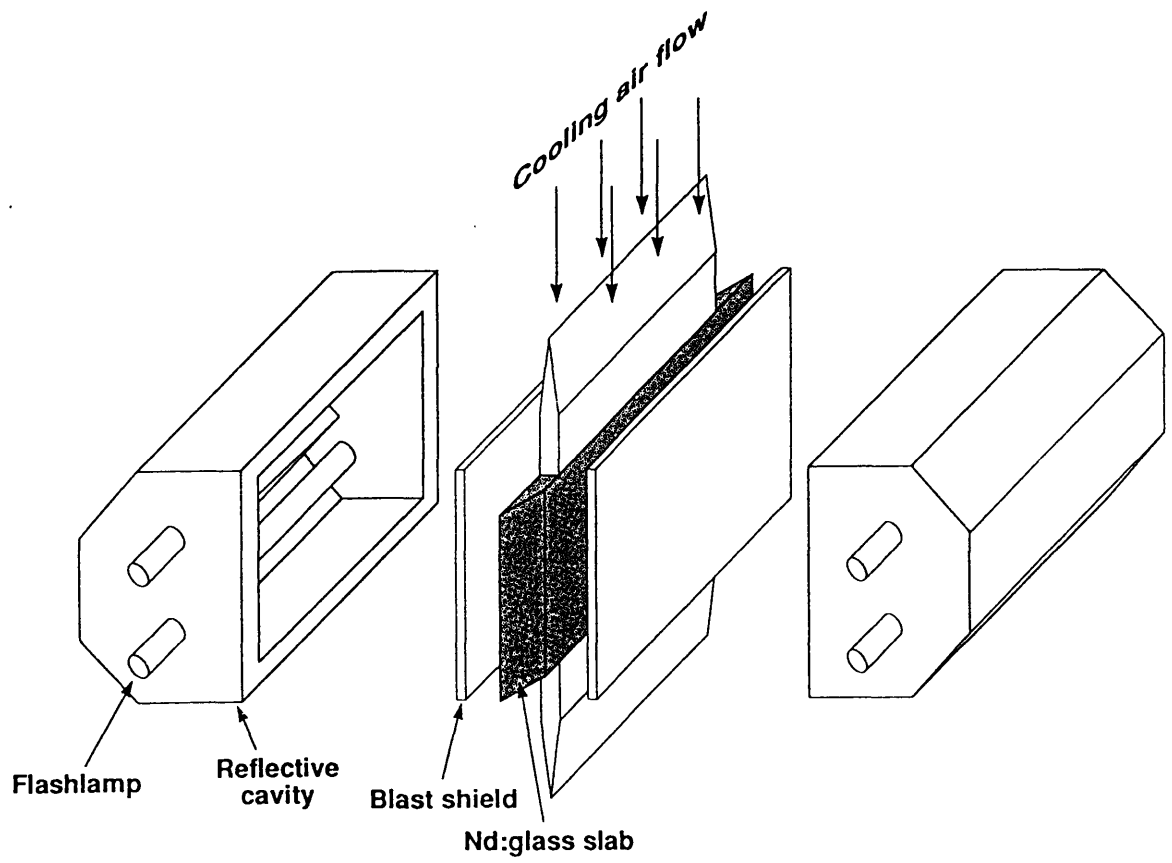


Figure 4.1: Slab amplifier head layout

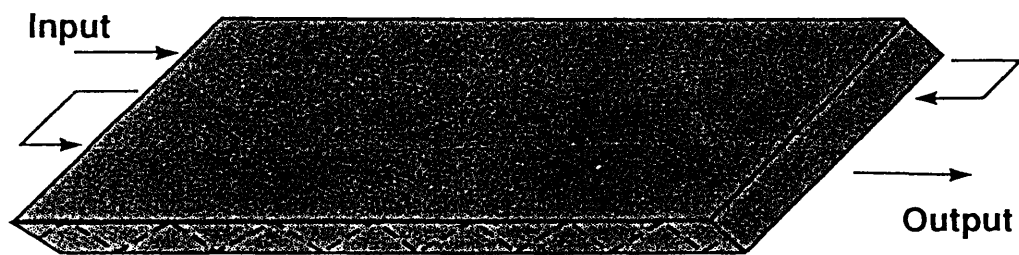


Figure 4.2: Beam propagation through zig-zag slab



The slab dimensions were chosen as follows: the length, to give the required net gain; the width, to give the required cross section; and the thickness, to give acceptable thermal behavior. In view of the success of this slab in thermal performance, future slabs could be designed to be considerably thicker and to operate at correspondingly higher peak powers.

## 4.4 Slab fabrication

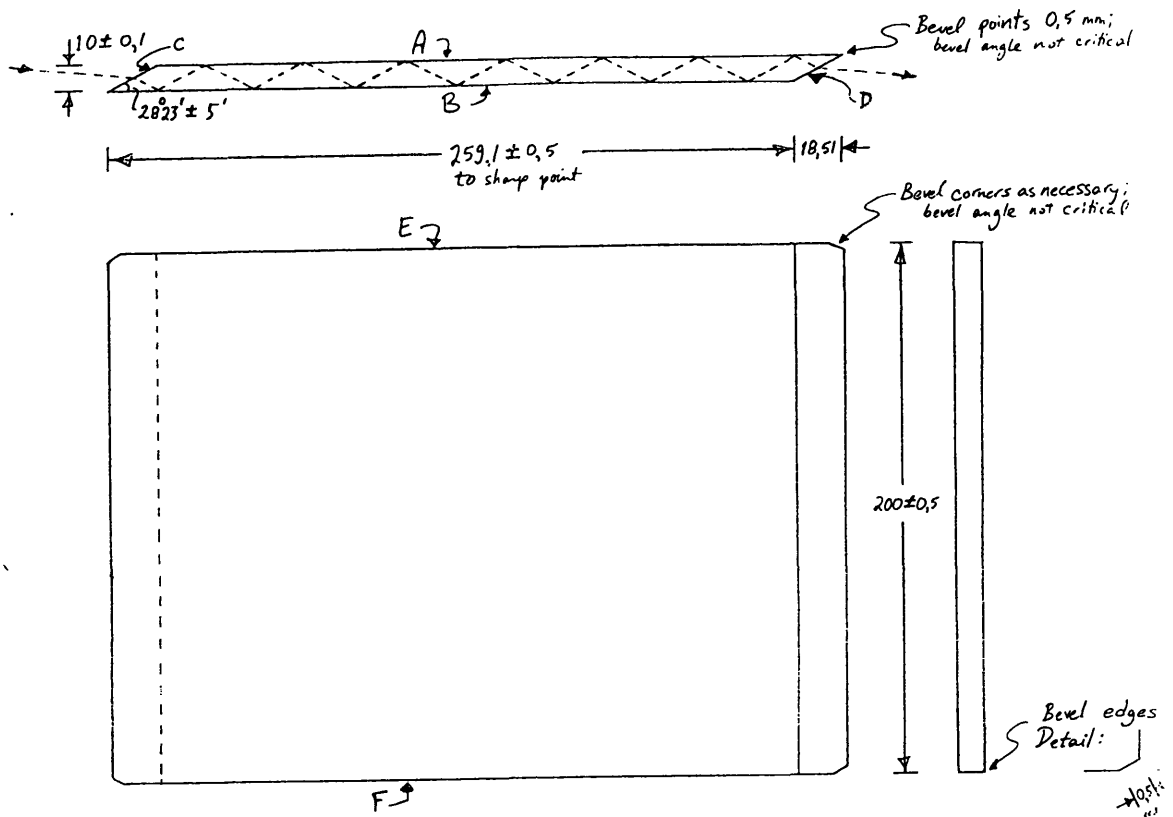
Schott APG-1 phosphate glass was used for the current slabs: this is a specialized glass with high thermal conductivity, high fracture strength, and low solubility, which was developed for the LLNL slab laser program. Our present experience suggests that standard glass probably would be satisfactory for future slabs (Schott LG-760, for example, has poorer thermal characteristics but 20% higher gain and a lower nonlinear coefficient than APG-1).

Because of the zig-zag beam path, both the ends and the faces must be highly flat and parallel; fabrication of large slabs is consequently a specialized and costly operation. Two slabs were fabricated to the specifications given in Figure 4.3 by Wild Leitz AG, Switzerland.

A Michelson interferometer was set up and the slabs tested upon receipt; a double-pass transmission interferogram at 633 nm is reproduced in Figure 4.4. The slab shows several fringes of sphericity but is probably close to specification; in practice, no significant degradation of the beam quality by the slab has been observed.

## 4.5 Parasitics

As was mentioned in Chapter 2, parasitic oscillations ultimately set the maximum gain that can be achieved in a laser amplifier. The zig-zag slab is



Material: Schott APG-1 Phosphate Glass, 3% & 5% Nd Surfaces: "A", "B", "C", "D" Laser Polish  
 "E", "F" Felt Polish  
 "MIL 30 Scratch/10 Pol"  
 Angle Tolerance: "A" to "B" parallel  $\leq 1'$   
 "C" to "D" parallel  $\leq 1'$   
 "E" to "F" parallel  $\leq 10'$   
 Flatness, "A", "B", "C", "D":  
 (2/10) / 5 cm each direction  
 2/4 total  
 $\lambda = 1054 \mu\text{m}$   
 Fabricate slabs from blanks 281 x 201 x 11 mm<sup>3</sup>  
 No coatings

M.H. Muendel, Mass. Inst. of Tech.		
Nd: Glass Laser Slab, Version I		
Scale 1:2	Dimensions mm	21 June 89

Figure 4.3: Slab fabrication drawing

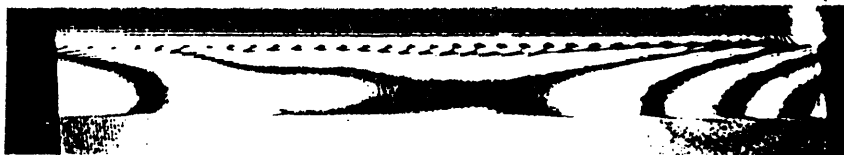


Figure 4.4: Slab transmission interferogram

Zig-zag slab ray threshold gains - John Trenholme - 05-29-1989 03:28  
 Wedge angle 28.4 Slab index 1.526 Angle count 360  
 Center L / T 25.9 Face index 1 Pass count 2

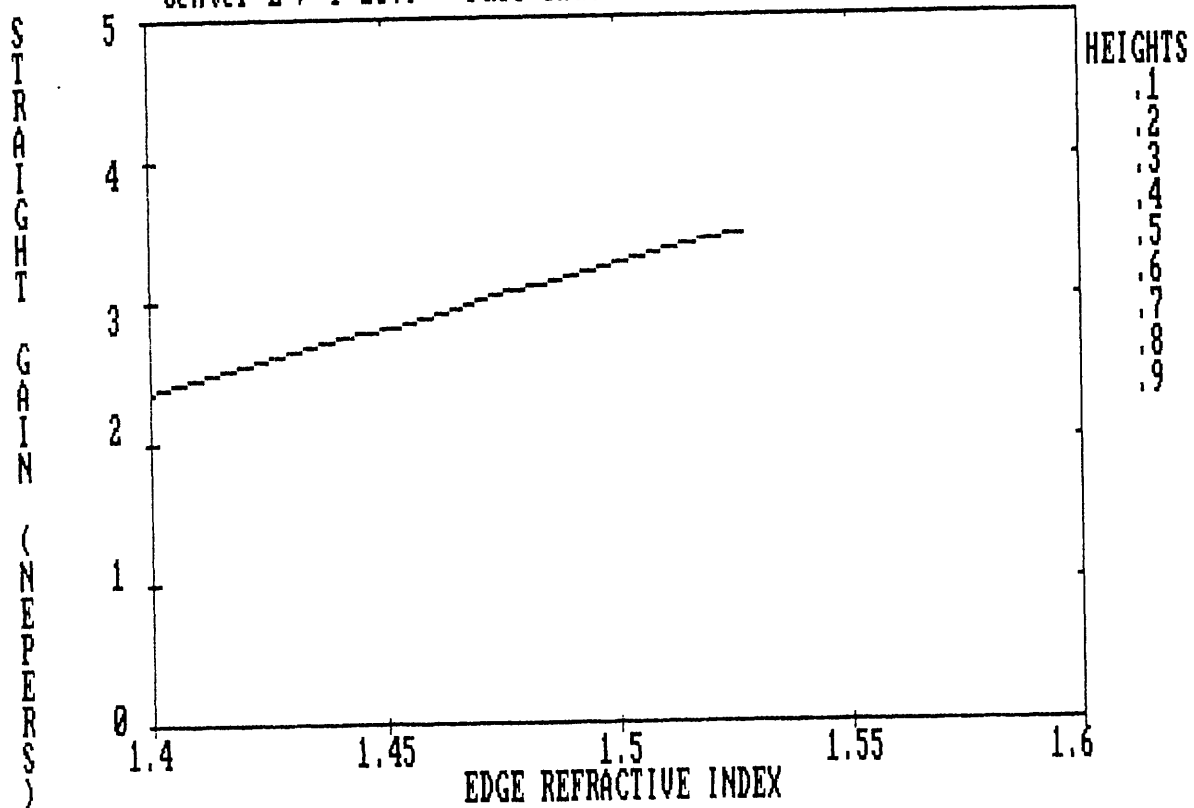


Figure 4.5: Parasitic thresholds versus edge cladding index

particularly susceptible to parasitics because the large faces are flat, parallel, and polished. The presence of an air boundary rather than water worsens this problem.

The upper and lower edges of the slab are accessible to be used for parasitic control; IR-absorbing edge-cladding glass was glued on them. A ray-trace code of J. Trenholme at LLNL was used to estimate the parasitic threshold as a function of the edge-cladding material refractive index. The results are shown in Figure 4.5. The estimated thresholds were near enough to the desired gain to cause concern; it was clear that exact index matching of the edge cladding

was very important.

To match the laser glass ( $n = 1.526$ ), the Schott filter glass KG-3 ( $n = 1.52$ ) was chosen and acquired in 1.5 mm thick strips which were then cut to fit the slab edges. This glass is highly absorbing at 1053 nm and transmissive in the visible. In order to prevent the escape of visible pump radiation through the slab edges and the cladding glass, the rear surface of the cladding was silvered; a pump-cavity simulation (described below) estimated a 9% improvement in efficiency as a result of this innovation.

The edge cladding was glued onto the laser glass using the UV-curable optical cement Norland NOA-65 ( $n = 1.52$ ). This cement was chosen because of the ideal index match and because it is relatively flexible and therefore forgiving of thermal coefficient mismatch between the two glasses. A sample of the cement was exposed to approximately 1000 high energy flashlamp pulses to verify that the cement is not degraded by the high intensities or the UV component in the lamp spectrum; no degradation was seen.

## 4.6 Flashlamps and electrical system

The slab is pumped by four EG&G FX-47C water-cooled flashlamps with 13 mm bore diameter, 200 mm arc length, 22 mm water jacket, and 450 torr xenon fill pressure. Ce-doped quartz lamp envelopes are used to reduce UV emission and prevent solarization of the slab. The lamp electrodes are processed for full simmered operation.

The lamp discharge parameters were optimized using a flashlamp simulation code of K. Jancaitis at LLNL. For the lamp pulse duration, a tradeoff exists between increased efficiency with shorter pulses (because of the 350  $\mu$ sec stored energy lifetime), and decreased permissible pulse energy (due to lamp lifetime considerations). The optimal pulse duration was found to lie near

500  $\mu\text{sec}$ ; a total pulse energy of 6800 J then corresponds to 25% of the lamp explosion energy, which gives an expected lifetime of  $10^4$ - $10^5$  shots [Koechner]. In practice, the energy is kept below a 20% explosion fraction.

Two single-mesh pulse forming networks (PFNs) were constructed to provide the required pulses to the lamps, which are wired in series pairs. The parameters for critical damping at 25% explosion and 500  $\mu\text{sec}$  pulse duration are  $C = 350 \mu\text{F}$ ,  $L = 120 \mu\text{H}$ , and  $V = 5000 \text{ V}$ . At lower energies, the pulse becomes slightly underdamped. A 1500 J/sec capacitor charging supply from a.l.e. systems is used, which operates at 0.3 Hz for typical pulse energies.

The capacitance is provided by fourteen 50  $\mu\text{F}$  5000 V capacitors. The lamp discharge is initiated by series injection triggering. Transformers with 80  $\mu\text{H}$  saturated secondary inductance were wound using 10-gauge 30-kV Teflon-insulated wire on Hypersil tape-wound cut cores, and air-core inductors provide the remaining 40  $\mu\text{H}$ . Because the magnetization curve is not well known in the regime of kiloamp currents, the transformer inductance was optimized experimentally. The turns ratio is 120:3; trigger pulses of 25 kV and 2  $\mu\text{sec}$  are generated using 2  $\mu\text{F}$  capacitors charged to 600 V and discharged through the transformer primaries by SCRs.

The electrical system was configured to allow simmered and prepulsed operation modes in addition to the standard single-pulsed mode. Experiments were performed to determine whether any increase in pumping efficiency occurred in these modes. Simmering caused little improvement, but prepulsing (with about 2% the main pulse energy, applied 1 msec before the main pulse) typically enhanced the gain by about 10%. This prepulse enhancement has also been noted by workers at LLNL, who conjectured that the prepulse causes residual ionization in addition to the simmer streamer, which speeds the breakdown and enhances plasma uniformity on the main pulse [Erlandson]. For our

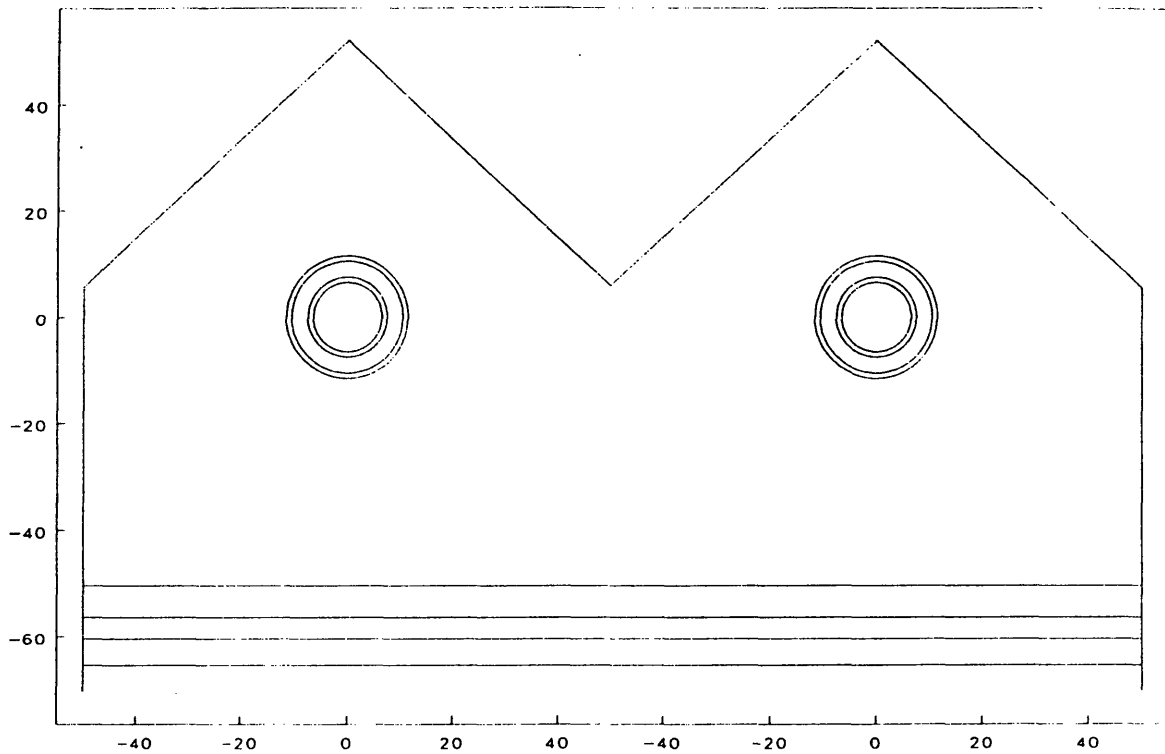


Figure 4.6: Pump cavity design in cross section

purposes, the gain improvements were judged insufficient to warrant the complexity and potential unreliability of the prepulsed/simmered circuit, and the system currently runs in the standard mode.

## 4.7 Pump cavity design

The pump cavities were designed to provide uniform, efficient illumination of the slab. A double-peaked “birdhouse” reflector similar to those used in the early LLNL HAP program was designed; the interior design is shown in cross section in Figure 4.6.

In order to optimize the geometric shape of the birdhouse roof and to predict the pump efficiency, a 2-1/2 dimensional Monte Carlo code was devel-

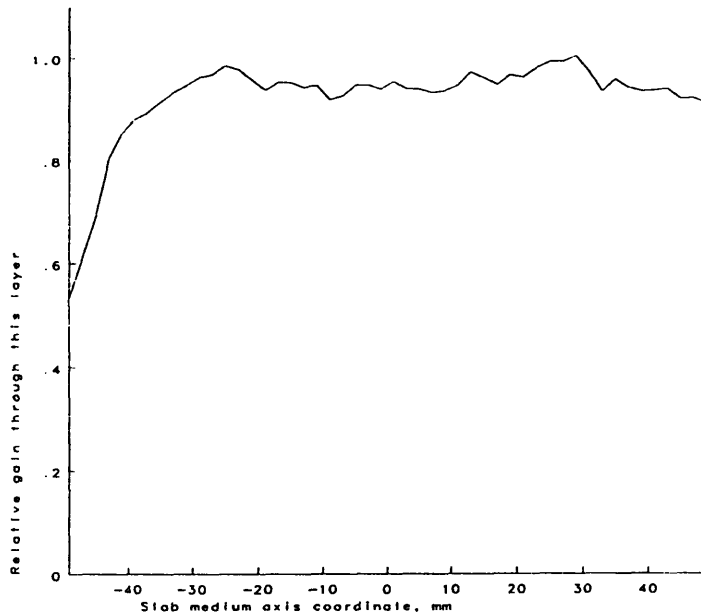


Figure 4.7: Predicted gain profile over one lamp

oped. This code produced light rays randomly oriented in 3 dimensions and propagated them inside a volume with the cross section shown in Figure 4.6 (symmetry is used to reduce the volume to one-quarter that shown). Rays were assigned wavelengths consistent with the xenon lamp output spectrum, and reflectivities were evaluated at each bounce off the silver reflectors using the wavelength-dependent optical constants of silver. Typical runs involved up to  $10^5$  rays (on a 386-25 microcomputer, execution times were about 1 hour), and the statistical noise in the output was about 5% when 100 output bins were used.

This code was used to converge on a suitable set of cavity dimensions; the design was close to that of the HAP group 'C' head. The design was then checked by E. Goodwin using a single run of LLNL's fully 3-dimensional cavity modeling code. The predicted gain profile for the region over one lamp appears in Figure 4.7. Aside from statistical noise, it is flat across most of the slab. The measured gain profile across the whole slab is shown in Figure 4.8 for two values of the pump energy and can also be seen to be reasonably flat.

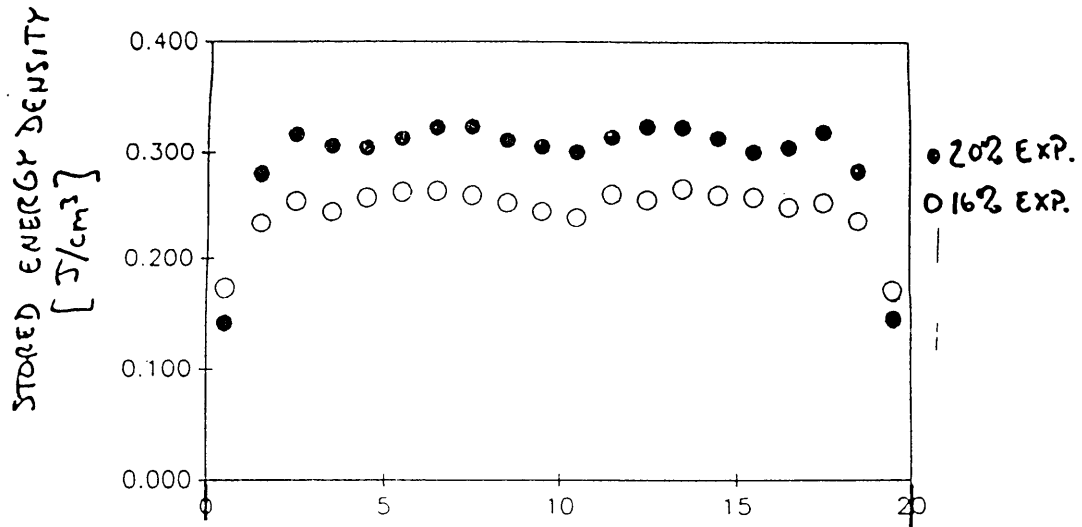


Figure 4.8: Measured gain profile across slab

## 4.8 Thermal design and performance

In an ideal face-cooled slab geometry, the thermal distribution is 1-dimensional across the slab thickness. Because the beam traverses the thermal gradient repeatedly in its zig-zag path, thermal lensing and depolarization are canceled to first order [15]. However, a finite slab will have some residual non-uniformity due to end effects and non-uniform heating and cooling. The cooling system and observed thermal performance of the slab are summarized here.

The forced-air cooling system is shown in Figure 4.9. A high-pressure blower provides a flow of approximately 20 liters/sec through the system. An air-to-water heat exchanger stabilizes the air temperature, and an in-line HEPA filter (99.99% efficiency) provides class-10 clean air for the slab faces. The system is run in a closed loop; three-inch hoses and large ducts are used to minimize pressure loss. The flow Reynolds number at the slab faces is  $\sim 10^4$ , so that the flow is turbulent and the heat transfer rapid and uniform.

At 0.3 Hz, the slab dissipates around 30 W in steady state. Solving the



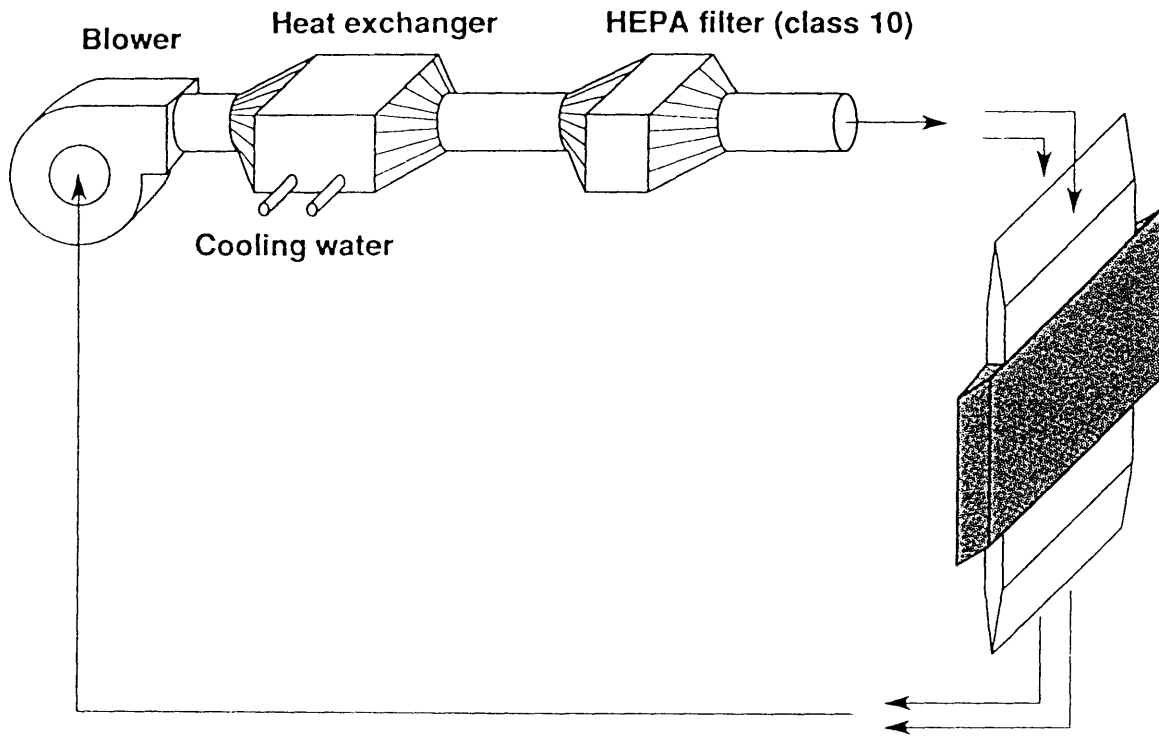


Figure 4.9: Slab cooling system

heat equation for the temperature across the slab thickness gives a parabolic profile. The heat transfer from the slab faces to the air can be calculated using data from [16] for a turbulent flow. The following results are obtained:

Temperature difference across slab thickness = 1.0 K

Temperature difference from slab top to bottom = 1.2 K

Temperature difference between slab and air = 8.4 K

The temperature gradients are quite small for a slab laser, so thermal distortions and depolarization are expected to be insignificant. This is especially true since the laser is not customarily run at 0.3 Hz but rather at only one shot per 30 sec.

The thermal performance of the system was studied by several means. The far-field pattern of a beam passed through the slab was viewed with a CCD camera and monitored while the average power was increased; little perturbation of the beam could be discerned. The depolarization was measured with crossed polarizers and was found to be under 2% throughout the laser power range.

A large beam was passed through the slab and focused through a pinhole, and the transmission monitored; the beam quality went from  $1.2\times$  diffraction limited at zero power to  $1.5\times$  diffraction limited at 1000 W input power (Figure 4.10). This performance is satisfactory for the present needs.

## 4.9 Mechanical construction

A mechanical structure for the amplifier head was designed which is modular and provides straightforward access to the laser components. A photograph of the structure is reproduced in Figure 4.11, which may be compared with the

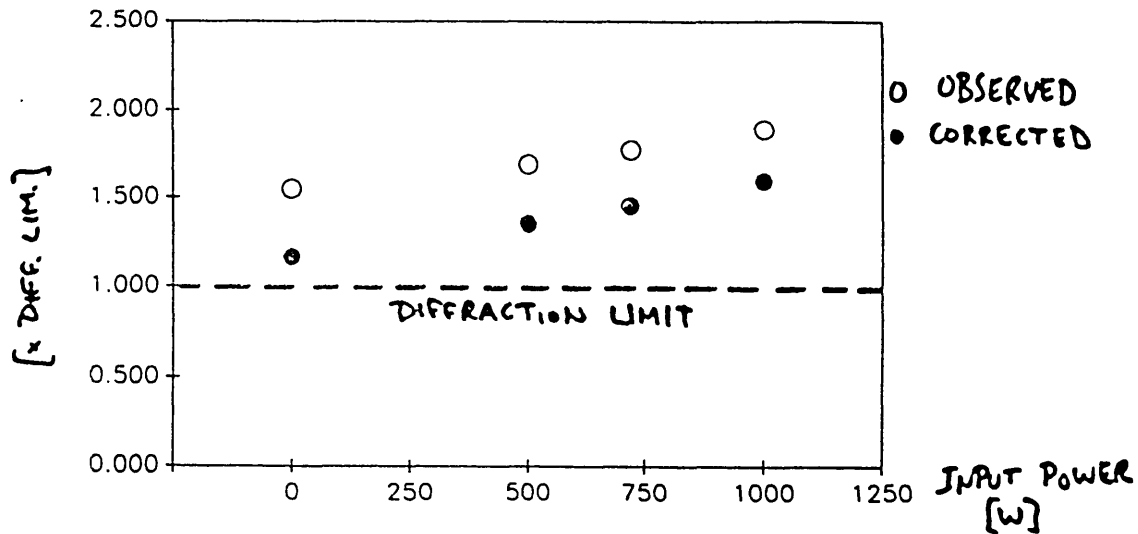


Figure 4.10: Beam quality ( $\times$  diffraction limit) versus pump energy

schematic in Figure 4.1. The cooling air ducts and hoses are visible prominently at the top and bottom. The slab protrudes slightly from each end of the head. The four flashlamps, with their high voltage and cooling water connections, can be seen protruding from the pump cavities. All parts are aluminum, and all except the pump cavities are black-anodized.

The glass slab is held at its top and bottom cladded edges in a vertical fixture that allows handling of the slab outside of the head structure. Tapered vanes split the airflow into the two channels over the slab faces. A 2 mm thick layer of Dow Corning Sylgard Q3-6605 heat-conductive elastomer is used to bond the edge cladding to the vanes; this material prevents thermo-mechanical stress to the slab and also allows the vanes to serve as heat sinks for the cladding, which would otherwise become hot in use.

The pump cavities were fabricated from single blocks of 6061-T6 aluminum; the internal surfaces were finished to 16 microinches roughness, nickel-plated, and polished. A Denton Vacuum FSS-99 first-surface silver coating, with 98% reflectivity throughout the visible, was then applied. The cavities are easily

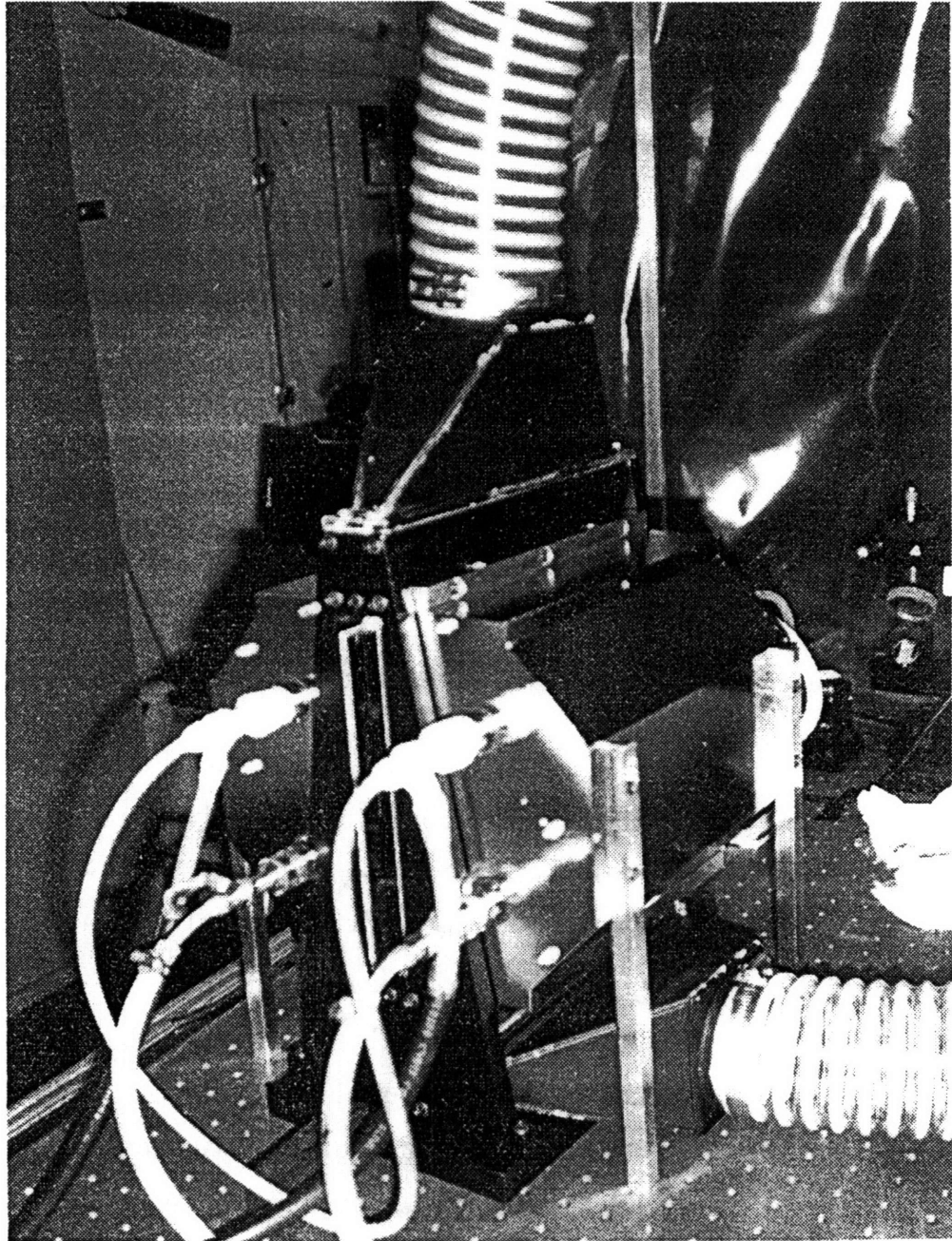


Figure 4.11: Slab amplifier head structure

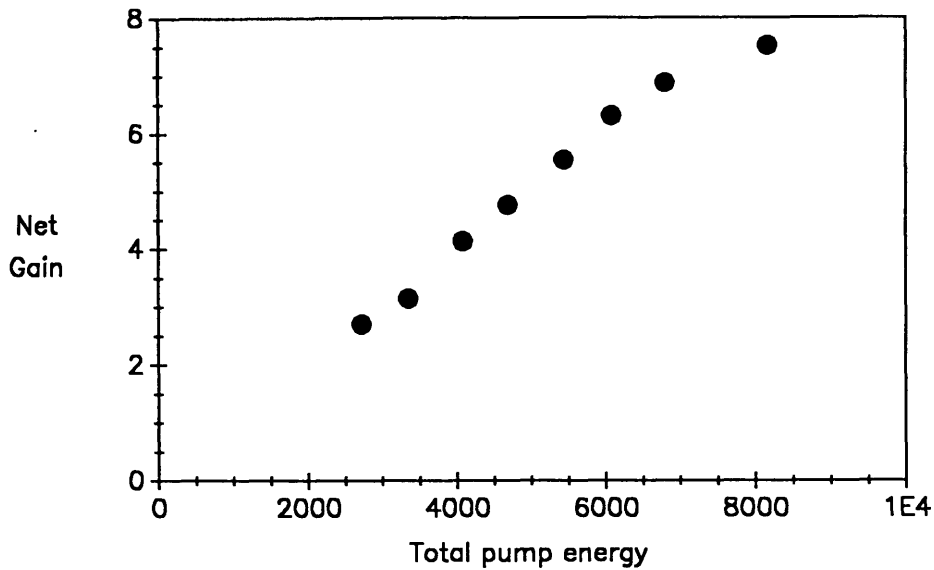


Figure 4.12: Measured slab gains

removable from the laser head for access to the slab or the flashlamps.

## 4.10 Gain and storage efficiency measurements

The measured gains for the slab amplifier are presented in Figure 4.12. The highest achieved gain was about 7.5, measured at 8160 J; this represents, to our knowledge, the highest single-pass gain observed to date on a Nd:glass slab amplifier.

Using these measurements, the stored energy densities and storage efficiencies were inferred. These quantities are plotted against one another in Figure 4.13. Some of the decline in storage efficiency with increasing stored energy is attributed to blue-shifting of the lamps at increased currents. The sharp decline near  $0.45 \text{ J/cm}^3$  is suggestive of increasing ASE and possibly the approach of a parasitic threshold.

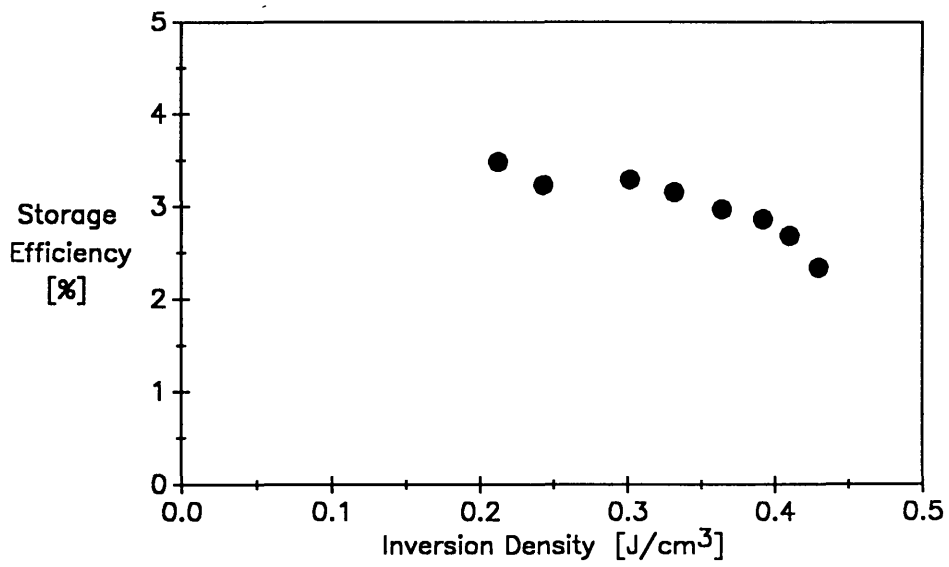


Figure 4.13: Storage efficiencies versus stored energy densities

# Chapter 5

## Optical system

### 5.1 Overview

This chapter reviews the laser optical system and summarizes some of the particular issues involved with the propagation of a non-gaussian beam through the amplifier stages.

A schematic of the optical system is given in Figure 5.1. The oscillator output passes through a pulse selector to extract the desired pulses, then through an  $f/60$  spatial filter with a  $250\ \mu\text{m}$  diamond pinhole. The beam is expanded  $4\times$  and impinges on a bead-blasted 7 mm apodizer (Apodizer 1), which converts it from a gaussian profile to a near-flattop. The beam double-passes the preamplifier and a Faraday isolator, is expanded to 12 mm radius and truncated by a square serrated aperture (Apodizer 2) to form a 10 mm square. It passes through an  $f/60$  vacuum spatial filter with a  $600\ \mu\text{m}$  gold-plated pinhole, passes once through the slab, is expanded by a factor of 6 in one direction by a set of anamorphic prisms and passes twice more through the slab to emerge at full power as a  $10 \times 60$  mm beam. This beam is then focused on the target by cylindrical optics.

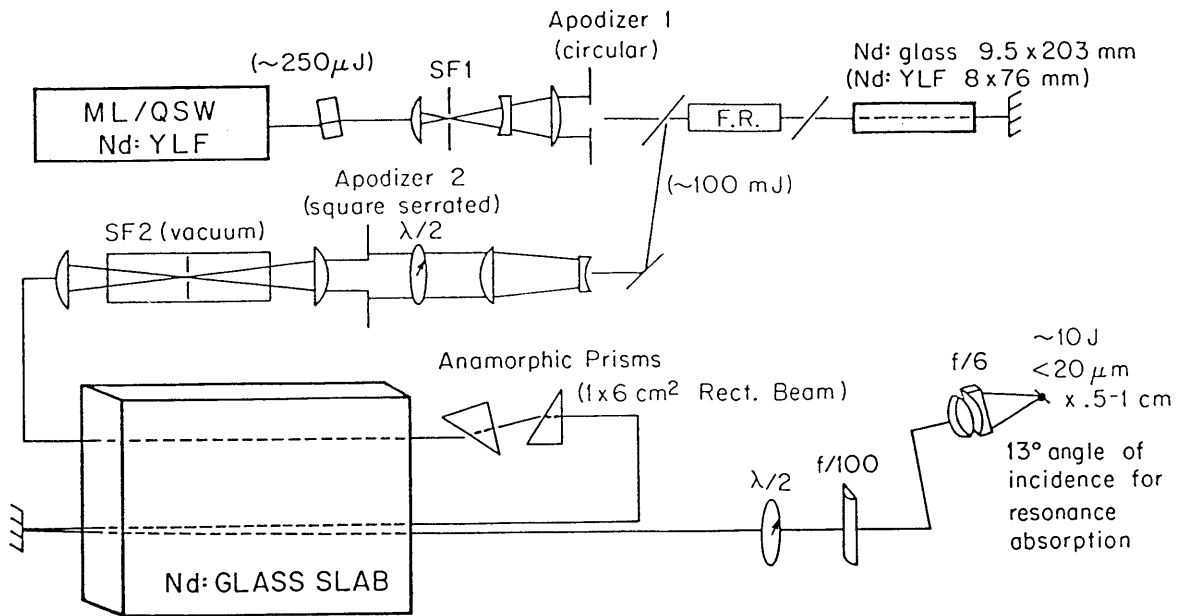


Figure 5.1: Optical system schematic

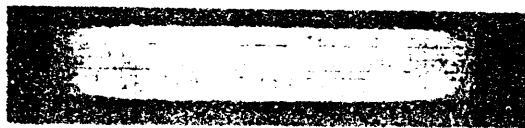


Figure 5.2: Example of burn pattern from slab amplifier output

A burn pattern showing the size and shape of the output beam is reproduced in Figure 5.2. Slight near-field diffraction ripples due to the flattop beam profile can be seen.

The double-passing of the preamplifier has been done both using a Faraday isolator, as shown here, and using a quarter-wave plate and polarizer, with the isolator in the output beam. The first configuration offers doubled isolation but is prone to parasitic lasing between the end of the isolator rod and the rear mirror. The second offers lower losses but is more sensitive to thermal depolarization by the preamplifier rod.



The optical system is configured to be able to generate two  $10 \times 60$  mm 1-J output beams. Normally only one beam is extracted; inserting a beam splitter on a kinematic mount before the slab slices off a second beam which is amplified in parallel to the first.

## 5.2 Non-gaussian beam propagation

### Introduction

Because the laser system performance is limited mainly by the intensity damage threshold of bulk media, it is necessary to use apodized, near-flattop beams with high fill factors and steeply falling edges. This maximizes the safe power level and prevents sharp diffraction ripples caused by clipping of the wings of gaussian pulses by hard edges [7].

The use of non-gaussian beams means that near-field diffraction will distort the pulse profile during propagation [10]. The resulting ripple is dangerous for bulk optical components since the  $B$  integral causes it to grow. The ripple can be minimized by judicious tailoring of the apodization function and by relay imaging. Both of these techniques were used in this system and will be discussed here briefly.

### Circular beam region

A 1-dimensional beam propagation code was developed to model the propagation of the circular non-gaussian beam from Apodizer 1 through the preamplifier to Apodizer 2. The code evaluates the Huygens integral numerically in circular geometry for an arbitrary input beam profile. A variety of apodizer profiles were studied, including supergaussian, parabolic, and various hybrid functions.

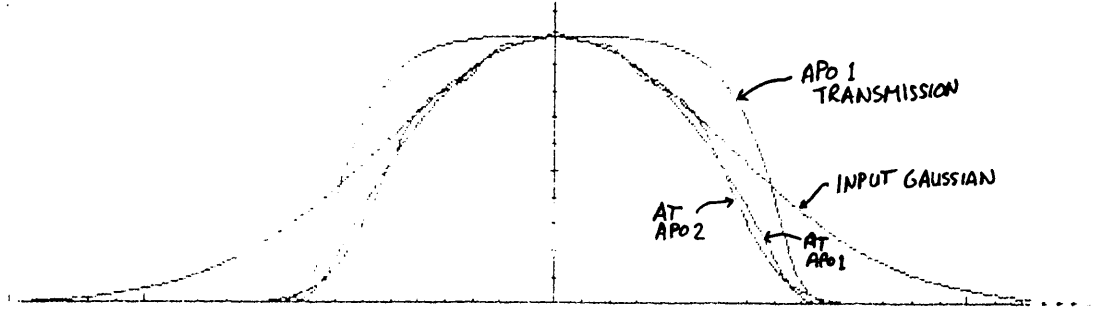


Figure 5.3: Calculated beam profile at Apodizer 2 using spliced parabolic profile

For the first version of Apodizer 1, a spliced parabolic beam profile was used that had originally been suggested by workers at LLNL [7] [5]:

$$I(r) = \begin{cases} 1 - 1.3r^2 & 0 < r < 0.79 \\ 0.3 \exp\left(-\left(\frac{r-0.71}{0.124}\right)^2\right) & 0.79 < r < 1 \end{cases}$$

The computed beam profile at Apodizer 2 for propagation from Apodizer 1 is shown in Figure 5.3. Because the spliced parabolic mimics a gaussian profile fairly well and has very smoothly falling edges, the beam does not suffer significant distortion over this propagation distance.

A metallic-film apodizer to generate the required intensity profile was fabricated by Reynard Enterprises. It produced excellent results and was in service for over one year. The metallic film was unfortunately not highly damage resistant and was degraded in time by slight parasitic lasing between it and the double-pass preamplifier.

A second, higher-damage-threshold optic for Apodizer 1 was fabricated by a bead-blasting process by Continuum. The transmission profile could not

be as accurately controlled on this apodizer, and the optical density gradient was considerably steeper. Using the measured transmission function, the apodizer was modeled; also, the actual beam profile was measured at plane of Apodizer 2 using a Reticon diode array. The results of theory and experiment are compared in Figure 5.4. The input beam to the apodizer was insufficiently expanded, and therefore the ripples on the experimental data are somewhat low. The size and number of ripples agree well, however. A lineout of the non-apodized gaussian beam, after clipping by the preamplifier rod, is also shown as justification of the need for apodization.

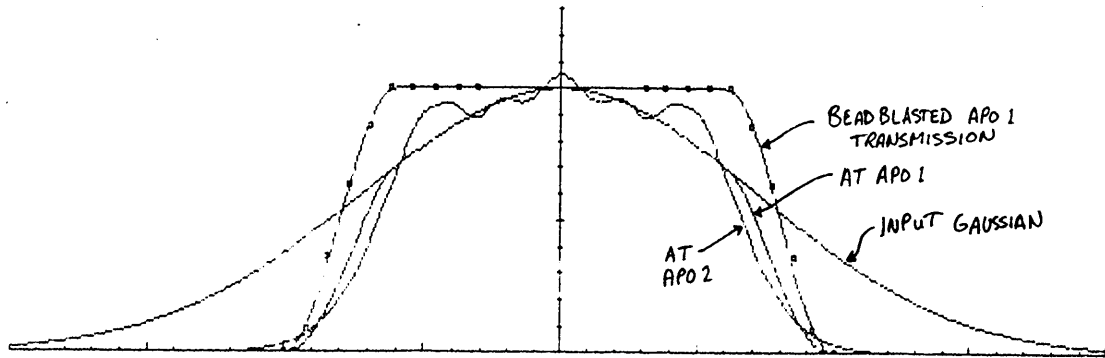
Ripple growth is considerable using the bead-blasted apodizer; if this apodizer continues to be used, the beam diameter through it should be reduced to make the transmitted beam more nearly gaussian. Such a beam will work well with the reduced clear aperture of the 8 mm Nd:YLF rod.

## **Rectangular beam region**

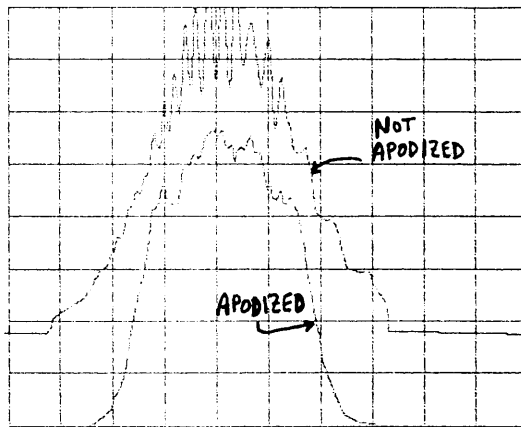
Beam propagation dynamics following the square serrated aperture (Apodizer 2) are much more complex than in the circular region. Since a square beam is being sliced out of a round profile, the resulting beam has neither rectangular nor circular symmetry and should be studied using 2-dimensional modeling. Moreover, spatial filtering must also be studied in 2 dimensions. The analyses leading to the present design were done with the assistance of J. Hunt and J. Lawson at LLNL.

Apodizer 2 is a square aperture, laser-machined out of stainless steel, with fine serrations lining its edges (Figure 5.5). The profile of the serrations defines the resulting beam profile; the serration pattern itself is removed by the vacuum spatial filter.

The apodizer serration frequency, the spatial filter focal length, and the



CALCULATED



MEASURED

Figure 5.4: Calculated and measured beam profiles at Apodizer 2 using bead-blasted apodizer

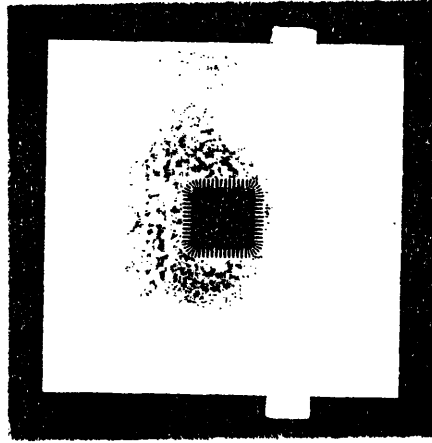


Figure 5.5: Square serrated aperture

pinhole size are mutually dependent. Relevant issues to the correct design of the apodizing system include the following:

- the spatial filter must remove the serration pattern, yet maintain the desired apodized beam profile
- the spatial filter should avoid introducing far-field diffraction ripple into the profile
- the serrated aperture must be able to be fabricated satisfactorily (the present design is near the limit for laser machining; some imperfection can be seen in the ripples)
- pinhole erosion must be minimized by using low intensities, large pinholes, and suitable pinhole materials
- pinhole closure (plasma generation at the pinhole by the clipped portion of the focused beam, leading to massive beam refraction) must be avoided, using high  $Z$  pinhole materials and, again, low intensities and large pinholes [LLNL Ann Rep]

Selection of a number of serrations of about 20 per side and a spatial filter cutoff frequency of about 6 times the fundamental gave satisfactory results for

the present system. Standard stainless steel pinholes are unsuitable for high intensity use due to the last two of the above requirements; suitable materials include molybdenum, tungsten, gold-plated copper, and diamond (synthetic diamond wire dies are popular and seem to work well in spite of low  $Z$ ).

The vacuum spatial filter relays the filtered image of Apodizer 2 forward by twice the focal length, i.e. 1 m. Here, the beam uniformity is maximized, and the optical path is therefore arranged such that this point corresponds to near the high-intensity passes through the slab. The high uniformity here was verified experimentally.

As the beam continues to propagate beyond that point toward the target, diffraction ripples build up. This is a concern because ripples in the short dimension will result in ripples along the length of the line focus, which are not in general desirable for the x-ray laser.

The ripple growth is controlled by the Fresnel number [10],

$$F = \frac{(a/2)^2}{\lambda L},$$

where  $a$  is a transverse dimension and  $L$  the propagation distance. Since the beam is rectangular, the two dimensions develop ripple at different rates, the narrow dimension 36 times faster than the long dimension. In the distances of interest, the beam experiences essentially no diffraction in the long dimension, whereas in the narrow dimension, it experiences considerable ripple growth since  $F < 10$ .

A version of the beam propagation code was developed for rectangular symmetry and run to determine approximately how these ripples in the narrow dimension behave. Figure 5.6 shows the transverse beam profiles after propagation distances of 4 m (the current distance from slab to target chamber) and 12 m. The beam rapidly becomes unusable at distances over 4 m; if a longer propagation distance is needed, diffraction must be reduced using either relay

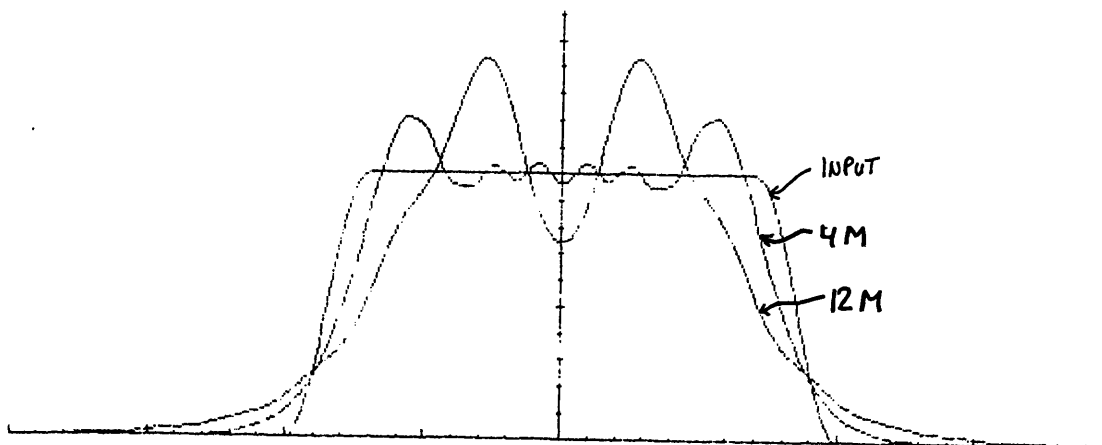


Figure 5.6: Beam profiles after propagation of 4 m and 12 m from the image plane of Apodizer 2

imaging in a second vacuum spatial filter or beam expansion.

The calculated profile at 4 m is in reasonable agreement with experimental observations. A Reticon diode array was used to measure the beam profile at 4 m compared to at the image plane of Apodizer 2. The results are shown in Figure 5.7. The intensity variation across the beam at 4 m is about  $\pm 10\%$ , which is acceptable for x-ray laser experiments.

A 2-dimensional modeling capability needs to be developed in order to expedite design calculations for the optical system in the regions lacking rectangular or circular symmetry. This will lead to greater understanding of both the spatial filtering process and the growth of diffraction ripples.

### 5.3 Cylindrical focusing optic

The long dimension of the beam is line-focused on the target by a cylindrical lens aplanatic lens doublet of 400 mm focal length. A second, orthogonally

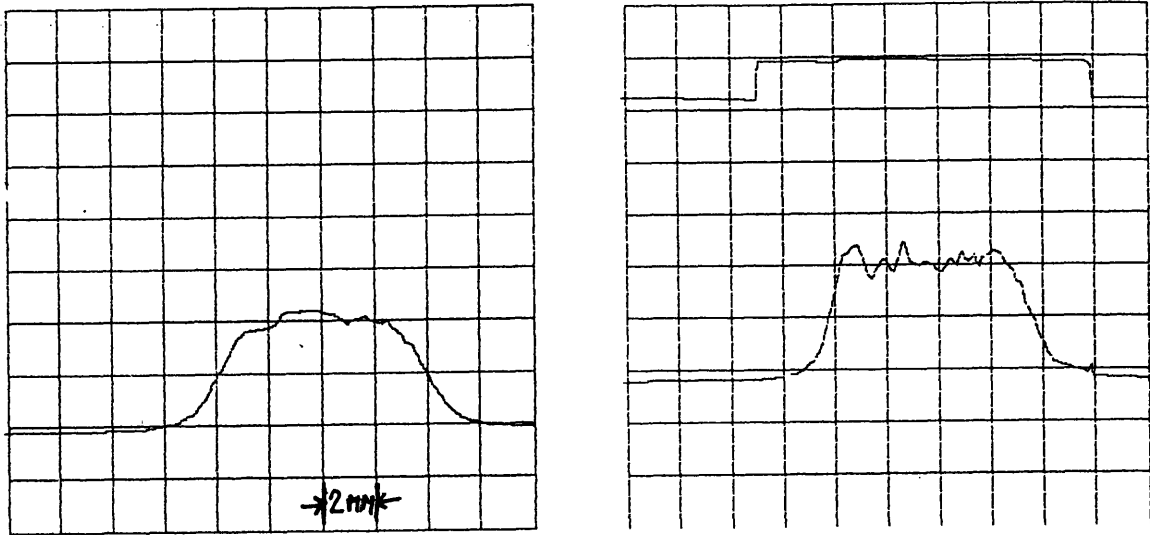


Figure 5.7: Observed beam profile at apodizer image plane and after 4 m propagation

oriented cylinder lens, of 1000 mm focal length, adjusts the length of the line (the arrangement is visible in Figure 5.1).

A doublet design was chosen because a singlet would suffer excessive spherical aberration, and cylindrical aspheres are prohibitively expensive. Large cylinder lenses good to  $\lambda/5$  can be custom fabricated at reasonable cost. The doublet was initially designed using third-order aberration theory; the two lenses offer enough degrees of freedom to correct both sphericity and coma. A ray-trace code was written to optimize the design once an appropriate regime had been found.

The performance of the doublet was verified by measuring the line focus width with a  $10\times$  magnifying optical arrangement and a Reticon diode array. Traces for both the doublet and the 1000 mm singlet acting on the 60 mm beam dimension are shown in Figure 5.8. The singlet had been interferometrically verified to under than  $\lambda/5$  and was essentially diffraction limited in this application; it generated a FWHM of  $25\ \mu\text{m}$ , which suggested that the laser



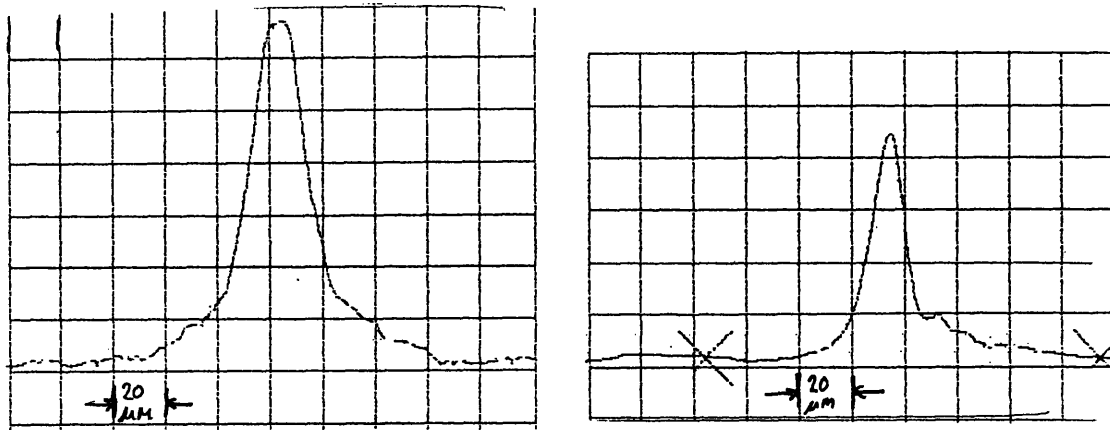


Figure 5.8: Focal plane beam profiles for cylindrical singlet and doublet. Note that a vertical scale change has occurred between the two pictures.

output was about  $1.5\times$  diffraction limited. The 400 mm doublet produced a  $14\ \mu\text{m}$  line focus width, which was about  $2\times$  diffraction limited. It could be concluded that the optical quality of the doublet was on the order of  $1.5\times$  diffraction limited.



# Chapter 6

## Collisionally excited x-ray laser theory overview

### 6.1 Collisionally excited schemes

#### Pumping mechanism

In this and the following chapter, some of the basic physics underlying the x-ray laser scheme is presented. This section gives an overview of the considerations that led to the present design. Following sections explore some aspects of the plasma physics to show that the required plasma conditions can be achieved by our system.

Collisional pumping of x-ray lasers uses electron-ion collisions to populate a radiatively metastable ionic level and create an inversion [1]. Achieving an inversion requires the plasma to be in a non-local-thermal-equilibrium (non-LTE) state. Relative to an LTE situation, the density must be lowered and the temperature raised in order for the plasma to have the desired characteristics for development of an inversion.

A criterion for full LTE to hold in a plasma is given by Griem [17]:

$$n_e \geq 9 \times 10^{17} \left( \frac{\Delta E}{I_H} \right)^3 \left( \frac{T_e}{I_H} \right)^{1/2} \text{ cm}^{-3},$$

where  $n_e$  is the electron density,  $T_e$  the electron temperature,  $\Delta E$  the principal resonance line energy of the ion, and  $I_H = 13.6$  eV the Rydberg energy.

Under this condition, the electron density is sufficiently high, the electron temperature sufficiently low, and the plasma sufficiently optically thin, that all transition rates are dominated by electron-collisional excitation and ionization processes and their detailed-balance inverses. Radiative rates are insignificant; the ionic energy levels are populated according to a Boltzmann distribution, and the ionization states according to Saha equations (Section 6.7). For the plasmas which we will be considering here, LTE would hold at densities upward of  $10^{22} \text{ cm}^{-3}$ .

At decreased electron density from the LTE regime, excitation and ionization are still predominantly collisional, but de-excitation and recombination have significant contributions from radiative or other (e.g. inverse Auger) processes. Level population calculations must be done using all relevant transition rates, and a Boltzmann distribution is not obtained. As is the case for neutral atoms, highly excited states of ions have much slower radiative decay rates than lower-lying excited states; in the Rydberg levels of ions in this regime, radiative decay can be small compared to collisional de-excitation. The levels above the so-called collision limit will then be in LTE, while those below it remain in non-LTE. Qualitatively, then, there arises the possibility that a higher-lying level could have a higher population than a lower-lying one that radiatively decays quickly. This is particularly true if the upper level is radiatively metastable.

Collisionally pumped x-ray laser schemes are based on the fact that, for a ground state  $nl$ , the excited state  $(n+1)l$  is strongly pumped by the electron-

collisional monopole excitation process  $nl \rightarrow (n+1)l$  but is metastable against direct radiative decay to the ground state, so that a large population can develop there. The lower-lying state  $(n+1)(l-1)$  is strongly radiatively coupled to the ground state and thus its population remains small (typical energy-level diagrams for these states appear in Figure 6.1).

Under appropriate conditions (low enough density that collisional destruction of the upper state does not occur, and high enough temperature to drive the excitation, for example), then, lasing can occur between the levels  $(n+1)l$  and  $(n+1)(l-1)$ . Since  $\Delta n = 0$  for this laser transition, the output photon energy is small relative to the excitation energy and the electron temperature. Achieving short x-ray laser wavelengths with this approach requires, in general, the use of highly stripped, high  $Z$  ions and consequently high pump laser powers.

The collisional monopole transition term is vital to this laser scheme. A description of the multipole expansion of the collisional excitation process under the Born approximation is given by Sobelman [18]. Since the collisional process is not governed by the radiative selection rules, a monopole transition is allowed. Also in contrast to the radiative case, the collisional terms do not rapidly decrease with increasing multipole order; thus the monopole term is of the same order as the dipole terms, whereas neighboring radiative terms differ by a factor of order  $1/137^2$ .

## Comparison of ionic sequences

In principle, any ion with a ground state having its outer electron in an  $l \geq 1$  orbital could be used for this scheme. The selection of ionic sequence can be guided by considerations of the ease of producing and maintaining the ion, and of how the output wavelength and gain relate to the required pump

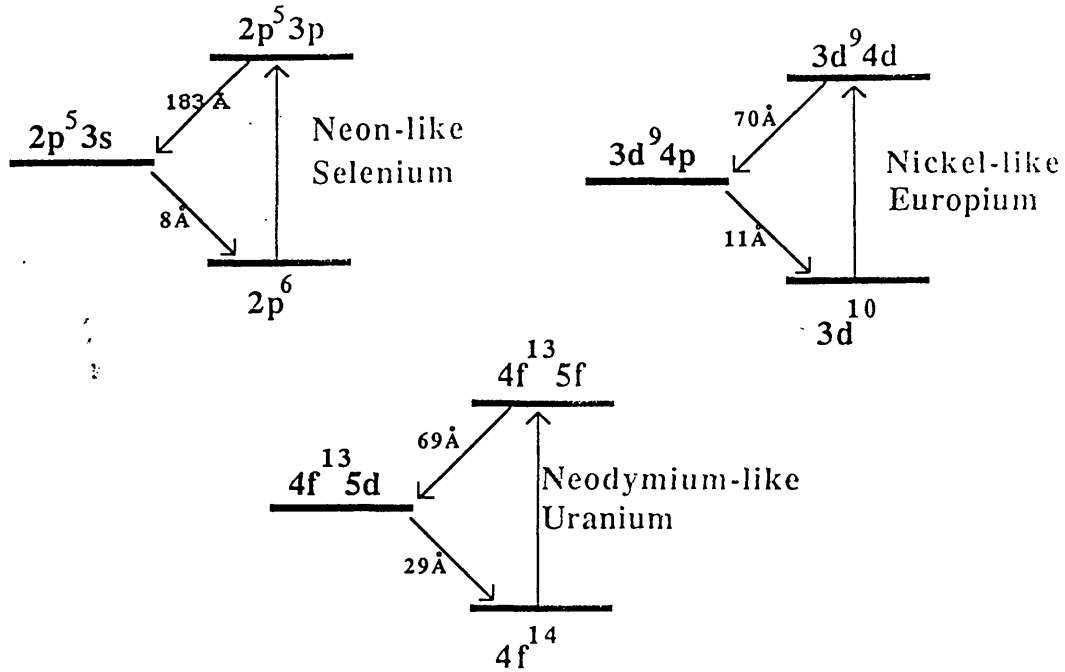


Figure 6.1: Energy level diagrams for collisional lasers [21]

power. Within a sequence, the selection of element to use ( $Z$ ), and thus output wavelength, is made to match the ion's excitation energy with the attained electron temperature, which is governed by the available pump power.

At moderate to high ionization, closed-shell structures analogous to those of the noble gases are exhibited by the ions isoelectronic to Ne ( $1s^2 2s^2 2p^6$ ), Ni ( $1s^2 2s^2 2p^6 3s^2 3p^6 3d^{10}$ ), and Nd ( $1s^2 2s^2 2p^6 3s^2 3p^6 3d^{10} 4s^2 4p^6 4d^{10} 4f^{14}$ ). These ions have elevated ionization potentials and will therefore offer the greatest stability, longevity and fractional abundance of the various ionization states that will typically coexist in a thermal plasma. For this reason most research efforts have been focused on these species [1] (some searches have also been made for lasing in F-like ions in overionized Ne-like plasmas [unsuccessful] [19], and in Co-like ions in overionized Ni-like plasmas [successful] [20]). Energy level diagrams illustrating the three schemes in representative ionic species appear in Figure 6.1.

Use of the Ne-like sequence was originally proposed by Soviet researchers in the early 1970's [22]; some early experiments were reported in 1977 on Ne-like Ca (laser line near 600 Å) using a 30-J Nd:glass pump laser [23]. The

LLNL effort in 1983 in Ne-like Se produced convincing evidence of about 6 gain lengths of amplification at 206 Å and 209 Å[3]. With increased drive energy, the scheme was demonstrated in Ne-like Y (155 Å) and Ne-like Mo (106 Å). Of the various collisional schemes, the Ne-like still appears to be the most robust and reliable; the Se and Y lasers have been driven into saturation (15-20 gain lengths) and are currently being used in x-ray laser applications research [72].

Ne-like lasers suffer from the fact that the laser photon energy ( $3s-3p$ ) is very small compared to the  $2p-3p$  excitation energy, as can be seen in Figure 6.1; the laser is consequently very inefficient. As one goes to higher principal quantum number, in Ni-like and again in Nd-like, it can be seen that the laser transition becomes proportionately larger compared to the excitation, and the lasers become more efficient. As one varies  $Z$  within the three sequences, the efficiency changes somewhat (the excitation energy is proportional to  $Z_{\text{eff}}^2$  and the laser transition to a somewhat lower power of  $Z_{\text{eff}}$ ) but the variation is insignificant compared to the difference between sequences.

Another fact which tends to make the Ni-like lasers more efficient, and should make the Nd-like even more so, is that the monopole collision strength for the excitation from the ground state to the upper laser state increases with principal quantum number [24]. The trend, for the closed-shell sequences, can be seen in Figure 6.2.

The total collision strength  $\Omega(Z)$  is shown scaled by  $\Delta E(Z)/NI_{\text{H}}$ , where  $\Delta E(Z)$  is the threshold excitation energy,  $N$  is the number of electrons in the outermost subshell (2, 6, 10 or 14), and  $I_{\text{H}} = 13.6$  eV. Thus scaled, the collision strengths are fairly constant within an isoelectronic sequence, and they increase somewhat as we go from He-like to Ne-like to Ni-like to Nd-like. This increase becomes much more dramatic when we consider the actual

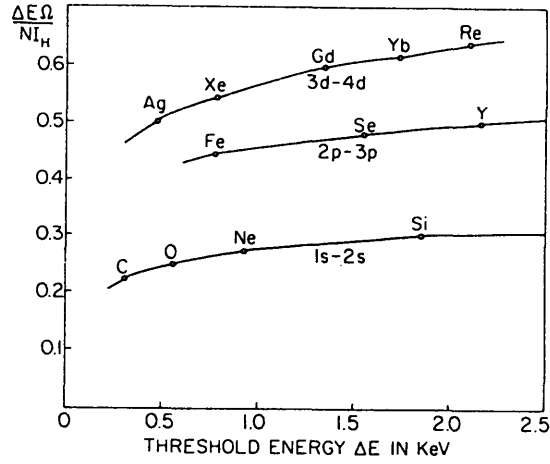


Figure 6.2: Monopole collision strengths (from [24])

unscaled value,

$$\Omega(Z) = (\text{value from Fig 6.2}) \times NI_H / \Delta E(Z) \quad (6.1)$$

for a given, fixed output laser wavelength, because as mentioned previously, the excitation energy  $\Delta E$  drops markedly with an increase in principal quantum number, and also the number of electrons  $N$  increases (more available electrons means a higher probability of one of them getting excited).

There are, on the other hand, several factors working against the benefits of using higher- $n$  sequences. In the first place, the higher sequences are not so energetically stable as the Ne-like, i.e. the population will be spread out over more adjacent charge states, and the optimal fractional abundance of the desired species in the plasma will be lower.

A practical limitation with the Nd-like sequence is that whereas for both the Ne- and the Ni-like sequences, there are elements of appropriate  $Z$  available to match pump power from a few J to several kJ, with Nd-like ions, the highest plausible  $Z$  is 92 (U), which requires on the order of 10 J pump energy. While this will give an extremely efficient laser around 70 Å, the scheme cannot be scaled to any shorter wavelengths, whereas the Ni-like sequence could extend



below 30 Å using tens of kJ and  $Z$  in the mid 80's.

The Ni-like and Nd-like ions are much more complicated than the Ne-like. For example, there are on the order of 100 allowed  $4p-4d$  transitions in Ni-like ions and far fewer  $3s-3p$  transitions in Ne-like species, so the oscillator strength is divided more finely at higher  $n$ . Also, the presence of more levels fractionates the population more; in particular, the emergence of the metastable states  $4s$  (in Ni-like) and  $5s$  and  $5p$  (Nd-like) is a concern. The  $4s$  turns out to lie sufficiently high that it does not consume much of the Ni-like population, but the low-lying  $5s$  and  $5p$ , according to simulations for Nd-like U, will contain most of the Nd-like population and so drastically reduce the expected gain [25]. The increased complexity of these ions also makes kinetics modeling more difficult to perform and/or less reliable.

A final concern is trapping of the laser dump transition radiation. If the spatial extent of the plasma is sufficiently large, the dump transition (e.g.  $2p^5 3s-2p^6$  for Ne-like ions) becomes optically thick, and excitation of the lower laser state—rather than being immediately dumped—is passed around from one ion to another. This radiation trapping effectively increases the lower laser state lifetime and reduces the inversion. Using the expression from Griem [17] for the opacity of a Doppler-broadened line gives

$$\tau = \left( \frac{\pi M_i c^2}{2T_i} \right)^{1/2} r_0 n_i \lambda_{\text{dump}} f d \quad (6.2)$$

where  $M_i$  is the ionic mass,  $T_i$  the ion temperature,  $n_i$  the ion density,  $f$  the oscillator strength, and  $d$  a characteristic plasma size. If  $\tau$  is on the order of unity or higher, then trapping can be expected to be significant, and more sophisticated ray-trace analyses would be worthwhile. Both  $f$  and  $\lambda_{\text{dump}}$  increase with higher  $n$  sequences, and scaling down in  $Z$  within a sequence toward longer laser wavelengths increases  $\lambda_{\text{dump}}$  also. Therefore, while trapping has not been verified to date in experiments in Ne-like or Ni-like lasers, it could

be a significant issue for the longer-wavelength Ni-like and the Nd-like schemes in which we are interested.

Research was undertaken in the mid-1980's on demonstrating gain in the Ni-like sequence. Gain has been observed throughout the range from 35 Å (Ni-like Au) to 71 Å (Eu), as compared to the range from 106 Å (Ne-like Mo) to 236 Å (Ge) [72] for comparable pump energies, in agreement with the expectation of increased efficiency. Some preliminary investigations have also been performed on Nd-like U [21]. Some 4–5 spectra taken using a large Nd:glass laser suggested the presence of the Nd-like species at intensities in the  $10^{13}$  W/cm<sup>2</sup> range, but neither the  $4f$ – $5d$  dump transition in the 30 Å region nor the transitions to the  $5s$  and  $5p$  metastables could be conclusively identified.

Because the Ni-like sequence was fairly well understood and had been shown to scale in  $Z$  reasonably, it was chosen as the primary candidate for x-ray laser studies at the outset of our program. Some work is likely to be done on Nd-like systems since their excitation energy is well matched to our capabilities, and the output wavelength is far shorter than those available to us in Ni-like systems. At long wavelengths ( $\lambda > 350$  Å) the Ne-like sequence will be accessible as well.

## Selection of $Z$ for Ni-like studies

The electron temperature  $T_e$  is related to the absorbed pump intensity  $I_{\text{abs}}$  by [26]

$$T_e = 0.06 \times (I_{\text{abs}} \lambda_{\text{pump}}^2 / f)^{2/3}, \quad (6.3)$$

where  $T_e$  is in eV,  $I_{\text{abs}}$  is in units of W/cm<sup>2</sup>,  $\lambda_{\text{pump}}$  is in cm, and  $f \sim 0.03$ – $0.1$  is a phenomenological constant, as will be discussed in greater detail in Sections 6.3 and 6.5. Using our laser system, with a line focus size of about

$Z$	$I_P$ [eV]	$E_{\text{exc}}$ [eV]	$\lambda$ [Å]
32	93	59	748.0
34	155	98	462.4
36	232	143	337.3
38	324	194	266.8
40	429	250	221.0
41	486	280	203.7
42	545	311	188.8
44	673	377	164.7
46	812	449	146.0

Table 6.1: Low- $Z$  Ni-like x-ray laser parameters [27] (some values of  $I_P$  have been extrapolated from tabulated values using  $Z_{\text{eff}}$ )

1 cm by 20  $\mu\text{m}$ , we can expect to generate electron temperatures on the order of 150-200 eV.

Table 6.1 shows ionization energies, excitation energies and laser wavelengths for low- $Z$  Ni-like species [27]. Typically one can expect to have a sizable fractional population of a species if the electron temperature is within a factor of three of the ionization energy. Significant excitation by the high-energy tail of the electron Maxwell-Boltzmann distribution will occur on the  $3d-4d$  transition if the temperature is within a factor of about two. Thus it appears that elements in the neighborhood of Mo ( $Z = 42$ ) will be well matched to the capabilities of our system. These estimates regarding excitation and ionization balance will be verified in Sections 6.2 and 6.7.

## Scaling of pump energy

A quantitative scaling argument can be made to see how, within a sequence, the required pump intensity varies with the desired output wavelength, or equivalently, with the  $Z$  of the lasing material. It is assumed that for pumping the monopole excitation to the upper laser level, the same approximate

region of the electron Maxwell-Boltzmann distribution will participate in the excitation regardless of the scaling. Then the temperature should be proportional to the excitation energy. The laser transition energy is not directly proportional to the excitation energy but rather to a power of it which varies from about 0.5 to 1; in the  $Z$  region of interest, the exponent is about 0.72. Thus we have that

$$I_{\text{abs}} \sim T_e^{1.5} \sim \Delta E_{\text{ul}}^{1.5} \sim \lambda_{\text{laser}}^{-1.5/0.72} = \lambda_{\text{laser}}^{-2.1}. \quad (6.4)$$

This relation can be re-cast in terms of the nuclear charge  $Z$  [28]. The ion is modeled hydrogenically with an effective charge  $Z_{\text{eff}} = Z - \sigma$  used to model the screening effect of the  $N - 1$  inner electrons. Clearly  $\sigma$  varies with  $n$  and  $l$  of the outer electron, depending on the penetration of the orbital into the inner electron core; it can be expected to be less than the perfectly screening value of  $N - 1$  for penetrating orbitals and to tend to that value as  $n$  and  $l$  grow large. The concept of  $Z_{\text{eff}}$  is useful in that  $\sigma$  is largely independent of  $Z$  for high ionization stages, because electron-electron Coulomb energies scale slower in  $Z$  than the electron-nucleus energy, and the orbitals become essentially hydrogenic. We find for  $3d-4d$  transitions near  $Z = 42$  that  $\sigma \approx 22.5$ , as compared with  $N - 1 = 27$ , for a screening effectiveness of 83%. Using the hydrogenic model,

$$\Delta E_{\text{ul}} \sim Z_{\text{eff}}^2,$$

which gives us

$$I_{\text{abs}} \sim Z_{\text{eff}}^3. \quad (6.5)$$

This shows how the required pump intensity is affected by changes in  $Z$  in the region of interest; the output wavelength varies correspondingly as

$$\lambda_{\text{laser}} \sim Z_{\text{eff}}^{-1.4}. \quad (6.6)$$

A change in  $Z$  of 1 in the neighborhood of  $Z = 42$  will change the intensity required by 16% and the output wavelength by 7.5%.

The total power required for a given gain-length product will depend not only on the above scaling for the laser intensity, but also on the scaling of the resulting gain. The stimulated-emission cross section goes as

$$\sigma_{\text{stim}} \sim \lambda^2/\Delta\lambda;$$

as a crude assumption, we can take  $\Delta\lambda/\lambda$  as a constant. This contributes a factor of  $\lambda$  to the scaling of Equation (4), whereby the total power  $P$  required for a given gain-length product scales as

$$P \sim \lambda_{\text{laser}}^{-3.1}. \quad (6.7)$$

These scaling relations, while probably fairly reliable locally, do not seem to explain the very large difference in pump powers between our system near  $Z = 42$  and systems near  $Z = 70$  such as at LLNL. There are other factors to be considered in such a comparison: the high- $Z$  systems optimize at much high electron densities than the low- $Z$ , and consequently refraction of the x-ray laser beam by the plasma becomes a serious issue. A different target design than ours (a thin foil rather than a solid surface) is employed; it uses a larger beam width to lessen density gradients, and it is intended to burn through completely, yielding a relatively constant density in the middle [Rosen]. Typically, frequency-doubled (527 nm) pump radiation is used, because it is absorbed more efficiently and burns through the foil faster. The larger width enters the power scaling linearly, clearly; the altered pump wavelength can be accommodated, according to Equation (3), by using  $I\lambda^2$  or  $P\lambda^2$  rather than  $I$  or  $P$ . Unfortunately, Equation (3) becomes invalid when the foil burns through, but the scaling found when the above factors are taken into account is nonetheless reasonably close to that observed experimentally.

For example, the Eu laser ( $Z = 63$ ,  $\lambda = 71 \text{ \AA}$ ) has been found to operate at an incident intensity of  $7 \times 10^{13} \text{ W/cm}^2$  at 527 nm [72]. This scales to an intensity of  $2.3 \times 10^{12} \text{ W/cm}^2$  at 1053 nm for the Mo laser ( $Z = 42$ ,  $\lambda = 189 \text{ \AA}$ ), in agreement (within a factor of two) with our theoretical and experimental results.

## 6.2 Results from x-ray laser gain model

A three-level model for the Ni-like laser was developed by P. Hagelstein [29]. The relevant results for our effort are listed here.

The peak stimulated emission cross section is given by

$$\sigma = (\lambda^2/2\pi) \times (A_{21}/\Gamma_V),$$

where  $\lambda$  is the laser wavelength,  $A_{21}$  the upper level radiative decay rate, and  $\Gamma_V$  the Voigt linewidth. For the Ni-like Mo system,  $\lambda = 189 \text{ \AA}$  and  $A_{21} = 8.8 \text{ psec}$  (the lower level lifetime, by contrast, is around 1 psec). At  $T_e = 250 \text{ eV}$ ,  $T_i = 10 \text{ eV}$ , and  $n_e = 1.5 \times 10^{19} \text{ cm}^{-3}$ , it is found that the Doppler linewidth is  $2.5 \times 10^{12}$ ,  $\Gamma_V = 3.3 \times 10^{12} \text{ sec}^{-1}$ , and  $\sigma = 1.9 \times 10^{-14} \text{ cm}^2$ . A key feature of this scheme is the low ion temperature, which comes about because of the low electron-ion coupling at low density, and serves to reduce Doppler broadening.

The upper state population depends on the balance between the collisional excitation rate and radiative and collisional decay rates. The excitation rate is shown to be more strongly temperature dependent than the loss rates, so the upper state population increases with increasing temperature. The lower state population involves more contributing processes and is evaluated using an empirical model.

The optimum electron temperature for a fixed total pump power is found

by balancing the increasing excitation strength with increasing temperature against the decreasing amplification distance, since generating higher temperatures requires higher intensities and thus shorter line foci. The optimum temperature is found to be  $T_e = \Delta E_{20}/2$ , where  $\Delta E_{20}$  is the excitation energy. For Ni-like Mo, the optimum temperature should lie at 155 eV.

The density is optimized through a balance between the mechanisms populating the upper and lower states; at high density, the upper state fractional population saturates, while the lower state population continues to increase. For Ni-like Mo, the optimum density is found to be around  $1-2 \times 10^{19} \text{ cm}^{-3}$ .

Under these various optimal conditions, and under the assumption of a Ni-like fractional population of 20%, the laser gain coefficient is predicted to be around  $10 \text{ cm}^{-1}$ ; also, in this region, it should be linear in the pump intensity. Experimentally, a coefficient of  $5 \text{ cm}^{-1}$  was inferred (Chapter 8) at intensities 2-3 times higher than should be required to generate 155 eV. The gain, while present, was thus considerably lower than predicted; more sophisticated analyses of the gain, the dump-transition opacity, and the plasma physics should probably be performed to achieve better agreement between theory and experiment.

### 6.3 Overview of relevant plasma physics

According to the analysis in the preceding section, a Ni-like x-ray laser near  $Z = 42$  requires a plasma of density  $1-2 \times 10^{19} \text{ cm}^{-3}$  and electron temperature 150-200 eV in order to generate high gain. In the following sections and Chapter 7, relatively simple arguments will be developed to show that these plasma conditions are attainable in our system. The following topics will be discussed in this chapter: basic plasma characteristics, the mechanisms by which the pump laser interacts with the plasma, the energy balance between absorbed

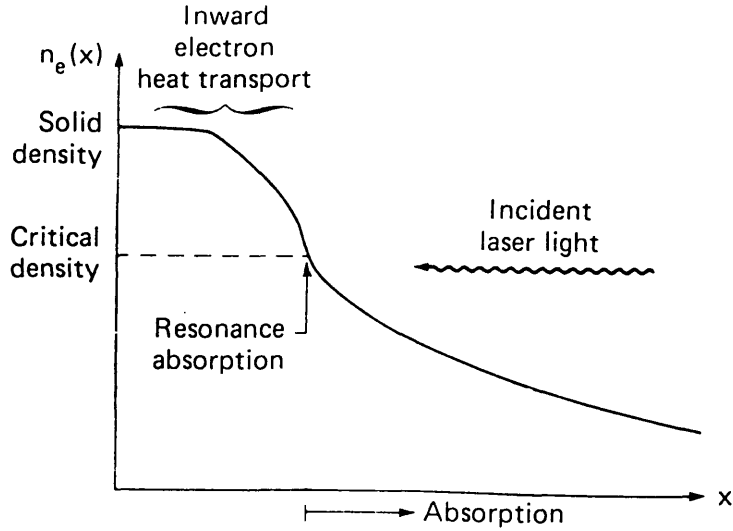


Figure 6.3: Coronal plasma during laser illumination (from [26])

pump light and plasma generation, the choice of target configuration, and finally the ionization and recombination rates which will determine whether the plasma in fact has a large population in the Ni-like charge state, as required. All these topics except the last two are discussed to some extent by Max [26] and Kruer [30]; an article by Fabbro, Max and Fabre [31] gives a very in-depth discussion of heat flow in laser plasmas.

In our approach, the required conditions for gain are found in the coronal plasma ablated from an initially solid target by a train of high intensity laser pulses, as shown in Figure 6.3. Laser light is absorbed in the corona, and its energy is conducted inward toward the cold, high density solid surface where new material is ablated. The desired plasma density is low relative to that of the solid and that where the laser light is absorbed; plasma of that density is found further out at distances of typically tens to hundreds of microns above the surface.

For plasmas in our range of interest, the Debye length  $\lambda_D \equiv (T_e/4\pi n_e e^2)^{1/2}$ , representing the distance down to which neutrality is preserved, is on the order of nanometers. The number of electrons within a Debye sphere,  $N_D \equiv$



$(4\pi/3)n_e\lambda_D^3$ , is large, so that the microscopic scale behavior of the plasma (distance scales of  $\lambda_D$ , frequency scales of the plasma frequency  $\omega_p \equiv (4\pi n_e e^2/m_e)^{1/2} \sim 10^{15}$  Hz) averages out when we consider the macroscopic behavior; we can assume charge neutrality, ignore plasma oscillations, and apply the equations of kinetic theory and hydrodynamics.

The thermal energy of the plasma can be characterized by an electron temperature  $T_e$  and an ion temperature  $T_i$ ; the equilibration rates are, adapted from Spitzer [32],

$$\tau_{ee}, \tau_{ii} = \frac{14 \times 10^6 A^{1/2} T^{3/2}}{n Z^4 \ln \Lambda} < 1 \text{ psec}$$

$$\tau_{ei} = \frac{7 \times 10^6 A_e A_i}{n Z_e^2 Z_i^2 \ln \Lambda} \left( \frac{T_e}{A_e} + \frac{T_i}{A_i} \right)^{3/2} > 100 \text{ psec},$$

where  $A$  represents mass in units of  $m_p$  and is  $1/1836$  for an electron and  $96$  for a Mo ion;  $\ln \Lambda \sim 3$  is the Coulomb logarithm; and  $Z$  is the electronic or ionic charge. On the scales of time, temperature, and density of interest, both  $T_e$  and  $T_i$  will be well established but are unlikely to be equal. The electrons are heated by the laser energy; the ions are not heated directly, but only through the electrons, while they are strongly cooled by  $P dV$  work during the plasma expansion. Therefore, typically  $T_e \gg T_i$ .

There are  $Z_c$  electrons per ion (where  $Z_c$ , the ionic charge state, equals  $14$  for Ni-like Mo), and the electron thermal speed is much higher than that of the ions, even at equal temperatures. As a result of these facts, the plasma thermal energy, thermal transport and pressure are all determined by the electron temperature (as too are ionic collisional excitation and ionization rates). The ion temperature does not play a significant role in our calculations other than in determining the x-ray laser Doppler width.

Electron thermal transport is a particularly important process in laser-plasma interactions. A high conductivity means that the laser energy is rapidly

conducted inward to cold, dense regions, which is desirable for laser fusion experiments but not for coronal x-ray lasers. Conversely, a low conductivity means higher coronal temperatures, which will benefit us.

The heat flux is customarily taken to be the minimum of the classical value given by Spitzer [32] and the flux-limited form [31]:

$$q = \min \begin{cases} -K_0 T_e^{5/2} \nabla T_e \\ -f n_e m_e^{-1/2} T_e^{3/2} \end{cases}$$

where  $K_0$  is defined in Spitzer, and the flux limiter  $f$  is typically taken to be in the range 0.03-0.1. Note that the flux-limited form does not depend on the thermal gradient. Its physical meaning is that the electrons can transport their thermal energy  $\sim n_e T_e$  at a rate proportional to their thermal speed  $\sim (T_e/m_e)^{1/2}$ . During illumination of a target by a high intensity laser, the temperatures and gradients are typically high enough that the flux limited form is applicable.

## 6.4 Pump light absorption

When a high intensity laser beam illuminates a surface, it rapidly begins to generate a plasma [26]. The plasma electrons modify the propagation of the laser through the index of refraction,

$$n = 1 - \frac{\omega_p^2}{\omega^2},$$

where  $\omega_p^2 = 4\pi n_e e^2/m_e$ . As the laser propagates through progressively denser plasma, its  $\vec{k}$  vector becomes smaller, until, at the critical density, given by  $n_c \equiv \omega^2 m_e / 4\pi e^2$ , the beam is reflected. For  $\lambda = 1.05 \mu\text{m}$ , the critical surface occurs at an electron density of  $10^{21} \text{ cm}^{-3}$ . The higher-density region closer to the target, where the laser cannot propagate, is termed “overdense”, while

the region outside the critical surface is “underdense”. Since the pump light absorption is strongly density dependent, most of it will occur in the portion of the underdense region nearest the critical surface.

The most important absorption mechanism in our experiments appears to be inverse Bremsstrahlung (also known as collisional or classical absorption), which occurs through electron-ion collisions [26]. The propagating laser beam induces oscillations in the electrons; collisions with ions dephase the oscillations, damping the light wave and causing energy to be transferred to the electrons. Since the process involves binary collisions, it varies as the square of the density; and since disruption of the oscillations is less noticeable at high  $T_e$ , the process favors low temperatures. This picture of inverse Bremsstrahlung is accurate in the parameter range of interest; at higher laser intensities, the absorption is decreased by nonlinear effects involving the modification of the collisional frequency by the coherence of the electron oscillatory motion and the presence of a non-Maxwellian electron velocity distribution.

The absorption coefficient can be expressed as

$$K = (2\pi)^{1/2} \left( \frac{16\pi}{3} \right) \frac{Z_c n_e^2 e^6 \ln \Lambda}{\omega^2 c (m_e T_e)^{3/2} (1 - n_e/n_c)^{1/2}},$$

which can be averaged and evaluated to give, for an exponential density profile with a beam propagating to the critical surface and reflecting,

$$\bar{K} = 2.4 \times 10^{-16} n_c Z_c \ln \Lambda T_e^{-3/2} = 3600 \text{ cm}^{-1} \quad (6.8)$$

for  $n_c = 10^{21} \text{ cm}^{-3}$ ,  $Z = 14$ ,  $\ln \Lambda = 3$ , and  $T_e = 200 \text{ eV}$ . The total absorption is given by  $1 - e^{-\bar{K}L}$ , where  $L$  is the scale length, so we see that very large absorption is possible with scale lengths of a few microns.

On the first laser pulse of the train of pulses, scale lengths are short and the inverse Bremsstrahlung is probably relatively weak. On subsequent pulses, the plasma has expanded to scale lengths of several microns, and very high

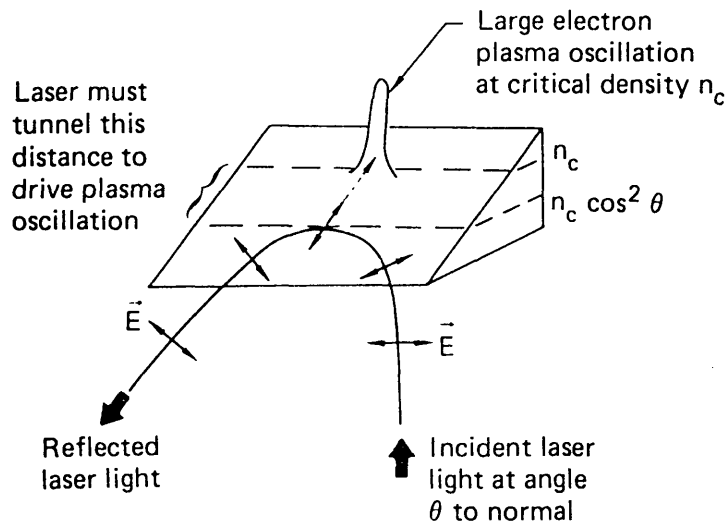


Figure 6.4: Resonance absorption (from [26])

absorption might be expected. Unfortunately, it turns out that the density profile at the critical surface will tend to steepen dramatically during the pulse [30]. This occurs through the ponderomotive force (photon and plasma pressure) and through inhibition of thermal transport (which can be shown on theoretical grounds to produce a discontinuity in density and temperature at critical) [31]. This effect has been observed in simulations of the plasma during the second pulse and seems to reduce the absorption to a value on the order of 20%. In spite of this effect, inverse Bremsstrahlung appears to be the dominant absorption mechanism during the second and subsequent pulses.

The first-pulse absorption has a large contribution from resonance absorption (Figure 6.4). A  $p$ -polarized beam incident on the target at a moderate angle does not penetrate all the way to the critical surface, but is bent by the refractive index gradient in a manner akin to a GRIN lens. The point of closest approach occurs at a density of  $n_c \cos^2 \theta$ ; at this point, the laser electric field points into the density gradient and drives plasma density oscillations (Langmuir waves). At the critical surface, these oscillations would be resonant because their frequency  $\omega$  would equal  $\omega_p$ ; this would give rise to a large

transfer of energy from light wave to plasma. Since the lightwave does not, in fact, reach the critical surface, the wave must tunnel from density  $n_c \cos^2 \theta$  to  $n_c$ ; this favors near-normal angles of incidence. However, the component of  $\vec{E}$  pointing into the density gradient and driving the Langmuir wave is maximized at shallow angles and vanishes at normal. An optimal angle of incidence can be found, and in theory, absorption on the order of 50% can be achieved there under ideal conditions.

The averaged inverse Bremsstrahlung coefficient, however, varies as  $\cos^3 \theta$  [30] and optimizes at normal; thus, attempts to increase the total absorption by tilting the input beam and boosting resonance absorption should take this tradeoff into account. Our experiments to date have been done using a  $12^\circ$  angle of incidence, based on an optimization performed by K. Estabrook at LLNL. As will be discussed in Chapter 8, polarization experiments showed comparable contributions of both types of absorption on the first pulse, and greatly increased inverse Bremsstrahlung on the second.

## 6.5 Electron temperature during pump pulse

In this section, we examine the steady state electron temperature, demonstrate the plausibility of the phenomenological flux limiter, and determine the characteristic thermal response time of the plasma during the laser pulse.

The electron temperature is established at the critical surface in a balance between absorbed laser power and flux-limited conduction [26]. In the steady state, an estimate of the temperature can be found from

$$I_{\text{abs}} - f n_c m_e^{-1/2} T_e^{3/2} = 0, \quad (6.9)$$

(which yields equation (6.3)). For  $f = 0.1$ , an absorbed intensity of  $2 \times 10^{12}$  W/cm<sup>2</sup> is needed to generate a temperature of 200 eV; this is likely

to correspond to around  $10^{13}$  W/cm<sup>2</sup> incident. Unfortunately, the values of both the flux limiter  $f$  and the absorption efficiency in the presence of profile steepening are poorly known, so that this calculation gives a crude estimate at best. Profile steepening can be modeled using conventional hydrodynamics codes, but the origins of flux inhibition are not yet fully understood, and a method for selecting an appropriate value for  $f$  is not well established.

Nonetheless, it can be demonstrated that the expression for flux limited flow is a reasonable estimate of the actual heat flow required in steady state to ablate material continuously and maintain an isothermal rarefaction wave (the expanding underdense plasma). We use the same argument as will be employed in Chapter 7. Most of the incident power goes into ablation and heating of new plasma. Ultimately this material arrives at the critical surface, where on theoretical grounds [31] it is known to be moving at the local sound speed  $c_s = ((Z_c/M_i)T_e)^{1/2}$ , and it has been heated to the local electron temperature  $T_e$ .

Expressions for the heat flux from the critical surface inward to heat and accelerate that mass, and outward to perform isothermal  $P dV$  work in the expanding plasma, can be written and balanced against the laser intensity:

$$I_{\text{abs}} - 2T_e \frac{dn_{\text{tot}}}{dt} - T_e \int_0^\infty n_e \frac{\partial v}{\partial r} dr = 0.$$

These expressions are derived in Chapter 7 and are given here in the form for a planar expansion:  $dn_{\text{tot}}/dt$  is the flowrate of new mass, and  $\partial v/\partial r$  is the gradient of the velocity profile in the underdense plasma, which determines the  $P dV$  rate. Using the self-similar solution as in Chapter 7 gives

$$I - 2n_c T_e c_s - n_c T_e c_s = I - 3n_c \left(\frac{Z_c}{M_i}\right)^{1/2} T^{3/2} = 0,$$

and it can be identified through comparison with (6.9) that

$$f = \frac{3}{(m_p/m_e)^{1/2}} \left(\frac{Z_c}{A}\right)^{1/2} = 0.07 \left(\frac{Z_c}{A}\right)^{1/2} = 0.03$$

for our plasma. This is actually a commonly used value of the flux limiter for intensities on the order of  $10^{14}$  W/cm<sup>2</sup> [26]. At our somewhat lower intensities and shorter pulse durations,  $f$  is reportedly taken to be somewhat larger ( $\sim 0.1$ ), so there is some extra heat flow compared to our simplistic picture. Several heat sinks have been ignored: ionizing the cold mass to the desired ionization stage requires an average energy of order  $T_e$  per electron (for Ni-like Mo, it comes out to 134 eV per electron and will raise  $f$  by 22% at  $T_e = 200$  eV); the shock wave driven into the solid requires a power input; and probably, in our timescale of interest, the ablation process does not reach steady state [31].

That the form of the heat flow expression here matches that of the flux limited expression is actually not surprising, since in both cases, mass with energy density  $(3/2)n_e T_e$  is being transported at a speed proportional to  $T_e^{1/2}$ . Basically, this value of the flux limiter represents the electron heat being transported at the ion acoustic velocity rather than the electron thermal velocity.

In this calculation, one-third of the total heat flux is found to be conducted outward to keep the expanding corona isothermal. This is in reasonable agreement with [31], who find a value of one-quarter in a non-flux-limited situation and show that with a flux limit, the outward-conducted fraction increases somewhat. Now, in the more realistic case where the flux limiter is higher than estimated here (e.g. 0.1 rather than 0.03), the total amount of outward flux should stay constant, and so in our case the fraction might be expected to drop from 1/3 to 1/10.

The flux-limited conduction problem will now be solved in the transient period before the plasma reaches its steady-state temperature. This will yield a temperature risetime  $t_r$  which should guide our choice of laser pulse duration. For a laser pulse of duration comparable to, or longer than,  $t_r$ , the temperature

is set by the pulse intensity, whereas for a shorter pulse, it depends on the time-integrated energy fluence. Thus, overly short, high-intensity pulses offer little benefit over pulses of equal energy with duration  $t_r$ . By the same token, pump pulses longer than  $t_r$  will use excessive total energy for a given temperature. It is this observation which is driving present experimental efforts in our group toward shortening the pump pulses from 60 psec to around 10-15 psec, which should be closer to the value of  $t_r$ .

The transient form of the heat equation reads

$$I_{\text{abs}} - f n_c m_e^{-1/2} T_e^{3/2} = \frac{3}{2} n_c L \frac{dT_e}{dt}$$

where the right hand side now represents the time rate of change of thermal energy in the underdense region, and  $L$  is an effective scale length characterizing the amount of underdense plasma (the density profile need not be exponential; we are interested only in the total amount of mass to be heated, and  $L$  is the scale length that that amount of mass would have if it were exponential, in a planar geometry).

This equation cannot be solved explicitly for  $T_e(t)$ , although a cumbersome implicit form can be found. Instead we have cast the equation in normalized variables and solved numerically: taking

$$\begin{aligned} T_{e,f} &\equiv \left( \frac{I_{\text{abs}} m_e^{1/2}}{f n_c} \right)^{2/3} \\ T &\equiv T_e / T_{e,f} \\ \tau &\equiv \frac{2}{3 m_e^{1/2}} \frac{f}{L} T_{e,f}^{1/2} t, \end{aligned}$$

it follows that

$$\frac{dT}{d\tau} = 1 - T^{3/2}$$

which is plotted in Figure 6.5 together with the exponential form  $1 - e^{-\tau}$  (which solves  $dT/d\tau = 1 - T$ ). A characteristic risetime (to 0.71) is  $\tau_r = 1$ ,



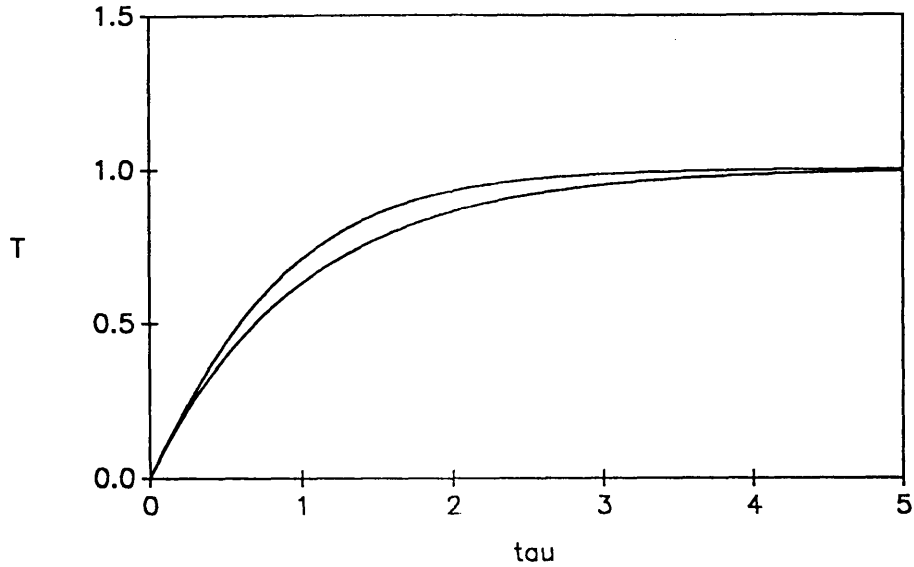


Figure 6.5: Normalized transient temperature response (lower curve is exponential)

which corresponds to

$$t_r = 3.6 \times 10^{-8} \frac{L}{f} T_{e,f}^{-1/2} \quad (6.10)$$

for  $L$  in cm and  $T_{e,f}$  in eV.

On the first pulse of our experiments, the value of  $L$  will be very small ( $\sim 1 \mu\text{m}$ ) throughout the pulse, as very little plasma has been formed; the temperature is expected to follow the steady-state equation (6.3) closely. On the second pulse, though, the plasma is much larger. Using results from our model in Chapter 7 for 15 psec and 60 psec pulses at 200 eV, we find effective scale lengths of  $5 \mu\text{m}$  and  $13 \mu\text{m}$ , respectively. Equation (6.10) with  $f = 0.1$  then gives  $t_r = 13$  psec and 33 psec.

For the 60 psec pulse, the risetime seems comfortably matched to the pulse duration. For the 15 psec pulse, it seems marginal, especially when the uncertainty in  $f$  is considered. If experimentally it should be inferred that the temperature is not rising as high as it should on the second pulse, it might be necessary to reduce the first-pulse energy or the inter-pulse delay to decrease

the amount of mass needing to be heated.

It can be seen from this calculation that the transition from  $t_p > t_r$  to  $t_p < t_r$  is relatively gentle, since the plasma size drops somewhat with the duration of the first pulse. On the other hand, it is also fairly clear that compression of pulses to much less than  $\sim 10$  psec is unlikely to have much benefit, for plasmas of reasonable spatial extent.

## 6.6 Target configuration

Our choice of target configuration and our decision to pump with multiple pulses can now be explained. Two well-known options for targets are a solid surface and a thin foil which burns through during the laser pulse. In both cases, the pump radiation is focused to a thin line on the target, at near normal incidence.

Foils have been used in the successful experiments at LLNL [33]. According to theory, after the foil burns through, it takes on an expanding Gaussian density profile with a broad, relatively flat top with a width of on the order of a hundred microns. This is beneficial because those x-ray laser schemes optimize at densities of over  $10^{20}$   $\text{cm}^{-3}$ ; critical density for the x-ray laser radiation is around  $2 \times 10^{24}$   $\text{cm}^{-3}$ , so having a density gradient on the order of  $10^{20}$   $\text{cm}^{-3}/10$   $\mu\text{m}$  or greater will cause the x-ray laser beam to be badly refracted in distances of millimeters. The broad top of the Gaussian has gentle density gradients, alleviating this problem. Because the optimal lasing density is not far below the pump critical density, the plasma need not expand much after burn-through before reaching the desired lasing density at the middle of the Gaussian. Therefore the plasma will not be dramatically cooled by  $PdV$  work, and some inverse Bremsstrahlung absorption will continue during the expansion; the plasma can be maintained at the required high lasing

temperature through the time when the lasing density is reached.

Foil targets are less well suited to our laser scheme. At  $10^{19} \text{ cm}^{-3}$  density, our system is much less sensitive to density gradients and the main benefit of the foil becomes unnecessary. Moreover, an expansion of around  $100\times$  would be necessary after the foil burns through, to achieve the required density. The temperature will have dropped, by adiabatic cooling, by a factor of 20. Because the plasma is now so low in density, it cannot absorb pump radiation efficiently to bring the temperature back up (inverse Bremsstrahlung will go as  $n_e^2 L \sim n_e$ , so the absorption will have dropped by  $100\times$  relative to its value at burn-through).

A solid target fits our needs well. Both the fact that at  $10^{19} \text{ cm}^{-3}$ , the scheme is less sensitive to density gradients, and the fact that the region of plasma at that density is far removed from the critical surface, where gradients tend to be high, mean that x-ray beam refraction will not be a serious concern to us. In Chapter 7, Figure 7.13 shows that for a solid target, the gradient at  $10^{19} \text{ cm}^{-3}$  is  $\sim 10^{19} \text{ cm}^{-3}/100 \mu\text{m}$ , which means that propagation over multiple centimeters of gain medium should be possible. Also, a solid target is very practical and convenient to use, since many shots can be taken on it if it is stepped slightly between shots to keep exposing fresh material.

The plasma should be fairly large (order of  $100 \mu\text{m}$ ) so that the gain region and the inverse Bremsstrahlung absorption are large (to achieve as high a temperature as possible with a given intensity). Were a single pulse to be used, it can be shown that the pulse duration would need to be around a nanosecond to give a plasma of the desired size. Much of the pulse energy would be wasted by not being absorbed or by being conducted into the cold overdense region. Since, as was shown in the previous section, it takes only tens of picoseconds for the underdense corona to reach its steady state temperature under laser

illumination, we can reach the lasing temperature much more efficiently by heating a pre-formed, cold plasma with a pulse of  $\sim 10$ -100 psec duration at the appropriate intensity. In our scheme, originally proposed in 1988 [25] a train of pulses from a mode-locked laser is used, with an inter-pulse spacing of 7.5 nsec.

The first pulse generates the initial plasma, which blows outward and cools (this process is modeled in Chapter 7). The second pulse re-heats the expanded plasma efficiently since its scale length is now large; the resulting high temperature at the critical surface is rapidly transmitted out to the gain region at  $10^{19} \text{ cm}^{-3}$  by electron thermal conduction. Clearly, a benefit of the solid target is that it always has a critical surface where pump radiation can be efficiently absorbed to re-heat the gain region. Also, it can be pumped by third and subsequent pulses to give repeated x-ray laser pulses or—in the presence of a cavity—a synchronously-pumped x-ray oscillator.

Multiple-pulse pumping saves a factor of around 10 in pump energy compared to a single nanosecond pump pulse, since the intensities would need to be comparable. It also produces very low ion temperatures, since the ions are weakly coupled to the hot electrons but experience a large amount of  $P dV$  cooling between pulses. This decreases the Doppler linewidth and so increases the gain (also, unfortunately, the susceptibility to trapping (section 6.1)).

Nonetheless, the overall efficiency remains low because energy is expended heating a large region of plasma, of which only a small, low-density region is useful for gain. A pump laser in the  $5 \mu\text{m}$  range might be preferable since it would be absorbed at  $4 \times 10^{19} \text{ cm}^{-3}$  [34], as might a shallow-incidence target angle using the present laser, penetrating to  $n' = n_c \cos^2 \theta$  [35]. Both schemes would benefit from having lower flux-limited conduction from the absorption region into the cold overdense region (equation (6.3)), but would

suffer from decreased inverse Bremsstrahlung absorption efficiency (equation (6.8)). For the first scheme, both effects will scale as  $n_e$  for equal  $T_e$  and identical, unsteepened density profiles. For the second scheme, the conduction goes as  $n'$  and the absorption as  $n'^{3/2}$ ; but in this scheme, the pump radiation is to be refocused and re-used until it has been efficiently absorbed. Both of these options will be interesting to pursue if the absorption and refocusing issues can be addressed.

## 6.7 Ionization balance

In this section, the degree of ionization of the plasma is studied as a function of temperature and density in order to determine the Ni-like population on the second pump pulse, when gain is expected. In the expected gain region, the fractional abundance of Ni-like ions is expected to be high in steady state at temperatures of 100-200 eV. However, the equilibration times are comparable to the temperature lifetime, and it follows that the transient behavior of the plasma must be investigated further.

Figure 6.6 shows the ionization potentials of the Mo ion; the step due to the Ni-like closed shell is prominent. Nonetheless, in spectroscopy of laser-produced Ni-like plasmas, typically five or more states are seen to be present in significant quantities [36].

In steady-state LTE plasmas, the ionization balance is found recursively using the Saha equation, which gives the population ratio between adjacent charge states [17]:

$$\frac{n^z}{n^{z-1}} = \frac{2}{n_e} \frac{Z^z(T_e)}{Z^{z-1}(T_e)} \left( \frac{m_e T_e}{2\pi\hbar^2} \right)^{3/2} e^{-I_P^{z-1}/T_e}.$$

This equation is an analog of the mass-action law of physical chemistry.

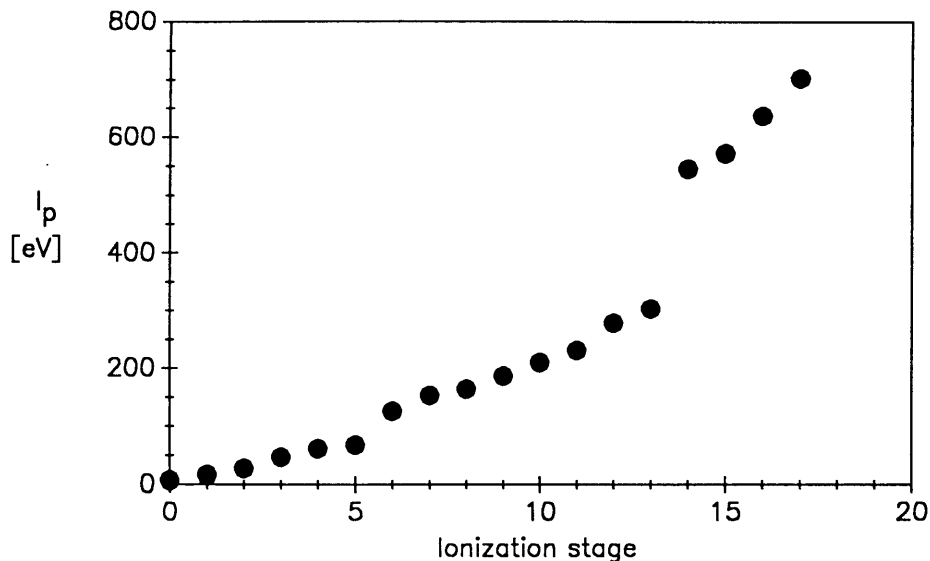


Figure 6.6: Ionization potentials of the Mo ion (from [28])

In lower-density, non-LTE plasmas, the explicit temperature-dependent rate coefficients must be used:

$$\frac{n^z}{n^{z-1}} = \frac{\overline{\sigma v}_{\text{ci}} + \overline{\sigma v}_{\text{auto}}}{n_e r_{3\text{br}} + \overline{\sigma v}_{\text{dr}} + \overline{\sigma v}_{\text{rr}}},$$

where the subscripts ci and 3br denote collisional ionization and its detailed-balance inverse, three-body recombination; and auto, dr, and rr denote autoionization, dielectronic recombination, and radiative recombination, respectively. It is believed that all the possibly significant processes are represented here. Since the three-body rate coefficient is proportional to the electron density  $n_e$ , it becomes negligible at low densities (the regime where this is true is called the coronal regime and is typically below  $n_e = 10^{16} \text{ cm}^{-3}$ ).

Solving the full coupled set of these equations would require knowledge of a large number of rate coefficients. Since our interest is restricted to the Ni-like population, we can gain some insight by finding only the ratio

$$\frac{n^{\text{Ni}}}{n^{\text{Cu}}},$$

where the Cu-like is the adjacent alkali-like state. When the ratio is unity, those two states presumably lie at the maximum of the ionization distribution function. At somewhat higher ( $\sim 50$  eV) temperatures, the Ni-like state should lie centered at the maximum and should contain a large fraction ( $\sim 30\%$ ) of the population.

A general description of the relevant rate coefficients is found in Chapter 5 of Sobelman [18]. In the present analysis, the coefficients were evaluated as follows. Approximate values of the cross section for direct collisional ionization from the  $4s$  sublevel of the Cu-like ion were found using the Coulomb-Born-exchange calculations of Golden and Sampson [37]. These were then integrated over a Maxwell-Boltzmann electron distribution to give the rate coefficients  $\overline{\sigma v}_{ci}$ .

Autoionization occurs following 3–4 collisional excitation to a doubly excited state in the Cu-like species. The rate through this channel was estimated using the calculated  $3d$ – $4d$  excitation rates for the Ni-like species [29] and assuming a fractional yield of 0.7. The rate was found to be about 10 times higher than the direct collisional ionization rate over the range from 70 eV to 200 eV.

Direct radiative recombination was found to be insignificant under the conditions of interest; three-body recombination was evaluated using the analytic formulation given by Pert [38]. This process preferentially populates the Cu-like Rydberg states, and a cascade to the ground state follows, which for our system is radiative at high temperatures and collisional at low temperatures.

Dielectronic recombination (inverse Auger ionization) was studied using the formulation of Hagelstein [39], summing the rates into  $n = 4$  final states through  $\overline{3d}4,4$  intermediate states; rates involving other states will be relatively insignificant unless the temperature is high. This process was found to be the

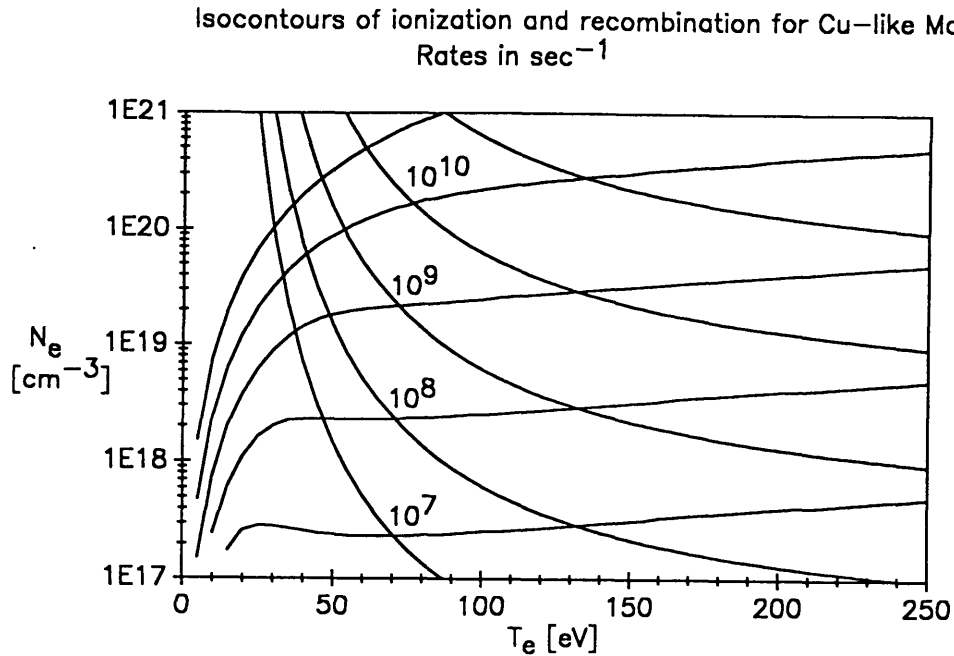


Figure 6.7: Isocontours of ionization and recombination between Cu-like and Ni-like Mo (rates in  $\text{sec}^{-1}$ )

dominant means of recombination over much of the region of interest.

Using these calculations, we have generated isocontours of ionization and recombination (Figure 6.7). It can be seen that the Cu-like and Ni-like states are in equilibrium in the neighborhood of 80 eV. Since collisional excitation (leading to autoionization) and dielectronic recombination are both proportional to  $n_e$ , the equilibrium is practically independent of density. The Ni-like population should therefore reach its steady-state maximum at a temperature somewhat above 100 eV; exactly where that maximum lies will depend on the relative rates between the Ni-like and the neighboring Co-like state.

Earlier steady-state simulations [25] had shown that the Ni-like population optimizes at temperatures below 100 eV. At that time, the conclusion was drawn that since the  $3d-4d$  excitation rate would be small at those temperatures, no gain would be generated in the steady state at high Ni-like populations. Conversely, if the steady-state temperature were high enough to drive the excitation, the plasma would be overionized and the Ni-like population



negligible.

This problem was addressed at that time by considering that the ionization times at the densities of interest are on the order of 100 psec. Therefore, at 150 eV and  $10^{19} \text{ cm}^{-3}$ , the plasma ionization state on the second pump pulse will pass through the Ni-like state relatively slowly on its way to the (overionized) steady state, and a large Ni-like population should be present transiently on a subnanosecond timescale.

This picture is consistent with the present calculations. We note further that whereas the Cu-like ionization time from the present calculation is found to be about 100 psec, the Ni-like ionization time will be much slower. This owes both to the lack of the autoionizing channel in the Ni-like and to the much higher Ni-like ionization energy, which will retard the ionization rate from the  $3d$  ground state. Therefore a large population will bottleneck in the Ni-like state for times of around 1 nsec.

Both current theory and experiment suggest that the steady state is never reached at low density and that only the transient dynamics are relevant. The high-temperature lifetime is predicted by the hydrodynamics model in Chapter 7 (Figure 7.15) to be around 0.5 nsec; experiments have shown lifetimes around 1 nsec. It is unlikely, given the above considerations, that the Co-like and higher ionization states will be highly populated during this time. Instead, the issue arises whether the Ni-like state is in fact reached while the temperature is still high enough to drive the  $3d-4d$  excitation. The estimated 100 psec Cu-like ionization time suggests that the Ni-like population should grow large while the temperature is still high.

More accurate modeling of the temperature and ionization balance is needed to investigate these points. The Ni-like/Co-like ionization balance should be investigated in the same manner as was the Cu-like/Ni-like. The autoioniza-

tion and dielectronic recombination analyses should be performed more rigorously. Also, increased understanding of the ionization state in the cold plasma before the second pulse will be helpful in calculating the delay before the Ni-like population is maximized. A time-dependent ionization balance model could be coupled with the hydrodynamics model of Chapter 7 to give a realistic picture of the development of the gain conditions. The entire ionization balance issue will be greatly clarified when time-resolved observations of the Ni-like principal resonance line can be made as a function of density (height above target surface).

# Chapter 7

## One-dimensional hydrodynamics model

### 7.1 Background and assumptions

In this chapter, results from a model of the post-pulse plasma cooling are discussed. A computer implementation of the model shows that during the cooling after the first laser pulse, the density and velocity profiles take on virtually stationary forms. Simple analytic expressions for the profiles and a power law for the cooling rate may then be derived for all time as functions of a single parameter. The model is, to our knowledge, the first analytic formulation of the plasma behavior during the expansion/cooling phase. It is similar in spirit to the self-similar expansion solutions and should be very useful in studies of both multiple-pulse laser-plasma interactions and recombination lasers.

The specific function of this model is, starting with an analytic solution for the plasma profiles immediately following the first pump pulse, to model the supersonic expansion and cooling of the plasma from that time until the

next pulse arrives. The code tracks the coronal plasma temperature, density profile, velocity profile, and cooling rates. In our code we have made several simplifying assumptions which make the problem tractable using a microcomputer. Although the simplification comes at some cost in analytical rigor, the dominant effects are treated in a reasonable manner and the results should give at least a rough approximation the plasma behavior.

A more sophisticated model would solve the 2-dimensional expansion shown on the left in Figure 7.1, where the line focus axis is into the page. The initial plasma width  $w_0$  is determined by the line focus width and plasma transverse thermal conduction, and is estimated at about  $40 \mu\text{m}$ . Near the solid surface, and the critical surface a few microns above it, the expansion is planar; as dimensions grow larger than  $w_0$ , the expansion becomes cylindrical. The temperature and heat transport everywhere must be tracked, particularly near the critical surface, where the laser energy is deposited: inside that surface, at rapidly increasing density, the temperature drops quickly; and the coronal plasma experiences significant cooling by thermal conduction into this region. This heat flow causes a mass flow from the overdense region into the corona which must be monitored.

Our interest is only in the underdense plasma, so we restrict our model to that region and make assumptions about what occurs at the critical surface, which forms our inner boundary. We shall see that the results are largely independent of the particulars of the boundary behavior. For our purposes, we assume a one-dimensional, half-cylindrical expansion from a half-cylindrical critical surface of radius  $r_0 = w_0/2$ , as shown on the right in Figure 7.1. Even in this cylindrical approximation, the expansion appears roughly planar in the immediate vicinity of the boundary. A further approximation is that the critical surface remains fixed at  $r_0$ ; in reality it moves outward somewhat as

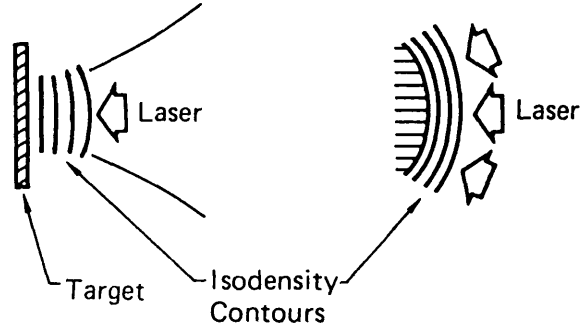


Figure 7.1: 2-D expansion and 1-D cylindrical approximation (from [26])

the plasma expands.

The plasma is modeled as having everywhere a uniform electron temperature  $T_e$  (which drops as the plasma expands and cools). This approximation is motivated by the observations that while the temperature is reasonably high, the electron thermal conduction, varying as  $T_e^{3/2}$  (flux limited) or  $T_e^{5/2}\nabla T$ , is very high; and when the temperature becomes low, the cooling is predominantly by  $P dV$  work, which is distributed fairly evenly throughout the plasma (this might be improved by making the cooling locally adiabatic once the temperature drops below a certain point).

The plasma is taken to be thermally isolated, except that at the critical surface, new cold mass is injected at the local sound speed. Accelerating this mass and bringing it to ambient plasma temperature cools the plasma: we call this effect “mass cooling,” and we postulate that this cooling is essentially equivalent to that represented by flux limited electron thermal conduction into the overdense region. The flux limited cooling rate and mass cooling rate have the same temperature dependence ( $T_e^{3/2}$ ), and the calculated rates are comparable (cf. Chapter 6), so the overall behavior should be approximately

correct.

The presence of a Mach 1 flow at the critical surface in steady state during a laser pulse is well established, both through simulations and theoretical analyses [31]. The behavior during the cooling phase after the pulse is less well understood. We view the continuing ablation of the cold, dense mass by the hot underdense plasma as being analogous to the ablation by laser power deposited at the critical surface, so that the plasma dynamics should be similar. Certainly the model has qualitatively the appropriate behavior: as the plasma cools, the sound speed drops as  $T_e^{1/2}$ , and the cold-mass flowrate drops accordingly. Postulating a Mach 1 flow of cold material has the benefit of allowing a solution to the model to be found in a relatively simple form, because the boundary behavior is tied in directly with the natural hydrodynamic variables (specifically  $c_s$ ).

A final assumption is that the plasma ionization state remains fixed. Clearly, some recombination will occur as the plasma cools, but this should not affect our results strongly at the densities and times of interest.

## 7.2 Hydrodynamic equations

The model integrates the one-dimensional hydrodynamic equations for continuity and momentum in an ideal gas, given here in their general form ( $\alpha = 1$  planar,  $\alpha = 2$  cylindrical,  $\alpha = 3$  spherical) [40]:

$$\begin{aligned}\frac{\partial n}{\partial t} + \frac{1}{r^{\alpha-1}} \frac{\partial}{\partial r} (r^{\alpha-1} n v) &= 0 \\ \frac{\partial v}{\partial t} + v \frac{\partial v}{\partial r} + \frac{c_s^2}{n} \frac{\partial n}{\partial r} &= 0\end{aligned}$$

Here  $n$  is the ion number density,  $r$  the spatial coordinate,  $v$  the velocity, and  $c_s = ((Z_c/M_i)T_e)^{1/2}$  the isothermal sound speed, where  $Z_c$  is the ionic charge,  $M_i$  the ionic mass, and  $T_e$  the electron temperature.

Under the stated assumptions for our model, energy conservation can be expressed as

$$\frac{3}{2}n_{\text{tot}}\frac{dT_e}{dt} + T_e \int_{r_0}^{\infty} n \frac{\partial v}{\partial r} r dr + 2T_e \frac{dn_{\text{tot}}}{dt} = 0$$

where

$$n_{\text{tot}} = \int_{r_0}^{\infty} nr dr = n_{\text{tot},0} + \int_0^t \frac{dn_{\text{tot}}}{dt} dt'$$

$$\frac{dn_{\text{tot}}}{dt} = n(r_0) c_s(t) r_0$$

are, respectively, the total number of ions (per radian) and the rate at which new ions are added at the boundary  $r_0$ . The first term represents cooling by  $P dV$  expansion; the second represents mass cooling and includes contributions of  $(1/2)T_e dn_{\text{tot}}/dt$  for accelerating the mass to  $v = c_s$  and  $(3/2)T_e dn_{\text{tot}}/dt$  for heating it to the ambient temperature.

The initial condition for our problem is the plasma immediately following the first laser pulse. Under the approximations that during the pulse, the absorbed intensity is constant (hence the temperature  $T_{e,0}$  and sound speed  $c_{s,0}$  are constant) and the plasma expansion is small compared to  $r_0$  (i.e.  $c_{s,0}t_p \ll r_0$ , where  $t_p$  is the pulse duration), the plasma is described by the well-known planar isothermal self-similar solution [40]:

$$n(r, t=0) = n(r_0) e^{-\frac{r-r_0}{r_p}}$$

$$v(r, t=0) = c_{s,0} \left( 1 + \frac{r-r_0}{r_p} \right)$$

where  $r_p \equiv c_{s,0}t_p$  is the scale length of the plasma immediately after the pulse.

We define the following normalized variables:

$$N(R, \tau) \equiv \frac{n}{n(r_0)}$$

$$V(R, \tau) \equiv \frac{v}{c_s}$$

$$R \equiv \frac{r}{r_p}$$

$$d\tau \equiv \frac{c_s dt}{r_p} \quad (7.1)$$

$$\alpha \equiv -\frac{1}{c_s} \frac{dc_s}{d\tau}; \quad (7.2)$$

here  $\alpha$  represents a normalized cooling rate. The equations become

$$\frac{DN}{D\tau} + N \frac{\partial V}{\partial R} + \frac{NV}{R} = 0 \quad (7.3)$$

$$\frac{DV}{D\tau} + \frac{1}{N} \frac{\partial N}{\partial R} = V\alpha \quad (7.4)$$

$$\frac{1}{3} \int_{R_0}^{\infty} N \frac{\partial V}{\partial R} R dR + \frac{2}{3} R_0 = N_{\text{tot}} \alpha \quad (7.5)$$

where

$$\begin{aligned} R_0 &\equiv r_0/r_p \\ N_{\text{tot}} &\equiv \int_{R_0}^{\infty} NR dR = N_{\text{tot},0} + R_0\tau \\ \frac{D}{D\tau} &\equiv \frac{\partial}{\partial \tau} + V \frac{\partial}{\partial R}. \end{aligned}$$

The initial conditions become

$$N(\tau=0) = e^{-(R-R_0)}$$

$$V(\tau=0) = 1 + (R - R_0);$$

now it may be verified that  $N_{\text{tot},0} = R_0$  and  $\alpha(\tau=0) = 1$ . Other initial conditions may of course also be used: note that the present condition is useful only for cases where  $R_0$  is about 3 or larger, so that the planar self-similar solution applies. For smaller values of  $R_0$ , the cylindrical isothermal self-similar solution of Schmalz [40] could be applied.

With the equations expressed in this fully normalized fashion, it becomes clear that the entire behavior of the model is determined solely by  $R_0$ . Equations (7.3), (7.4), and (7.5) can now be integrated numerically with  $R_0$  as a parameter, to give a family of solutions for  $\alpha(\tau)$ ,  $N(R, \tau)$ , and  $V(R, \tau)$ .



The sound speed  $c_s(\tau)$  is found by integrating (7.2) to give

$$\frac{c_s(\tau)}{c_{s,0}} = e^{-\int_0^\tau \alpha(\tau') d\tau'}$$

and so the temperature is

$$\frac{T_e(\tau)}{T_{e,0}} = e^{-2\int_0^\tau \alpha(\tau') d\tau'}$$

Now, the conversion back to standard time can be found by integrating (7.1):

$$\frac{t}{t_p} = \frac{r_p}{t_p} \int_0^\tau \frac{d\tau'}{c_s(\tau')} = \int_0^\tau e^{\int_0^{\tau'} \alpha(\tau'') d\tau''} d\tau'$$

The above forms somewhat obscure the time dependence of  $c_s$  and  $T_e$ . We will observe that the time dependence of  $\alpha$  is gentle; if we take  $\alpha(\tau) \approx \alpha(0) = 1$ , we can demonstrate the approximate time behavior:

$$\begin{aligned} \frac{t}{t_p} &= e^\tau - 1 \\ \frac{c_s}{c_{s,0}} &= \left( \frac{t}{t_p} + 1 \right)^{-1} \end{aligned}$$

which then gives

$$\frac{dT_e}{dt} \sim T_e^{3/2}.$$

### 7.3 Simulation code

The presence of the convective derivative in the hydrodynamic equations suggests the use of a Lagrangian code to solve them. The code divides the particles into a number (initially, typically 50) of zones of fixed particle number. The zones are allowed to move, and new zones are introduced at the boundary to simulate the incoming cold mass. At each time step, the movement of the zone boundaries is found using the momentum equation (7.4), and the sound speed and temperature are found using the energy equation (7.5). Quantities are

updated in leapfrog fashion to ensure second-order accuracy. Von Neumann-Richtmeyer artificial viscosity is used to prevent numerical instabilities.

The results are shown in Figures 7.2 to 7.6. For various values of  $R_0$ , the value of  $\tau$  corresponding to a desired time can be found from Figure 7.2. The behavior of  $\alpha(\tau)$  and  $T_e(\tau)$  can then be observed in Figures 7.3 and 7.4. Our typical plasma (Ni-like Mo,  $T_e = 200$  eV,  $t_p = 60$  psec,  $r_0 = 20$   $\mu\text{m}$ , giving  $r_p = 3.3$   $\mu\text{m}$ ) has  $R_0 = 6$ ; the corresponding normalized density and velocity profiles for four different times are shown in Figures 7.5 and 7.6.

Several aspects of the results are very interesting. First, the variation of the cooling rate  $\alpha$  with time is not large even as  $t$  and  $T$  vary over several orders of magnitude. This means that  $T$  will decay predominantly according to  $dT/dt \sim T^{3/2}$ ; it owes to the fact that both the  $P dV$  cooling and the mass cooling implicitly go as  $T^{3/2}$ . Second, on the whole there is not much variation with  $R_0$ : somewhat higher cooling rates and higher  $P dV$  fractions are associated with smaller values of  $R_0$  because the expansion will be more cylindrical, whereas with large  $R_0$ , a limit corresponding to the planar case ( $R_0 \rightarrow \infty$ ) appears evident, particularly in the plot of  $\alpha(\tau)$ .

The density and velocity plots are quite striking. It can be seen that behind an outward-moving boundary, the plasma establishes itself in a virtually stationary density distribution. The boundary travels outward at a speed  $v(r, t) - c_s(t)$ ; this can be seen as an inward-propagating acoustic wave being swept outward by the supersonic flow. The plasma distribution outside the boundary is dependent on the details of the initial condition; that within the boundary is isolated acoustically from the initial condition, and its form is determined solely by the overall cooling rate. In the time scales in which we are interested (nsec), the profile is stationary out to several hundred microns distance and down several orders of magnitude in density. Therefore, the re-

gion of interest for gain, at  $\sim 10^{-2} \times$  critical density, will be predictable in location and can be seen to be quite broad in spatial extent.

That the normalized velocity profile is quite linear is not surprising (particles far out must have moved faster to get there, most particles having started at around the same time), but that it is fairly stationary is remarkable. Acceleration of the plasma, from the momentum equation (7.4), is small over most of the plasma, so particles move at fairly constant velocities. The absolute velocity gradient drops with time as slower particles move outward; the sound speed drops at exactly the right rate that the normalized velocity is relatively constant.

## 7.4 Analytic expressions for $N(R)$ and $V(R)$

The above observations allow the derivation of analytic approximations for the stationary portions of  $N(R)$  and  $V(R)$  as functions of the instantaneous cooling rate  $\alpha(\tau)$ . We set the time derivatives  $\partial N/\partial\tau = \partial V/\partial\tau = 0$  in the continuity and momentum equations (7.3) and (7.4):

$$\frac{\partial}{\partial R} RNV = 0 \quad (7.6)$$

$$V \frac{\partial V}{\partial R} + \frac{1}{N} \frac{\partial N}{\partial R} = V\alpha. \quad (7.7)$$

Equation (7.6), plus the observation that  $\partial/\partial\tau RNV = 0$  and use of the boundary values, gives us

$$N = \frac{R_0}{RV}; \quad (7.8)$$

substituting this in the equation (7.7) and solving gives us

$$\frac{\partial V}{\partial R} = \alpha \frac{1 + (1/RV\alpha)}{1 - (1/V^2)}. \quad (7.9)$$

We see here that the sonic flow at the boundary causes the slopes of  $V$  and  $N$  to diverge there, as is seen in the simulation results. Equation (7.9) is not

separable as it stands, but the contribution of the  $1/RV\alpha$  term is fairly minor and does not affect the behavior at either  $R = R_0$  or  $R \rightarrow \infty$ . To a good approximation, we neglect this term and solve to find

$$V = 1 + \frac{\alpha}{2} (R - R_0) \left[ 1 + \left( 1 + \frac{4}{\alpha(R - R_0)} \right)^{1/2} \right]; \quad (7.10)$$

asymptotically,  $\partial V/\partial R = \alpha$ . The function is plotted in Figure 7.7. It turns out that we must scale the value of  $\alpha(\tau)$  from Figure 7.3 by a factor of typically 1.2 before using it here, to get the best agreement between Figure 7.7 and Figure 7.5.

Now  $N$  is found from equation (7.8); it has explicit  $R_0$  dependence and is shown for four values of  $R_0$  in Figures 7.8-7.11. Asymptotically, it becomes  $R_0/\alpha R^2$ . With these analytic solutions, the model is essentially completely solved.

It might be asked whether over a long period of time a true stationary solution, described everywhere by equations (7.8) and (7.9), could develop. For such a solution, new particles would still be continuously added at the boundary, yet the density everywhere would be expected to be constant. This difficulty is circumvented by the observation that, since the stationary solution has  $N \sim 1/R^2$ , the total particle number  $N_{\text{tot}} = \int_{R_0}^{\infty} NR dR$  diverges, and particles can continually flow outward without disturbing the density profile anywhere. Inserting the stationary solutions in the energy equation (7.5) with  $N_{\text{tot}} \rightarrow \infty$  causes the asymptotic portion of the  $P dV$  cooling to dominate the non-asymptotic portion and the mass cooling: we get

$$\frac{1}{3} \left( \frac{\partial V}{\partial R} \right)_{\text{asymp}} \stackrel{?}{=} \alpha.$$

We know that asymptotically  $\partial V/\partial R = \alpha$ , so we see that the “stationary” solution has an intrinsic  $P dV$  cooling rate which is three times too small to supply the cooling required for the solution to be self-consistent.

That our observed solutions are nearly stationary happens by virtue of several mechanisms which, together, provide the required cooling rate: the plasma is of finite extent, so that both mass cooling and non-asymptotic  $P dV$  cooling contribute; the cooling rate  $\alpha$  drops with time, in response to the plasma's tendency toward providing less than the required cooling rate; the asymptotic value of  $\partial V/\partial R$ , as mentioned above, tends to be greater than  $\alpha(\tau)$  by a factor of about 1.2; and the slightly nonzero values of  $\partial N/\partial \tau$  and  $\partial V/\partial \tau$  allow  $N$  to depart somewhat from the form (8).

## 7.5 Results and discussion

For our purposes it is useful to plot  $N$  in customary units at the time of the second pulse (7.5 nsec) for short (15 psec) and standard (60 psec) pulses at 200 and 400 eV (Figure 7.13). The region of density  $10^{19} \text{ cm}^{-3}$  is seen to be located about 100  $\mu\text{m}$  from the surface. The variation of the position with input pulse duration and initial temperature is not strong.

The model can also be used to analyze the temperature behavior following a second pulse. For the same set of pulses as above, we show the temperature behavior after the first pulse (Figure 7.14) and the second pulse (Figure 7.15). We see that the cooling rates are much slower after the second pulse, when the plasma is large and slow-moving, so that it cannot expand and cool rapidly. This extended high-temperature lifetime of typically 500 psec should allow the x-ray laser gain, if present, to be quite long-lived. Additionally, as mentioned in Chapter 6, the absorption efficiency and hence electron temperature should be increased significantly on the second and subsequent pulses because of the presence of the pre-expanded plasma. For collisionally pumped x-ray lasers, this model demonstrates several benefits of pumping using multiple pulses. Also, if we match the results of this model with the observed temporal behavior

of line emissions, we should be able to infer electron temperatures in our experiments.

It was stated at the beginning of the chapter that the simplistic handling of the boundary conditions would not have a severe impact on the results. Our results bear this out: the important quantities are the initial temperature and pulse duration, whereas the critical surface position  $R_0$  does not affect the results strongly. This is logical because the behavior turns out to be dominated by  $P dV$  cooling (see Figure 7.11, the fraction of total cooling that is due to  $P dV$ ) rather than mass cooling, which has a strong  $R_0$  dependence. The weakest point of the model is the claim that the flow at the critical surface remains Mach 1 at low temperatures (e.g. less than 5 eV). This overestimates the heat flow and contributes to two unphysical effects: the persistence of  $\partial N/\partial R = \infty$  at the critical surface after long times (i.e., after the critical surface has lost its significance and the density gradient should be relatively smooth there), and the presence of very low temperatures after several nanoseconds ( $\sim$  room temperature). The first effect does not make much difference because subsequent pulses will immediately steepen the profile again, and the picture given by this model will in fact be reasonable. The second also does not affect our overall results significantly.

The model is applicable not only to multiple-pulse-pumped lasers such as ours but also to the study of recombination x-ray lasers [1]. These lasers rely on the very fast cooling after a single pump pulse to cause recombination processes that preferentially populate excited states, leading to inversions. Cooling rates from this model should be helpful in predicting gains for these systems as a function of pumping conditions.

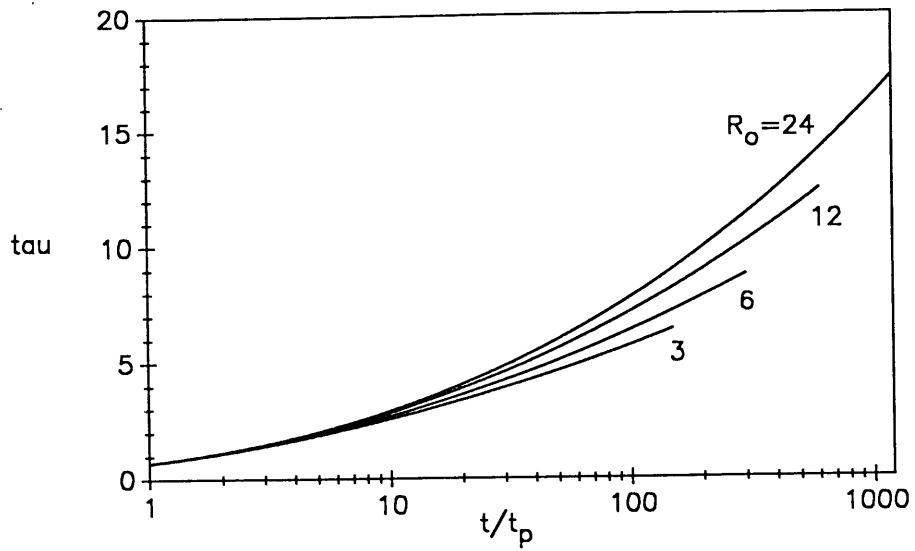


Figure 7.2

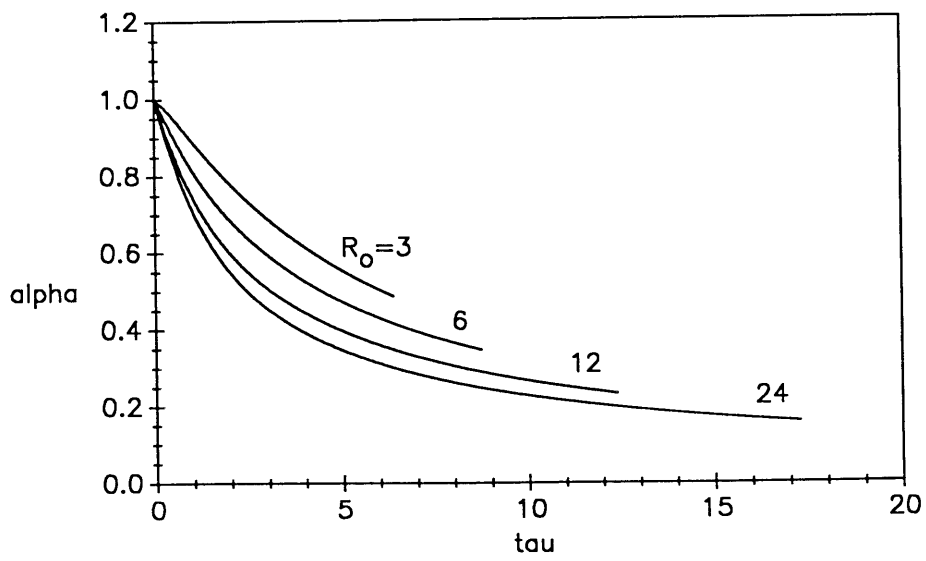


Figure 7.3

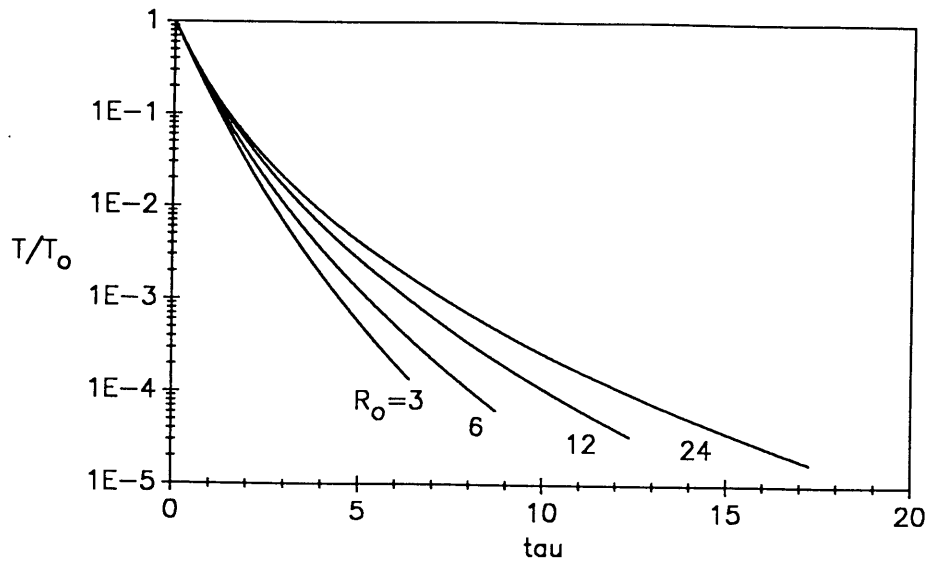


Figure 7.4

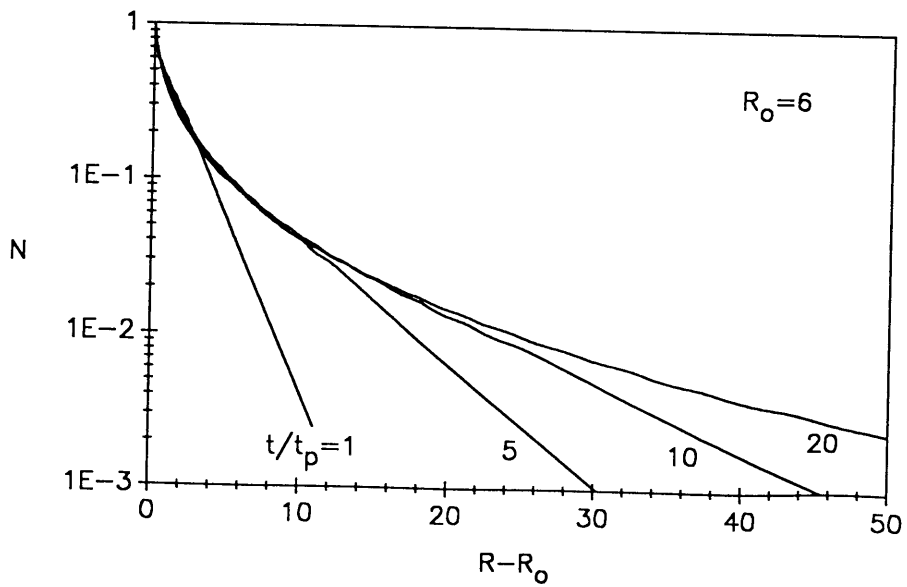


Figure 7.5



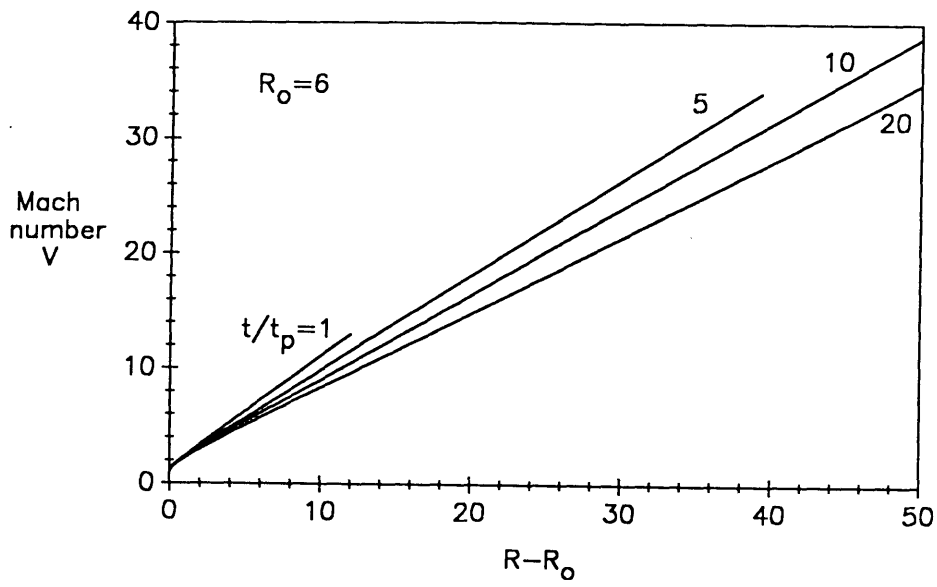


Figure 7.6

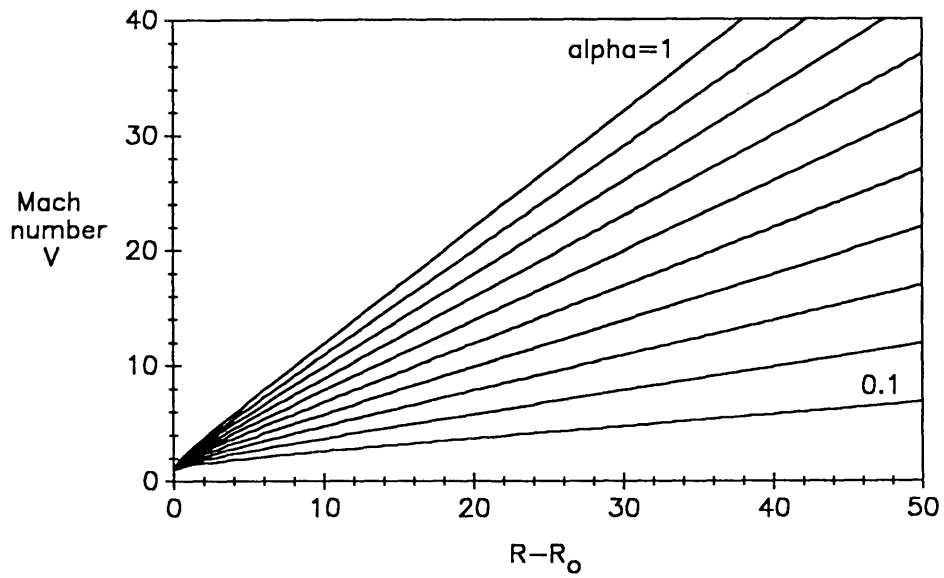


Figure 7.7

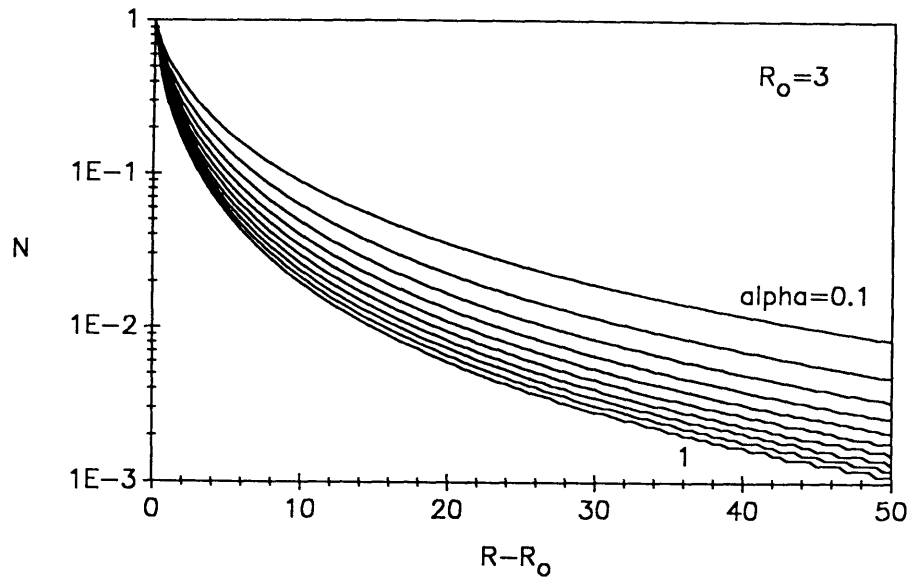


Figure 7.8

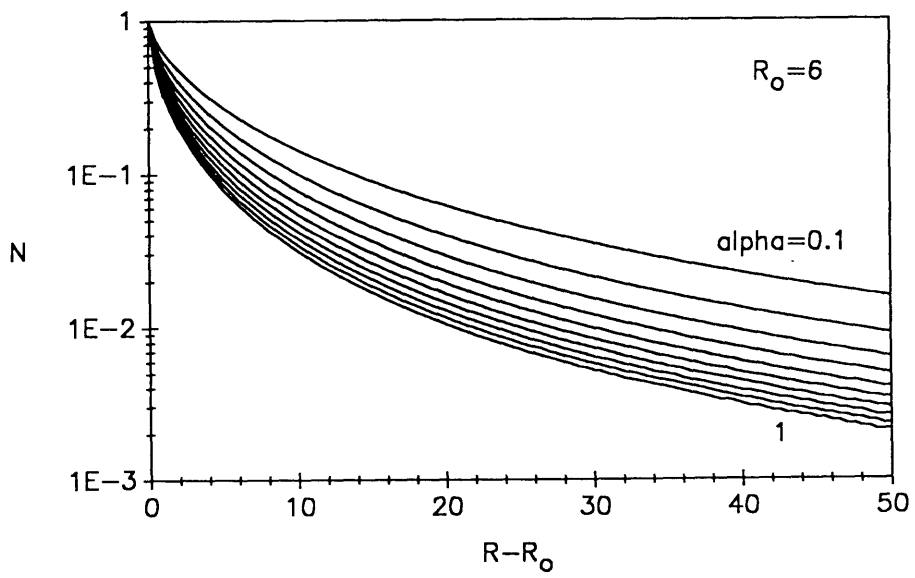


Figure 7.9

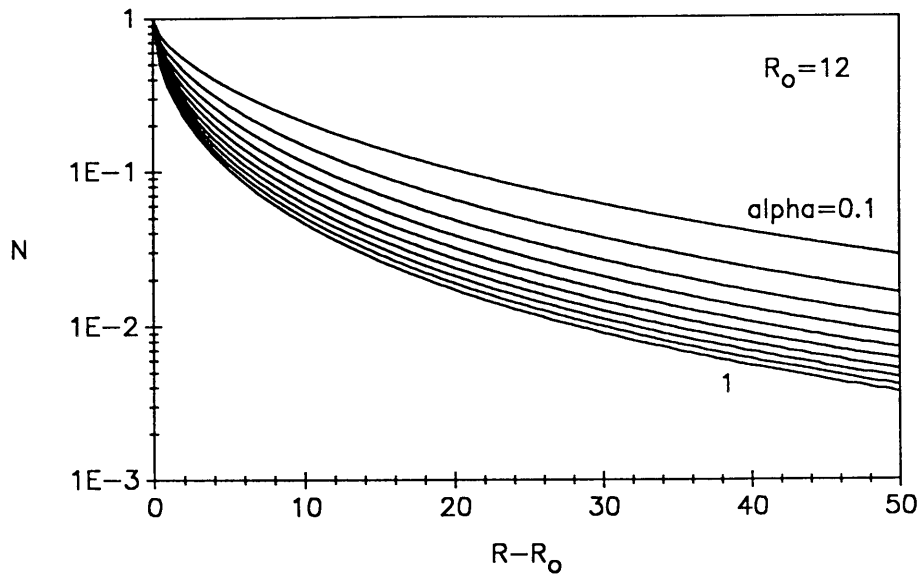


Figure 7.10

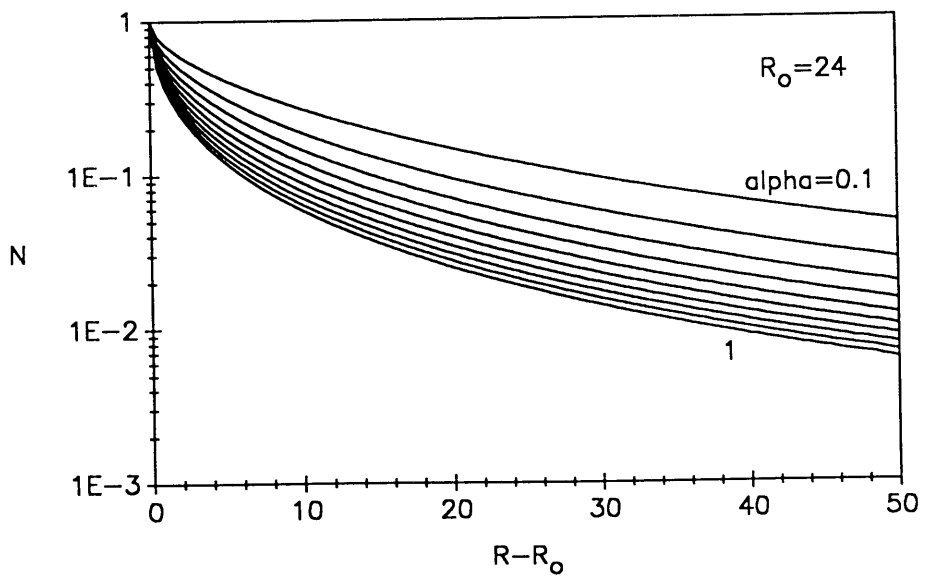


Figure 7.11

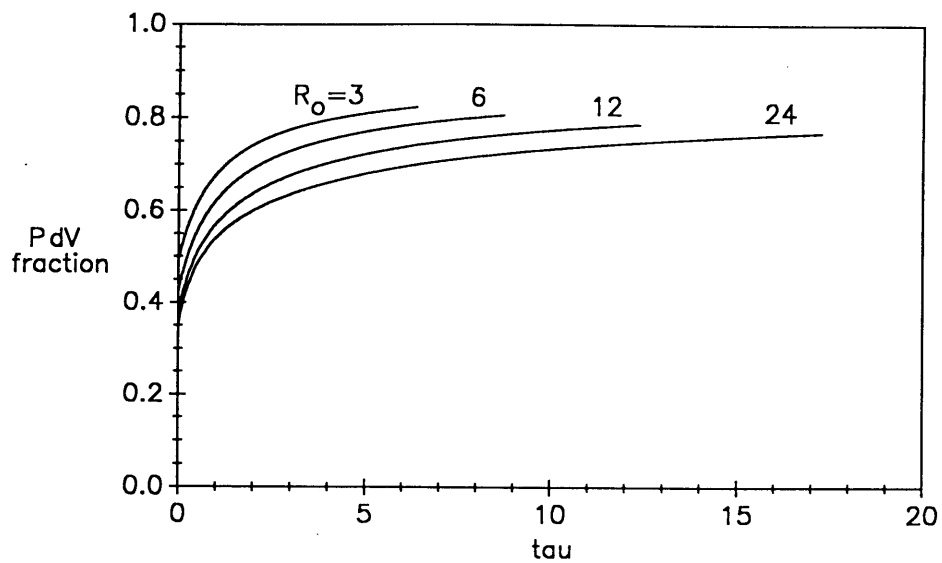


Figure 7.12

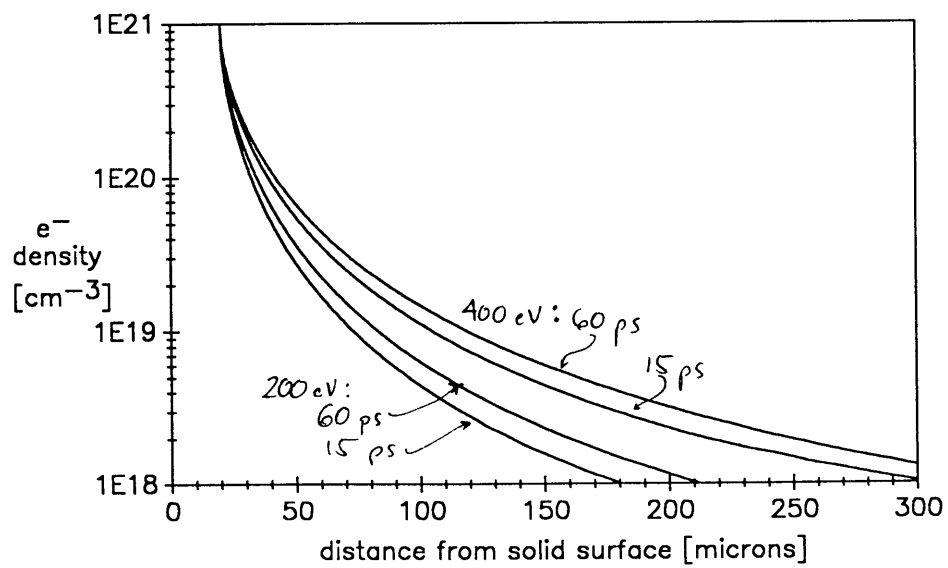


Figure 7.13

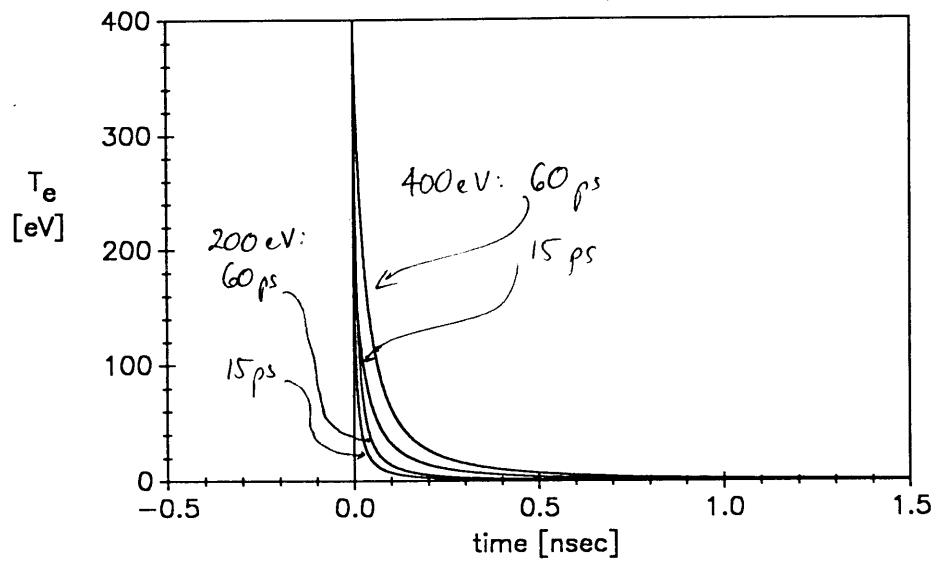


Figure 7.14

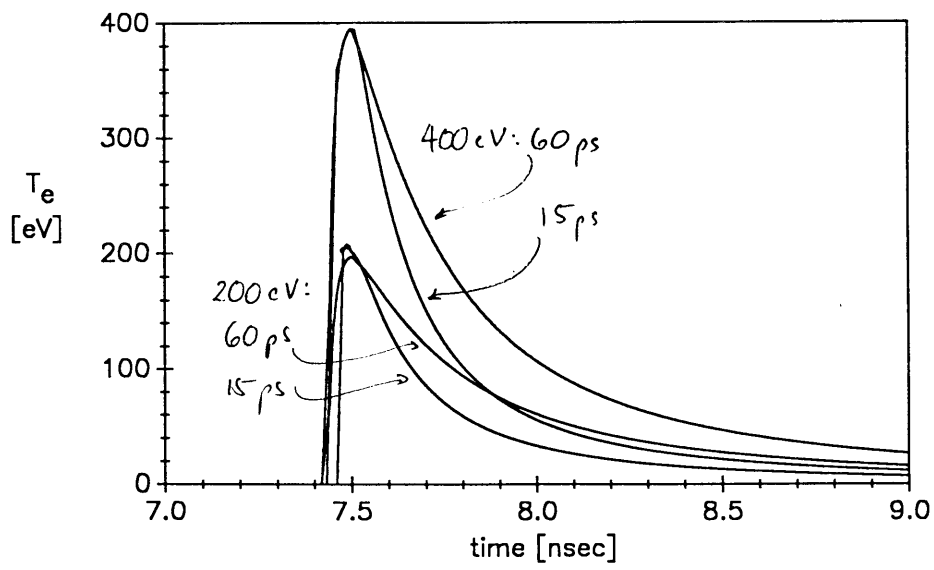


Figure 7.15



# Chapter 8

## Experimental studies

### 8.1 Introduction

In this chapter, the experimental work on measurements of soft x-ray gain will be summarized. The diagnostic instruments and spectroscopy will be described, followed by the experimental results and discussion.

The calculations in Chapter 6 were made for the ionic species Ni-like Mo ( $Z = 42$ ), with a lasing wavelength near 188 Å. Because of the reflectivity cutoff of the principal spectrometer near 200 Å, it was found necessary to concentrate efforts on the ion of neighboring  $Z$ , Ni-like Nb ( $Z = 41$ ), which is expected to lase at 204 Å. The substitution is insignificant other than that the gain is optimized at slightly lower density and temperature.

Strong indications of stimulated amplification were seen. A gain  $\alpha$  of about  $5 \text{ cm}^{-1}$  and a gain-length product  $\alpha\ell$  of about 1.5 were inferred for a 3-mm-long plasma column at energies of about 1.1 J in 60 psec. Higher intensities than expected were required, and ultimately  $\alpha\ell$  was limited by the available pump laser power. Present efforts toward laser pulse compression should greatly increase the gain-length product.

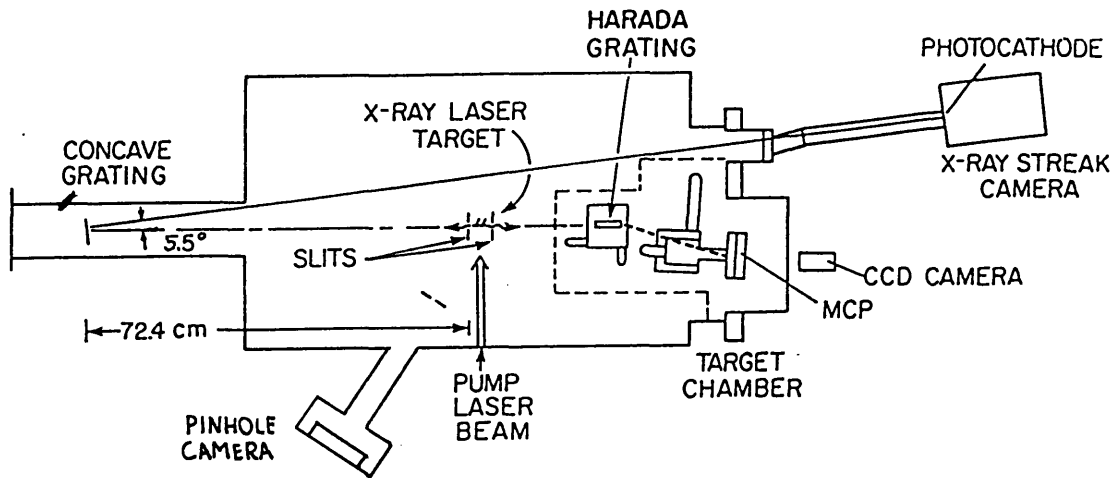


Figure 8.1: Target chamber and diagnostics (top view)

## 8.2 Instrumentation and diagnostics

### Target chamber and targets

An overview of the target chamber and plasma diagnostics appears in Figure 8.1. The pump laser beam lies approximately in the plane of the picture; the surface of the target is perpendicular to that plane. The line focus is formed in the plane, and two spectrometers are aligned axially to the line. A pinhole camera is used to image the hot plasma.

The target chamber, which has a volume of 200 liters, is normally used at a vacuum of  $10^{-6}$  torr. Two orthogonal He-Ne lasers define the x-ray laser axis and a normal to it. The axial He-Ne is used to position the two spectrometer slits, the target surface, and the concave grating wavelength setting (using a back reflection from the grating). The perpendicular He-Ne is used to set the target position and rotational angle (using a reflection from the target surface). With the pump laser at low power, the target can be imaged using a CCD camera to allow optimization of the line focus size and position on the target. The target is stepped about  $500 \mu\text{m}$  vertically between shots to expose fresh



material.

The adjustment of the spectrometer slits relative to the target surface was critical. Two types of slits were investigated: one which was fixed in space while the target was moved alongside it, and one in which the slit and the target were fixed to one another, the alignment having been done previously outside the chamber. The first had the advantage that the height above the target surface which the spectrometer was viewing could be adjusted during the course of the experiments, without breaking vacuum; a disadvantage was that the height was not precisely defined with respect to the target. This problem was addressed by using the axial He-Ne laser to establish the relative position of the slit to the target initially; an encoder motor was then used to move the target repeatably and reliably. Ultimately, the results using both slit types agreed well.

Two types of targets were used: solid metal and metal-coated Si wafers (1-3  $\mu\text{m}$  thick films). The Si wafers had the advantage of having a very flat and uniform surface, but were fragile, expensive, and non-reuseable; and they had the potential to introduce impurities (Si and dopants) into the spectra. The solid targets could be hand lapped to a surface microroughness of about 8 microinches and high flatness, and were easily refurbished when the surface had been consumed. Experimentally, no significant difference was seen in the performance of the two types of target; consequently most of the present experiments were done using solid targets (in an earlier series of experiments, S. Basu reported observing more consistent behavior of the 204 Å line when using Si wafers).

## Concave grating spectrometer

The principal diagnostic in these experiments was a streaked concave grating spectrometer, built by S. Basu, with a 3600 lines/mm  $32 \times 30$  mm gold-coated concave grating of 1000 mm radius of curvature and  $304\text{\AA}$  blaze wavelength. A LLNL streak camera provided time resolution to  $\sim 30$  psec at the fastest setting (1 nsec/sweep); the images were recorded on Polaroid 667 film, which was then digitized and analyzed.

Since the grating is used near normal incidence, it creates a nearly stigmatic image at the streak camera photocathode. The incidence angle also accounts for the low reflectivity, which drops rapidly below  $10^{-3}$  at  $200\text{\AA}$  (this does have the benefit that lines in higher order are eliminated). In the present configuration, the plate factor is  $1.40\text{\AA}/\text{mm}$  on the streak camera intensifier plate, and the wavelength coverage is  $22\text{\AA}$  on each picture.

The theoretical wavelength resolution of this instrument seems not to have been realized in this series of experiments. Experiments were performed to optimize the focus using a target with a  $50\text{ }\mu\text{m}$  slit rigidly attached to it, and adjusting the distance of this assembly from the grating. At optimum, lines in Ni-like Nb could be resolved to about  $0.7\text{\AA}$ ; this resolution was insensitive to the target assembly position within a range of about 1 cm. These results suggest that the optimal slit size is around  $100\text{-}200\text{ }\mu\text{m}$ ; smaller slits will not increase resolution, only decrease signal. This conclusion agrees with experimental observations.

The result of the poor resolution was to worsen the signal-to-noise ratio; since the background emission was high for the Ni-like targets, weak signals could easily be obscured and spurious signals suggested by features in the background. An additional problem with the spectrometer was a systematic intensity variation across the width of its output; the long wavelength wide

tended to be brighter by a larger factor than could be explained by the grating reflectivity variation. It was hypothesized that the streak camera photocathode was poorly aligned to the spectrometer dispersion direction.

## **Harada grating spectrometer**

A grazing-incidence Harada (varied line-space) grating spectrometer serves to record 3–4 resonance transitions in the 50 Å region in Ni-like and neighboring ionic species. To date, it has been used in time-integrated mode to verify the presence of Cu-like, Ni-like and Co-like ions under the appropriate irradiance. It can also indicate the presence of narrowed-divergence-angle radiation since it does not image in the non-dispersive dimension. This spectrometer will become far more useful when it is interfaced with a streak camera, so that ion populations can be closely observed as functions of time.

## **Pinhole camera**

A pinhole camera was used to image the bright 10-100 Å radiation emitted by the high density center of the plasma. Images were recorded directly on Polaroid 107 uncoated film. The most useful configuration used two perpendicular slits positioned to give 7:1 magnification. The horizontal slit was chosen to be 30 μm wide, which gives a diffraction-limited resolution of 25 μm at 100 Å across the plasma column width. The resolution along the plasma length was of less interest; a vertical slit width of 100 μm was chosen in order to increase the light-gathering ability. A thin polymer filter could be used to eliminate longer-wavelength radiation. This proved unnecessary with properly chosen slit sizes, since the longer wavelengths suffer higher diffractive loss in proportion to their wavelength.

An image of a 3-mm-long plasma irradiated with 5 60-psec pulses at 0.7 J



Figure 8.2: Pinhole camera image

is reproduced in Figure 8.2. The width of the image measures  $300\ \mu\text{m}$ , which places an upper limit of  $43\ \mu\text{m}$  on the plasma width. The pump beam focal width is  $15\text{--}20\ \mu\text{m}$ ; lateral electron thermal conduction is expected to cause a region of  $30\text{--}40\ \mu\text{m}$  to be heated, so the agreement is good. In this way, the pinhole camera verifies the near-diffraction-limited beam quality of the pump laser optical system at full power.

## 8.3 Spectroscopy

### Overall structure

An understanding of the spectra of the Ni-like ion as well as of neighboring ions is important for several reasons. First, known lines serve as static wavelength references. Second, the identification of species present in the observed spectrum diagnoses the ionization balance and temperature. Third, since the candidate laser lines have not been previously observed, it is vital to be aware of what known lines should be seen, where they should lie, and whether they might obscure or impersonate the laser line. This section reviews the known spectra of the  $4\text{--}4$  transitions in Ni-like and nearby charge state species, and presents spectroscopic observations confirming the presence of various charge states.

The Ni-like spectrum includes bright  $3d\text{--}4p$  and  $3d\text{--}4f$  resonance lines in the  $50\ \text{\AA}$  range and a large number of weaker  $4\text{--}4$  excited-state transitions in

the 200-400 Å range [41]. The Ni-like  $4p-4d$  transition array includes over 100 allowed transitions (about 80% of the total line strength is found in the 20 strongest lines). Most of these lines share a very dense spectral region above 240 Å with the  $4-4$  lines of the nearby lower charge states, which will coexist with the Ni-like species.

The primary x-ray laser line,  $4p^1P_1-4d^1S_0$ , lies detached from the other lines in a comparatively simple spectral region near 204 Å. This occurs because the  $^1S_0$  upper state shares a common  $J$  and parity with the ground state and is consequently elevated in energy by the configuration interaction in addition to the exchange integral. The same fact makes the energy level difficult to predict from *ab initio* calculations.

Other candidate laser transitions include the  $^3D_1-^1S_0$  near 211 Å, the  $^1P_1-^1D_2$  at 255.59 Å, and the  $^3D_1-^1D_2$  at 267.73 Å. Weaker gains are predicted for these transitions; this has been verified in the demonstrated high- $Z$  Ni-like experiments [72]. Except for the 255.59 Å line, none of these lines, including the 204 Å line, has been observed previously. Virtually all of our effort was placed in the search for gain at 204 Å, although a short study was done near 260 Å.

As a rough model of the level structures of the nearby ions, the Grotrian diagram of Cu-like Nb is reproduced in Figure 8.3. It can be seen that the  $4p-4d$ ,  $4d-5p$ , and  $4f-5g$  arrays lie in the wavelength range of interest, and the  $4p-5s$  is somewhat shorter in wavelength. The neighboring ions show a similar structure, but the arrays are split into many more transitions because of the coupling with the other electrons in non-filled shells. Also, the lower charge states have arrays involving doubly-excited states, some of which will also be in the relevant wavelength range.

The principal  $4p-4d$  arrays of all the species from Br-like ( $Z_c = 7$ ) to Ni-

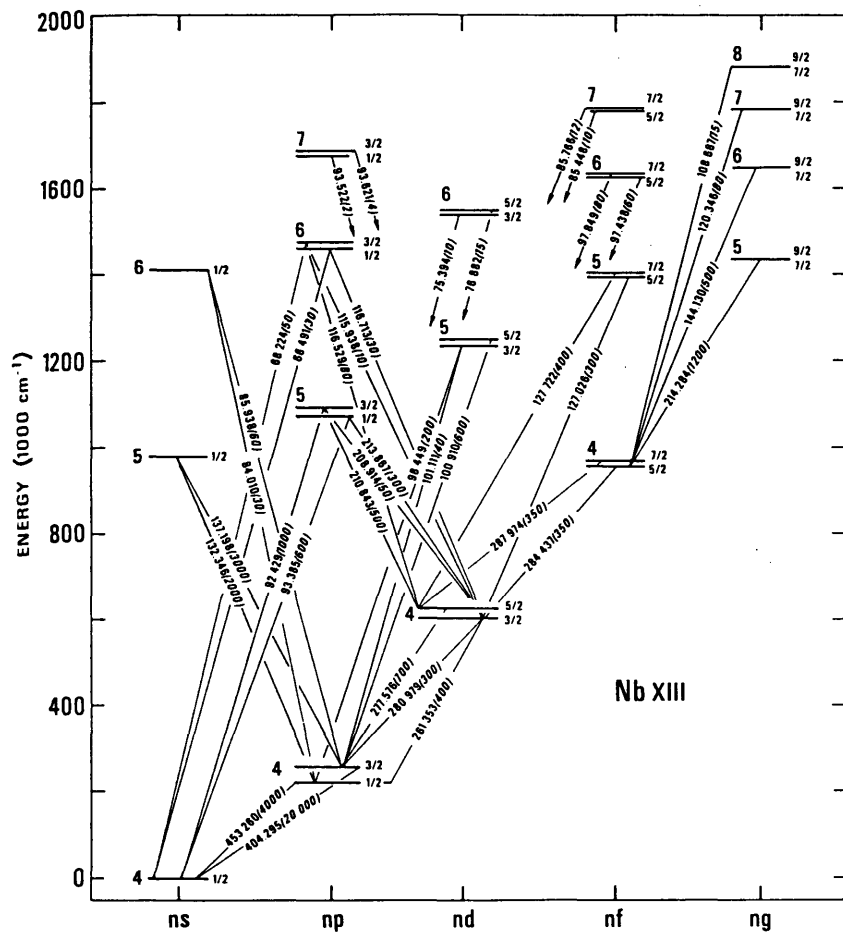


Figure 8.3: Grotrian diagram for Cu-like Nb [36]

like Nb have been analyzed, together with some of the other arrays (the 4–4 transitions of the Co-like and higher charge states have not been studied at all, to our knowledge). In Figure 8.4, we have compiled and charted all of the observed arrays for these species [41,36,42,43,44,45,46,47,48].

As the figure shows, the 4–5 wavelengths increase rapidly with decreasing charge state, but the 4–4 wavelengths do not shift appreciably. The region above 240 Å is very dense in weak 4–4 spectral lines and is consequently a difficult region in which to work. The  $4p$ – $5s$  transitions do not enter the range of interest until the Se-like sequence is reached, and it is unlikely that a significant population of this sequence, or lower ones, will coexist with the Ni-like species. The Ni-like  $4d$ – $5p$  and  $4f$ – $5g$  lines, though undocumented, are likely to lie at shorter wavelengths than 200 Å.

The 204 Å laser line, therefore, lies relatively isolated, with only the easily-identified  $4d$ – $5p$  and  $4f$ – $5g$  lines of the adjacent Cu-like species. This situation is ideal for spectroscopy, since the Cu-like lines can be viewed simultaneously with the laser line (the spectrometer wavelength window is 22 Å); they serve as a convenient temperature and alignment diagnostic as well as a wavelength reference.

The overall structure of Figure 8.4 applies to laser systems of neighboring  $Z$  such as Mo and Zr. The 4–5 transitions shift to shorter wavelength relative to the 4–4's with increasing  $Z$ , so for Mo, the Cu-like lines are seen near 180 Å, on the short-wavelength side of the  $^1S_0$  gain line expected near 189 Å. In Zr, the Cu-like lines fall at considerably longer wavelengths (near 250 Å) than the gain line (221 Å), so these lines cannot be viewed simultaneously on our spectrometer.

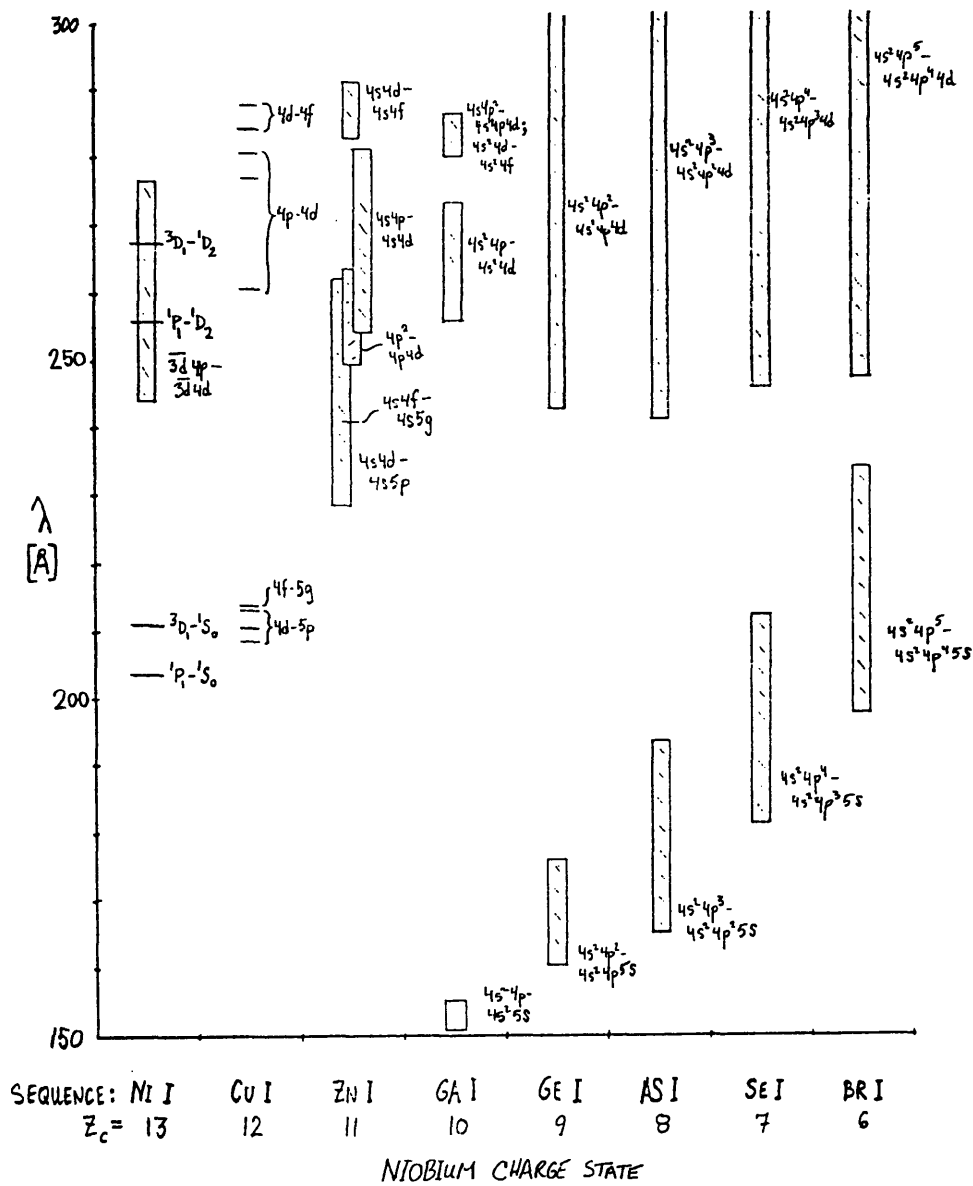


Figure 8.4: Nb transition arrays near 200 Å. Ni-like transitions with term labels are candidate laser lines;  $^1P_1-^1S_0$  is the principal line.



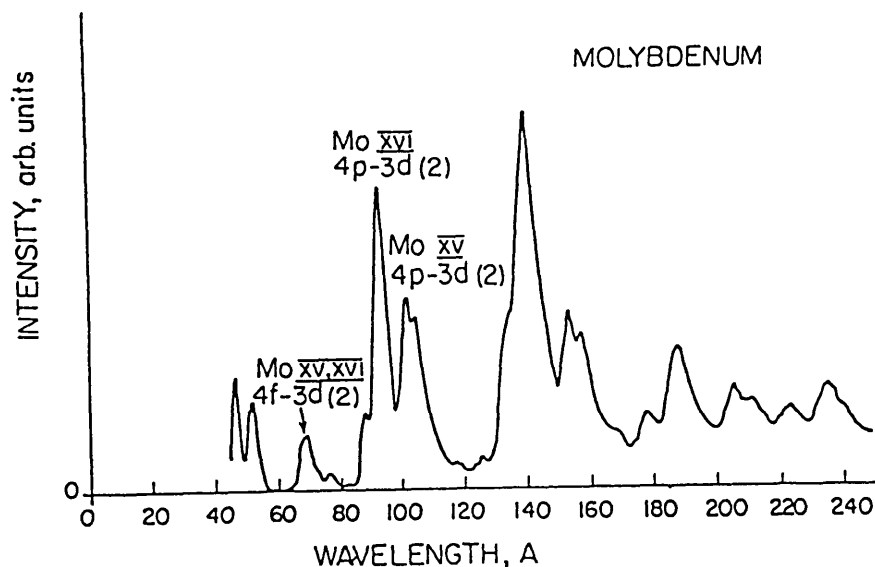


Figure 8.5: Time-integrated Nb spectrum: 3–4 resonance lines

## Experimental spectroscopy

In an early series of experiments, it was found by S. Basu that Ni-like ions are generated at the intensities of interest ( $3\text{--}5 \times 10^{12} \text{ W/cm}^2$ ) [49]. The work was done in Mo using the time-integrating Harada grating spectrometer to view the  $\sim 50 \text{ \AA}$  3–4 resonance lines in second order.

A lineout of the data is shown in Figure 8.5. Resonance lines of the Ni-like and Co-like species were identified, as were satellite transitions in the Cu-like species. This work confirms both that Ni-like ions are present and that 3–4 excitation occurs in the plasma.

Using the streaked concave grating, it was attempted to monitor the presence of Ni-like ions as a function of time by observing the strongest (still relatively weak)  $4p\text{--}4d$  line, which occurs at  $269 \text{ \AA}$ . Although the nearby strong Cu-like  $4p\text{--}4d$  line at  $261 \text{ \AA}$  was prominent, the Ni-like line could not be discriminated from a large number of other weak 4–4 lines.

Another study was performed to determine whether the  $4p\text{--}5s$  lines of the

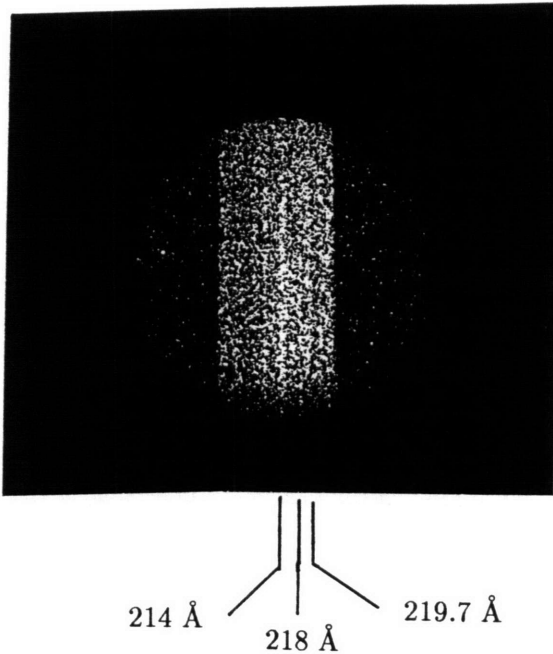


Figure 8.6: Streaked spectrum showing Br-like Nb lines at  $2 \times 10^{12}$  W/cm<sup>2</sup>

Se-like and Br-like species near the gain line were visible. Br-like Nb has strong lines at 217.95 Å and 219.74 Å. These lines were not visible simultaneously with the strong 210-215 Å Cu-like lines at intensities of  $5-10 \times 10^{12}$  W/cm<sup>2</sup>. When 10 shots at  $2 \times 10^{12}$  W/cm<sup>2</sup> were overlaid on film, the lines became visible (Figure 8.6). It was concluded that at the typical intensities and temperatures of interest, the ionization distribution does not include significant quantities of these lower-charge-state ions.

## Impurities

Since the target samples were high purity materials, it was expected that the only impurities in the spectra would arise from surface contamination by oxides or H<sub>2</sub>O. Since hydrogen has no lines over 13.6 eV, the only impurity ion expected was oxygen. A list of known oxygen lines near 200 Å appears in Table 8.1.

The lines near 203 Å were a source of concern for our investigations near

$\lambda$ [Å]	Intensity	Transition
183.9-184.1	400	O VI $2p-3s$
185.7	450	O V $2s2p-2p3p$
192.8-192.9	800	O V $2s2p-2s3d$
202.2-203.9	300	O V $2p^2-2p3d$
215.0-216.0	500	O V $2s2p-2s3s$
220.4	800	O V $2s2p-2s3d$

Table 8.1: Oxygen transitions in the 200 Å region (from [50])

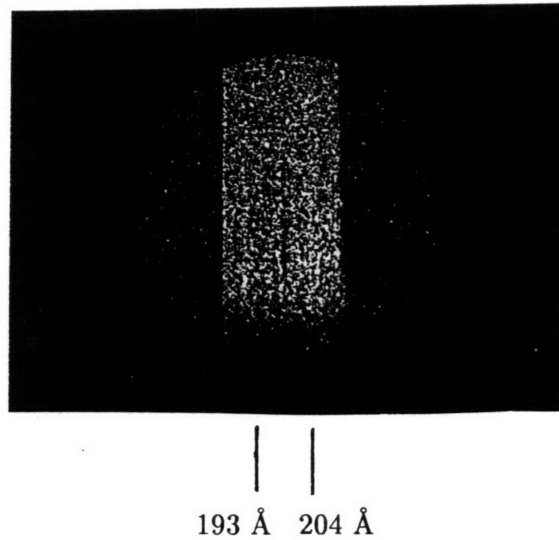


Figure 8.7: Streaked spectrum from 185 Å to 207 Å at  $10^{13}$  W/cm<sup>2</sup> in Nb

204 Å. These O V lines have been observed blended with the Br-like and Se-like Nb  $4p-5s$  lines, however, which suggests that the oxygen should be overionized at the temperatures in which Ni-like Nb is present [47]. In order to confirm that the suspected gain line near 204 Å was not O V, shots were taken at a spectrometer setting spanning the range from 185 to 207 Å. When the 204 Å line became visible at  $10^{13}$  W/cm<sup>2</sup>, no lines were seen near 193 Å (Figure 8.7). It was concluded that O V was absent from the spectra.

## Absorption mechanism observations

In section 6.4, it was mentioned that the pump beam is angled at  $12^\circ$  to the target normal in order to promote resonance absorption and increase pump efficiency. The contribution of resonance absorption to the total absorption was measured experimentally and is summarized here.

Since resonance absorption occurs only for  $p$ -polarized light, it is possible to eliminate it by rotating the polarization. Shots were taken in each polarization at  $5 \times 10^{12}$  W/cm<sup>2</sup> and streaked spectra of the Cu-like  $4d-5p$  transitions obtained for the first and second pump pulses. These pictures are shown in Figure 8.8.

On the second pulse, the Cu-like line emissions in the two polarizations were practically indistinguishable. The pump energy was increased 20% and observations repeated; the emission brightness increased significantly. Comparing the brightness increase due to the 20% energy increase to the brightness difference between the two polarizations allowed us to infer an upper limit of 5% on the contribution of resonance absorption to the net absorption. Because the plasma is large and initially cold, the absorption is dominated by inverse Bremsstrahlung.

The first pulse showed much dimmer emissions since the inverse Bremsstrahlung was much less; a correspondingly higher fraction of resonance absorption was observed. The Cu-like lines were barely discernible in the  $s$ -polarized case and were brighter in the  $p$ -polarized case by a factor of 2-3. Resonance absorption was inferred to be at least comparable to inverse Bremsstrahlung, if not stronger. This observation has little impact on our collisionally-pumped schemes, where only the absorption on the second pulse is critical. It has significance, however, for the efforts in recombination lasers [51], where only the first pulse is used. The incidence angle for resonance absorption should

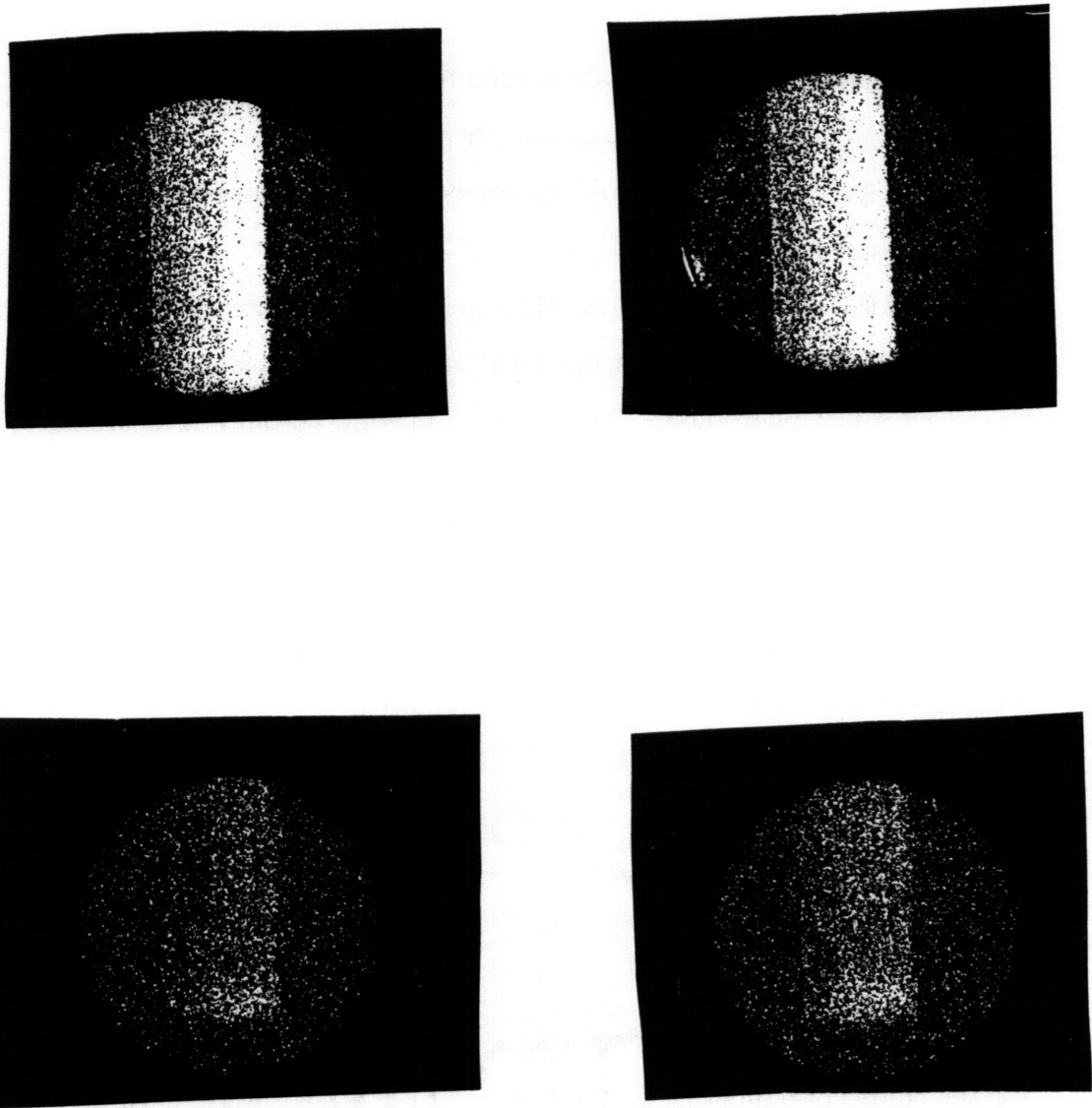


Figure 8.8: Absorption measurement data: Cu-like Nb 210.8 Å and 214 Å lines in 1 nsec streaked spectra. Top: second pulse; bottom: first pulse. Left: *s*-polarized pump beam; right: *p*-polarized.

be optimized, either experimentally or computationally, since a deviation from the optimum could affect the net absorption by a significant factor. This point will be especially critical for these efforts when the pump laser is configured for shorter (15 psec) pulses, which will experience even less inverse Bremsstrahlung on the first pulse.

Values of the absolute absorption efficiencies would be interesting to obtain and might be estimated by measuring the reflected pump radiation on each pulse using a fast photodiode. The need for making absolute measurements of the total reflected flux could be circumvented: since the first-pulse absorption is small, the reflectivity on that pulse should be near unity. Comparing the reflected intensities for the two pulses will then give an estimate for the net reflectivity on the second pulse. The impact of scattering losses on this measurement technique would need to be evaluated.

## **8.4 Gain studies**

### **Introduction**

In this section the results of our searches for amplification will be summarized. Over the course of 6 months, on the order of 1000 spectra were taken on full-power laser shots in a fairly exhaustive search through the range of parameters accessible by our system. The suspected laser line became visible at intensities somewhat higher than predicted. Although the damage limit of the driver laser prevented the generation of long line foci (and consequently high net gains) at these intensities, the laser line emission was seen to grow nonlinearly in the focus length. It was also directional and had a much shorter lifetime than than the neighboring Cu-like lines. However, the suspected laser line showed an unexpectedly broad linewidth; more study is required to understand this.

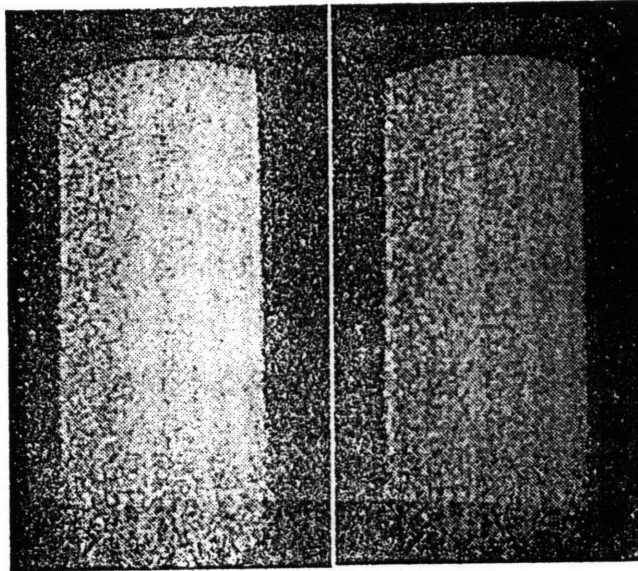


Figure 8.9: Streak camera data: on the left, original data; on the right, corrected computer replication. The direction of the time sweep is upward, spanning 1 nsec and starting at the beginning of the second pump pulse.

These and other observations will be discussed in this section.

Successful shots occurred only within a narrow range of parameters. In almost all of the results to be presented, the plasma was observed on the second pump pulse using a  $200 \mu\text{m}$  spectrometer slit, the pump energy was 1.1 J per 60-psec pulse, and the line focus length was 3 mm.

An earlier series of experiments was performed by S. Basu; at that time, the pump laser pulse duration and energy were poorly known, and the laser was apparently run at up to twice its design intensity. At these high intensities, several shots suggested very significant gain.

An example of the streak camera data is reproduced in Figure 8.9. This example was from one of the higher-gain shots from the earlier experiments. On the left is the original data; on the right, a computer replication which has been corrected for the diffraction grating reflectivity variation and the saturation of the Polaroid film on which the picture was taken. The strong

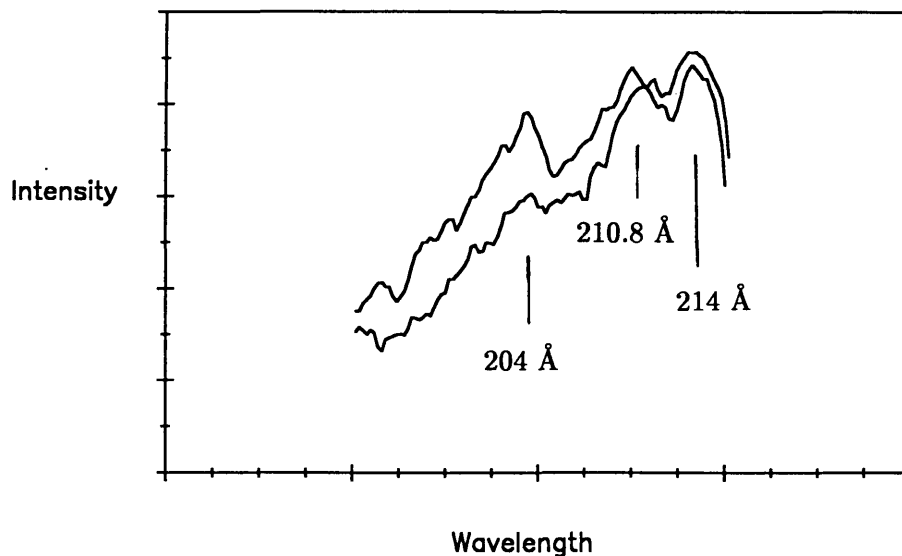


Figure 8.10: Lineouts for point focus (lower) and line focus (upper). The spectra were integrated over a time of 1 nsec.

lines which are visible include, from left to right, the candidate laser  $^1S_0$  laser line at 204.2 Å and the strong Cu-like  $4d-5p$  and  $4f-5g$  lines at 210.8 Å and 214 Å. The high degree of background continuum is to be noted; this made observation of weak signals very difficult.

Qualitative evidence of x-ray amplification is given by comparison of emission from a point focus on the target and a line focus under similar plasma conditions. In Figure 8.10, lineouts are shown from two typical shots at equal intensities; the lower line corresponds to a point focus and the upper to a line focus. The lineouts are largely identical except that the spectral feature at 204 Å grows from being obscure to being very prominent. (Here, and henceforth except in the following section, the lineouts have not been corrected for grating reflectivity or film saturation; the former is unnecessary since no quantitative comparisons are being made across different wavelengths, and the latter because the gain line is not saturated in these data.)



## Gain dependence on pumped plasma length

The gain coefficient was measured by varying the length of the line focus length on the target over the range from 1 mm to 3 mm. The lineout data that were used appear in Figure 8.11; these data have been corrected for grating reflectivity and film saturation, and were integrated over a time of 1 nsec. At each length, one shot was taken at a height of 75  $\mu\text{m}$  and one at 100  $\mu\text{m}$  above the target surface. Each shot was at 1.1 J energy at the amplifier, and for the shorter line lengths, the beam was clipped before striking the target. This ensured that the intensities and beam quality were identical on each shot.

The heights of the 204  $\text{\AA}$  peak were measured and the values fit to the Linford formula [52], which describes the growth of the ASE-mode emission with the length  $\ell$  of the gain medium:

$$I = \frac{J_s (e^{\alpha\ell} - 1)^{3/2}}{\alpha (\alpha\ell e^{\alpha\ell})^{1/2}},$$

where  $\alpha$  is the gain coefficient and  $J_s$  the spontaneous emission. A plot of this fit appears in Figure 8.12.

The inferred gain value of 5  $\text{cm}^{-1}$  agrees reasonably with the gains of 3-4  $\text{cm}^{-1}$  over longer lengths measured during the earlier series of shots. It is possible that because of the shorter line focus used presently, the intensities (and therefore gains) were higher. Also, the present estimates have a large possible error since the lengths were so short and the gain-length product so low.

## Gain dependence on plasma height over target

Careful optimization of the height of the spectrometer slit above the target surface was required to obtain significant signal at 204  $\text{\AA}$ . Emission was observed from only a localized low-density region, rather than from the high

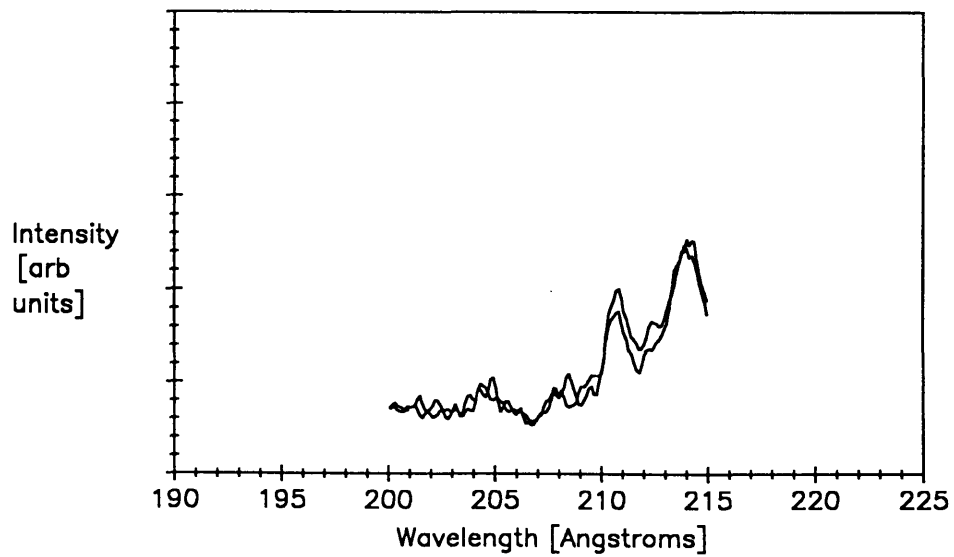
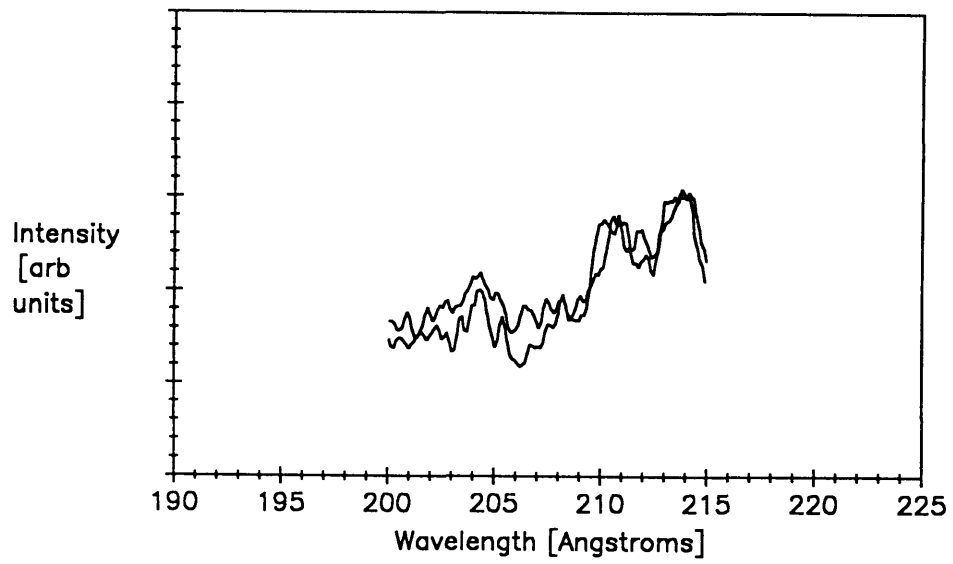
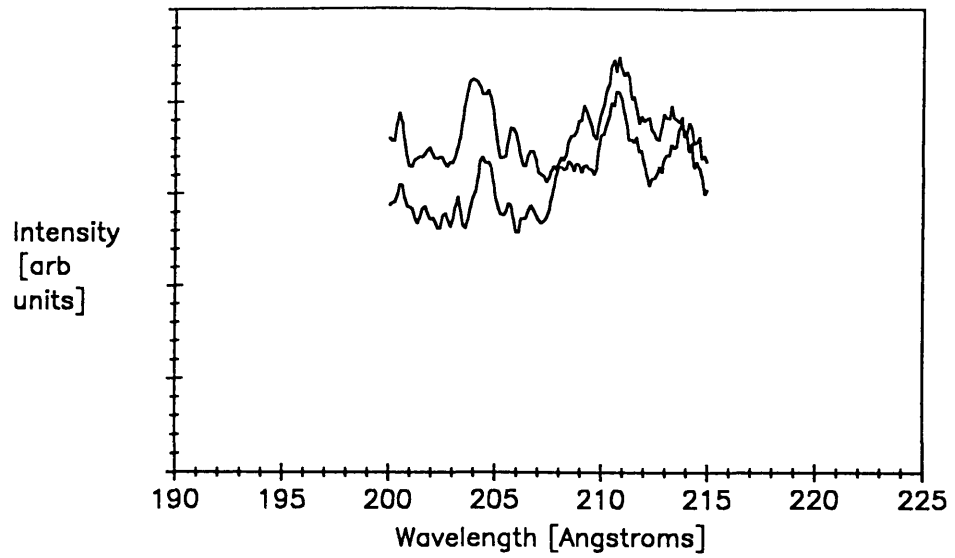


Figure 8.11: Corrected lineouts for 3 mm, 2 mm, and 1 mm long line foci (one shot each at  $75 \mu\text{m}$  and  $100 \mu\text{m}$ ); integrated over 1 nsec

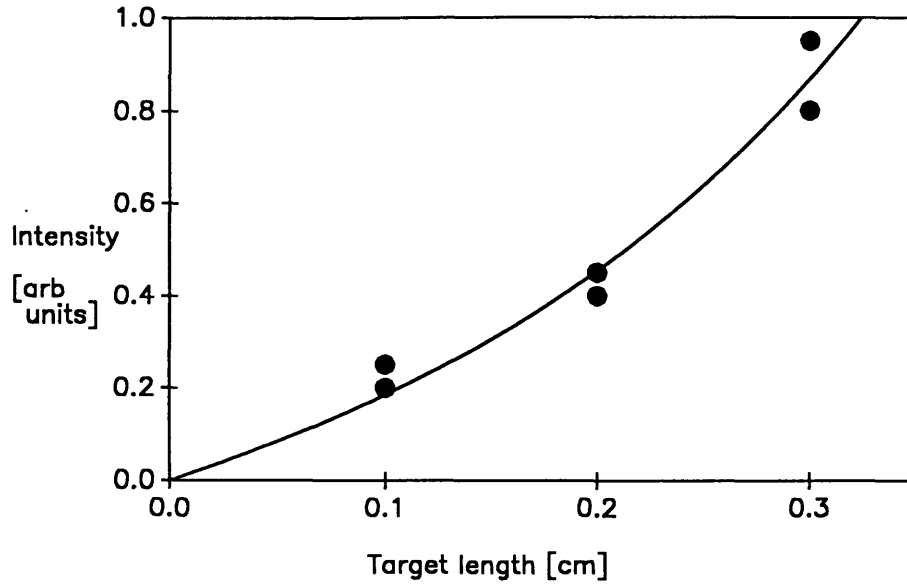


Figure 8.12: Observed gain vs. length and best-fit Linford curve

density region near the target surface, where the Cu-like lines are strongest. This observation provides further evidence of amplified emission.

Lineouts are shown in Figure 8.13 for slit heights of  $50\ \mu\text{m}$  through  $150\ \mu\text{m}$  above the surface. The zero was set using a He-Ne laser on the spectrometer axis. It can be seen that the peak at  $204\ \text{\AA}$  is maximized over the background around a slit height of  $75\text{-}100\ \mu\text{m}$ . This is in good agreement with the prediction of the model in Chapter 7 that the region of density about  $1\text{-}2 \times 10^{19}\ \text{cm}^{-3}$ , where gain is expected, should occur at a distance of about  $100\ \mu\text{m}$  from the target surface.

### Temporal behavior of gain line

The streak camera data were analyzed in the temporal direction to determine the behavior of the suspected gain emission and the Cu-like emission as a function of time. Typical lineouts for the gain line and the Cu-like  $4f\text{-}5g$  line appear in Figure 8.14. The rapid turn-on of the  $204\ \text{\AA}$  emission as seen here is

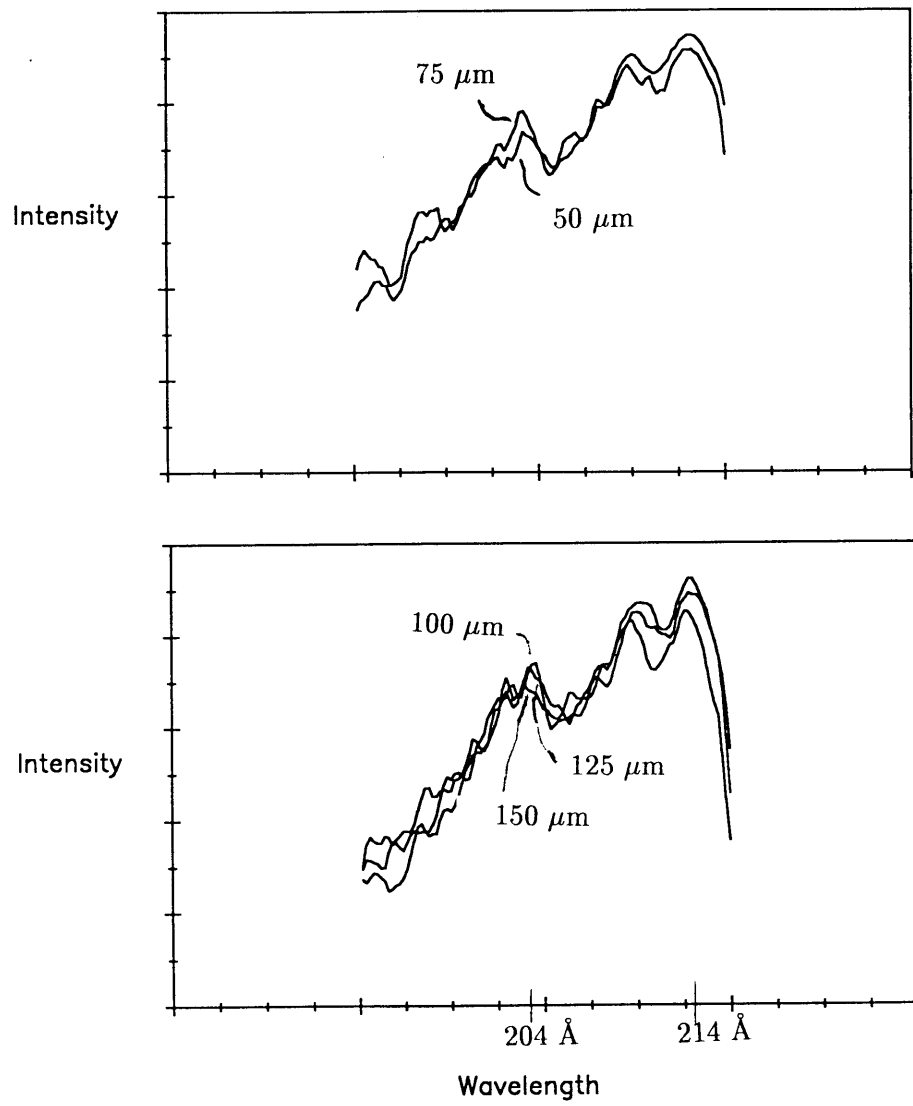


Figure 8.13: Lineouts for slit heights of 50-150  $\mu\text{m}$  above target surface

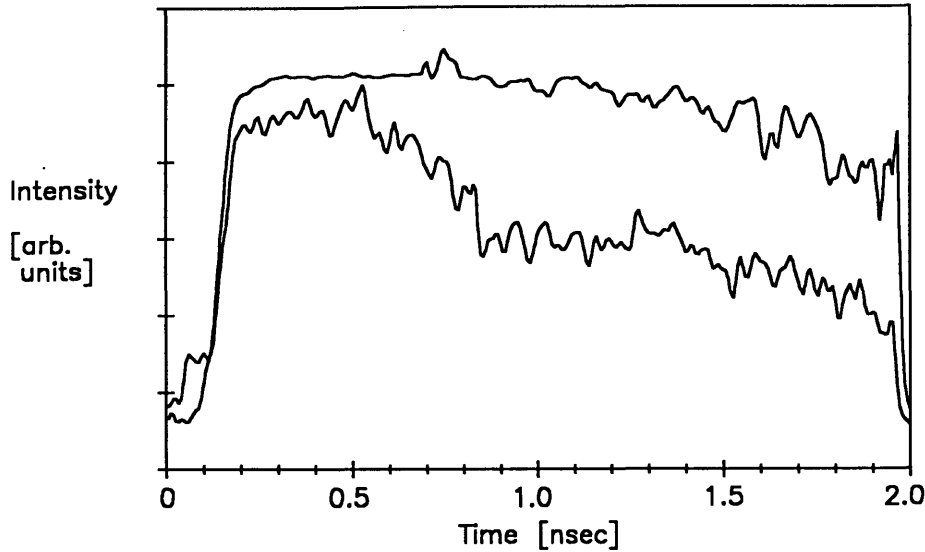


Figure 8.14: Temporal behavior of gain line (lower) and Cu-like  $4f-5g$ . These data are integrated over a wavelength range of  $1 \text{ \AA}$  and are not corrected for grating reflectivity or film saturation.

in agreement with the inference of Section 6.7 that at densities of  $10^{19} \text{ cm}^{-3}$ , it should take only about 100 psec for ionization to occur from the Cu-like to the Ni-like state at temperatures of 150-200 eV. It can also be seen that whereas the Cu-like emission is present for around 2 nsec on this shot, the gain line emission abruptly falls to the background level after 500-700 psec.

Ni-like ion emissions would in general be expected to be slightly shorter-lived than the Cu-like because plasma recombination will lower the Ni-like population sooner than the Cu-like; this should not however cause such a drastic difference in lifetime as observed. The collisionally-pumped gain is known to be strongly temperature-dependent, more so than is the ionization balance. As discussed further in section 8.5, the observed behavior suggests that the  $204 \text{ \AA}$  emission not only is associated with a Ni-like line, but also is demonstrating collisionally-pumped gain.

## Angular behavior

Even at the modest gain-length product measured here, the amplified emission is expected to be highly directional. A series of full-power shots was taken with the gain line evident, and the axial direction of the pump line focus was varied by rotation of the cylindrical focusing optic.

The spectrometer has an acceptance full angle of 40 mrad, and the divergence angle expected from a  $40 \mu \times 3$  mm line focus is on the order of 20 mrad. Therefore, the spectrometer acceptance dominates the angle over which the emission is expected to be seen.

The 204 Å emission was seen to fall to half its intensity over background at around 20-30 mrad off axis, and to be virtually extinguished at 40 mrad (Figure 8.15). The Cu-like line intensities are also observed to drop somewhat. If these lines are optically thin, then this behavior is to be expected: at oblique incidence, the amount of Cu-like emission emanating from the region observed by the spectrometer will drop. The 204 Å line would show similar behavior if it were radiating purely in spontaneous emission, whereas if it were radiating in ASE with substantial gain, then it would show a much stronger drop-off.

The observed behavior is in agreement with the latter picture; the 204 Å emission falls away much more rapidly than does the Cu-like emission. The angle over which this drop-off is seen to occur is consistent with the spectrometer acceptance angle and the expected emission divergence.

## Gain line linewidth

An additional indication of gain behavior would be decreasing linewidth with increasing gain. Unfortunately, all of the observed lines have relative linewidths  $\Delta\lambda/\lambda$  on the order of  $10^{-4}$  (the gain line is  $3.5 \times 10^{-5}$  without gain narrowing), which is far less than the spectrometer limit; therefore all fully resolved lines

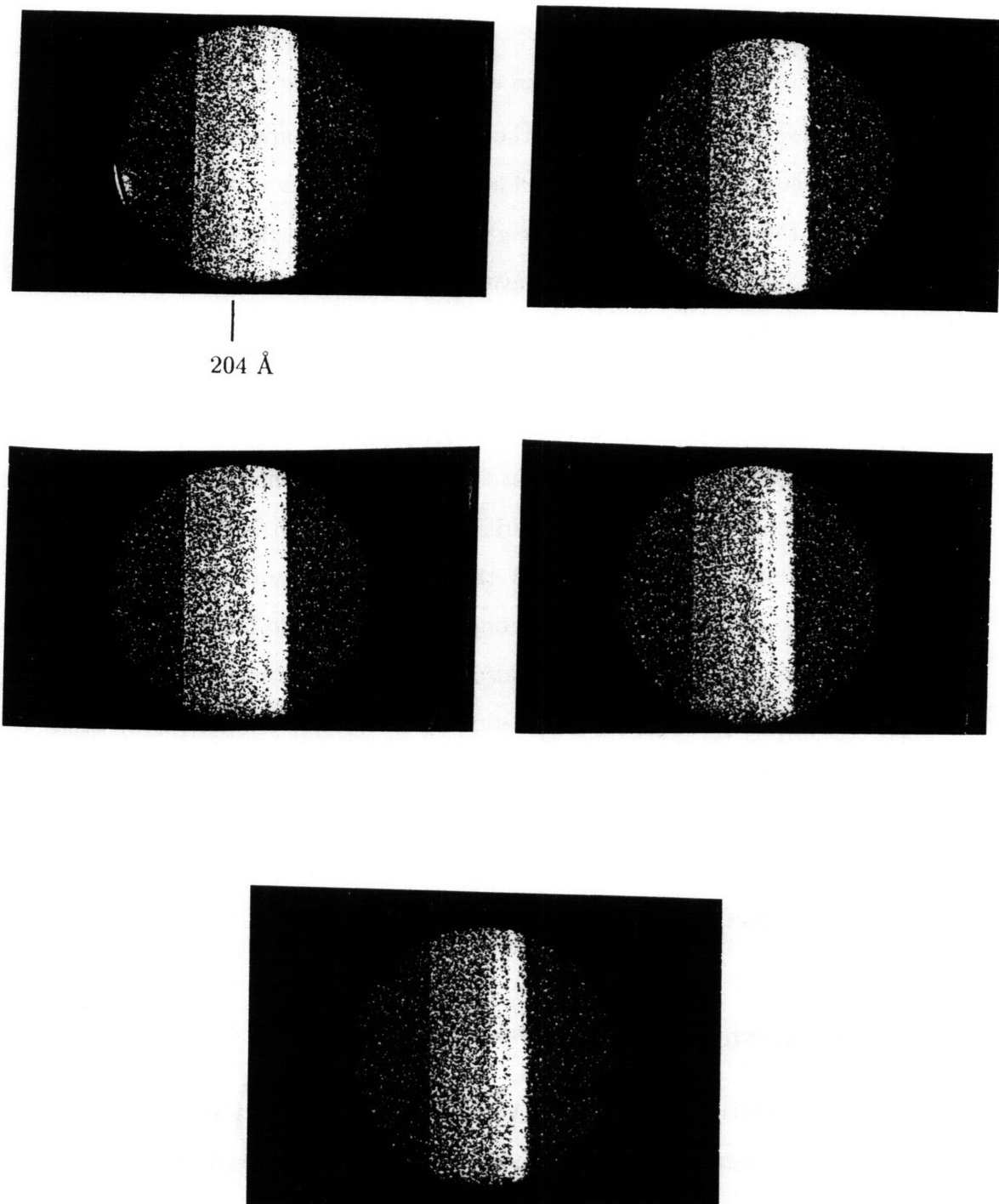


Figure 8.15: Angular behavior of streaked spectra from 0 to 40 mrad off spectrometer axis. Center: candidate gain line; on right, Cu-like lines

are expected to appear with the same width, equal to the limit.

Often, however, the gain line on the streaked images appeared wider than the spectrometer resolution limit, and also, sometimes, wider than the nearby Cu-like lines (note that in the higher-gain, corrected pictures such as in Figure 8.11, the 204 Å line appears to have about the same width as the Cu-like lines). It might be that a second line appears with the gain line; some pictures gave suggestions of a doublet with a separation of about 0.7 Å. There are no other known Ni-like lines near 204 Å, nor any lines of nearby lower-charge-state ions; also, oxygen lines were shown not to be present. Remaining possibilities include contamination by other impurities, emission from Nb ions in higher charge states, and Doppler shifting by the plasma velocity component in the direction of the spectrometer. It was conjectured that a Co-like satellite transition could be present which would also exhibit gain, as has been observed in high- $Z$  Ni-like systems [20]; calculation of the Ni-like ionization rate and time-resolved observation of the ionization balance are necessary to investigate this possibility. The broad laser linewidth remains a puzzling problem which should be resolved if the planned increase in laser power increases the gain-length product correspondingly.

## Other observations

Several other investigations were noteworthy. A series of shots was done using 120 psec rather than 60 psec pump pulses. These were at energies up to 1.5 J, yet very little suggestion of the 204 Å line could be discerned. The Cu-like emission also appeared dimmer than it did in the most recent 60-psec 1.1 J data, although the latter were at somewhat lower energy. These observations are in agreement with the calculations of Chapter 6 that predict a temperature risetime to steady state of under 60 psec, so that the temperature should be



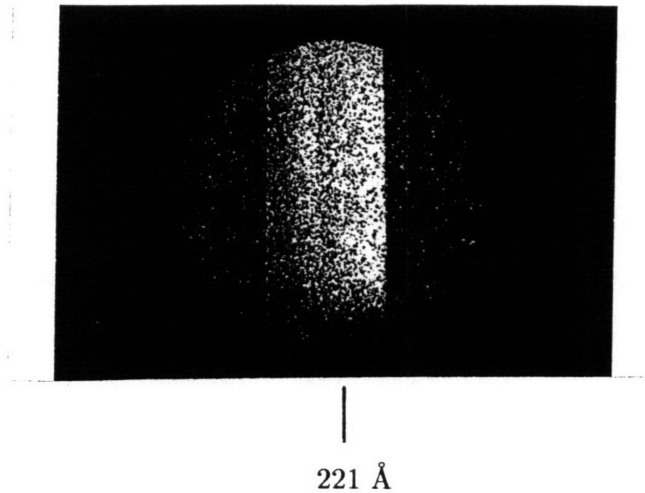


Figure 8.16: Zr spectrum near 220 Å at  $6 \times 10^{12}$  W/cm<sup>2</sup>

determined by the intensity rather than by the total energy.

The 204 Å gain line emission was observed on the third pulse as well as on the second. Both emissions were of approximately equal intensity, the only significant difference being that on the third pulse, the optimum height off the target surface moved outward to about 150 Å. This behavior is reasonable since the plasma is expected to expand outward between pulses.

A search was made for gain in the Ni-like Zr ion, for which the  $4p^1P_1-4d^1S_0$  transition is expected near 221 Å. The Cu-like reference lines at 250 Å were observed at intensities of  $6 \times 10^{12}$  W/cm<sup>2</sup>. Streak camera data for the 220 Å region showed a weak line near 221 Å (Figure 8.16). Without reference lines on the same picture, however, the spectrometer alignment could not be optimized, and precise wavelength measurements could not be made. It would be very worthwhile to reinvestigate this ion using an impurity with a simple, well-known spectrum near 220 Å to supply reference lines.

## 8.5 Discussion

In the preceding section, several features of the observed emission at 204 Å were discussed which were strongly indicative of laser gain. In some ways, observations deviated from theory: in addition to the laser linewidth problem discussed above, the required pump intensities were significantly higher than predicted, and the emissions were longer-lived than expected. These last two issues are summarized here; improved modeling and future experiments using higher powers and improved diagnostics should help greatly to resolve them.

The temporal behavior of the emission is examined first. However, the observed duration of the Cu-like emission is around 2 nsec. Assuming that temperatures of at least 50 eV are needed for these lines to radiate, we find from the model of Chapter 7 (Figure 7.15) that the expected lifetime is about 1 nsec for initial temperatures of 400 eV. Since it is unlikely that the temperature is higher than 400 eV, the model appears to be somewhat in error here; the predicted cooling rate is too high, and more detailed analyses need to be performed.

Nonetheless, the *relative* behavior of the gain line to the Cu-like lines is appropriate. If the gain line is taken to be extinguished below 140 eV and the Cu-like lines below 50 eV, then Figure 7.15 suggests that the gain lifetime should be about 1/3 that of the Cu-like lines, which is in agreement with Figure 8.14. If the 204 Å emission were a Ni-like line not demonstrating gain, it would be expected to last nearly as long as the Cu-like lines.

The high intensity required for the system to develop gain is the more serious problem. Two possibilities exist: either the achieved electron temperature is lower than suggested by calculations and modeling; or the temperature is high, and the x-ray laser scheme works well in our experimental setup only at considerably higher temperatures than predicted by the three-level model

[29].

. The first possibility would mean that in the calculations, either the pump-light absorption is taken too high or the flux-limited heat flow too low. The temperature and absorption, in this case, need to be studied more carefully, both experimentally and theoretically. The heat flow needs to be modeled more accurately, using, for example, the methods of Morgenthaler and Hagelstein [53].

The second possibility would suggest either problems in the experimental plasma conditions, such as the time behavior of the temperature and ionization balance, or an unknown atomic-physics or kinetics mechanism that would affect the predictions of the three-level model. Trapping of the laser dump transition radiation, which is greater in the present laser scheme than in higher- $Z$  collisional schemes, could be lowering the gain drastically; if this could be documented, it would be one of the first experimental verifications of significant trapping. All of these options could be examined using more sophisticated computational modeling. The experimental conditions could also be probed further using improved plasma diagnostics.



# Chapter 9

## Nonlinear x-ray conversion in plasmas

### 9.1 Introduction

In view of the increasing availability of laser sources in the soft x-ray region, it seems interesting to study nonlinear interactions at these wavelengths. One might hope to extend to this region many of the nonlinear techniques presently used in the visible: harmonic generation and frequency conversion, parametric oscillation for tunable radiation, and various interactions for spectroscopy and diagnostics. In this chapter, two published articles on short-wavelength four-wave conversion and frequency tripling are reproduced and combined [55]. These calculations were performed largely as an exercise to probe the extension of nonlinear optics to short wavelengths; also, particular schemes are described to convert the 189 Å radiation of the Ni-like Mo laser to 95 Å, and the 155 Å radiation of the Ne-like Y laser to 78 Å and to 52 Å.

Our immediate goal is to examine the use of a multiphoton process to convert soft x-ray radiation to shorter wavelengths. Conventional solid, liquid

and gaseous media are inappropriate for x-ray frequency conversion due to the relatively high degree of photoabsorption losses expected relative to the strength of any nonlinearities which are present. Such considerations suggest the use of highly stripped ions in a plasma as a nonlinear medium; the isotropy of the plasma forces us to consider only odd-order processes. The use of a plasma for short wavelength nonlinear optical conversion was proposed earlier by Harris [56]; here we examine particular schemes in order to explore whether x-ray frequency “doubling” (two x-ray photons plus one optical photon) or tripling can be demonstrated with the current generation of x-ray laser sources.

Most research on frequency conversion at low density has focused on the use of neutral gases in the visible and near UV, starting with the works of Ward and New [57] in 1969 and of Miles and Harris [58] in 1973. An excellent summary of these efforts is found in Reintjes [59]. Much of this work involved third harmonic generation, typically with the first transition nonresonant and the second or third somewhat resonantly enhanced. Conversion using a sum-difference frequency process, as we propose here, has been demonstrated in the VUV by Hilbig and Wallenstein [60] in Xe and Kr, and more recently by Marangos *et al* [61] in Kr. High conversion efficiencies and, in the latter case, wide tunabilities were obtained.

With the advent of high-power femtosecond laser systems, direct frequency conversion of optical radiation into the soft x-ray region through high-harmonic generation in gases has become feasible at modest efficiency, as was also proposed by Harris [56]. McPherson *et al* [62], for example, have demonstrated production of up to the seventeenth harmonic of 248 nm radiation in neon, and more recently Li *et al* [63] have demonstrated generation of up to the thirty-third harmonic of 1064 nm radiation in xenon.

The direct conversion of x-ray laser radiation to higher frequency is now

possible, at least in principle, given that a number of laboratories have achieved or will soon achieve saturated laser output with single-pass ASE systems. Although laser brightness is a prerequisite for x-ray frequency conversion, it is not *a priori* obvious that it is sufficient to yield a practical converter in the soft x-ray regime. There are issues of (i) smaller dipole moments for x-ray transitions in moderately stripped ions, (ii) optical phase matching in a plasma, and (iii) scattering and other loss mechanisms; such issues could prevent frequency conversion schemes which have been proven to be successful in the optical regime from extending into the soft x-ray regime.

Hence part of this chapter is devoted to a brief examination of how the proposed conversion scheme scales into the soft x-ray regime. We find that off-resonant conversion processes scale poorly to shorter wavelengths, which forces each step of the process to be near resonance to give a reasonably large susceptibility (though not so resonant as to cause absorption, of course). Third-harmonic generation will be difficult since suitable plasma systems, with four evenly-spaced dipole-connected levels (the spacing matching an x-ray laser line), will be rare.

We will consider four-wave mixing (FWM) processes of the form

$$\omega_4 = \omega_1 + \omega_2 - \omega_3,$$

where  $\omega_1$  and  $\omega_2$  are x-ray laser frequencies and  $\omega_3$  is a high-powered optical laser tuned to resonance on the final transition. The choice of a sum-difference-frequency process is made because in a plasma, this process, in contrast to sum-frequency processes, can be phase matched using noncollinearly propagating beams. The proposed scheme thus combines the benefits of readily available high power density from the optical laser, potentially very good resonance, and phase matching to reduce the required power density at the soft x-ray wavelengths and maximize the conversion efficiency.

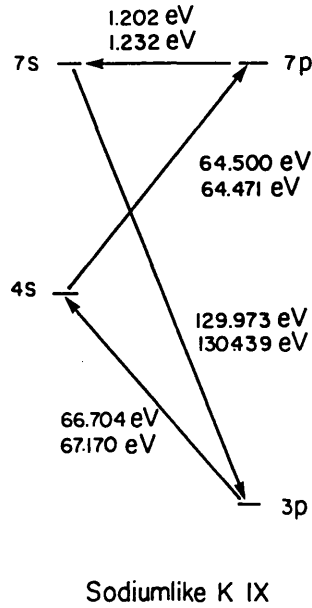


Figure 9.1: Schematic of K IX energy levels and the four-wave mixing scheme

For the FWM scheme, we examine a system where  $\omega_1 \approx \omega_2$  in the hope of being able to use just one type of x-ray laser in a  $\omega_4 = 2\omega_1 - \omega_3$  process for approximate frequency doubling. We choose to study Na-like ions for the simplicity of their level structure (i.e. the lines are known to high precision), for the high line strengths of the transitions and because the level structure is appropriate to allow  $\omega_1 \approx \omega_2 \gg \omega_3$ . Since various lasers have been demonstrated in the 60-70 eV region [3] [54] and the Ni-like Mo laser line lies in that region, we consider a scheme in Na-like K IX, illustrated in Fig. 9.1; the relevant transition energies are given by Edlén and Bodén [64]. The 3p level is assumed to have a sizeable thermal population. An x-ray photon at  $\omega_1$  (wavelength around 189 Å) polarizes the 3p – 4s transition, one at  $\omega_2$  then the 4s – 7p, and finally an optical photon at  $\omega_3$  (about 500-1000 nm) polarizes the 7p – 7s, giving rise to a new field at roughly double the original x-ray laser frequency.

The Rydberg levels 7p and 7s will give rather low oscillator strengths. For this reason it may ultimately be preferable to try the Cu-like sequence, which



would begin in an  $n = 4$  level and therefore have a more even energy spacing, allowing the use of the  $n = 5$  and  $n = 6$  levels and their higher oscillator strengths. However, the Na-like lines are better known, so we shall use them in this analysis.

We have also analyzed this FWM scheme and a third-harmonic conversion scheme in the specific context of a successful x-ray laser that has been demonstrated at LLNL, the Ne-like Y laser at 154.95 Å. For FWM, the appropriate ion is Na-like Ca. For tripling, it is Na-like V [71], and a different set of energy levels is used. The following theoretical sections will address the FWM scheme in particular, but the results are easily extrapolated to frequency tripling as well.

## 9.2 Basic equations

The multiphoton transition rates can be calculated straightforwardly using Feynman diagrams, and the results are well known [59]. The nonlinear susceptibility is

$$\begin{aligned} \chi^{(3)}(-\omega_4 : \omega_1, \omega_2, -\omega_3) &= \frac{1}{6\hbar^3} \sum \mu_{12}\mu_{23}\mu_{34}\mu_{41}\rho_{11} \\ &\times \left( \frac{1}{\omega_{21} - \omega_1 - i\Gamma_{21}} + \frac{1}{\omega_{21} - \omega_2 - i\Gamma_{21}} \right) \\ &\times \left( \frac{1}{\omega_{31} - (\omega_1 + \omega_2) - i\Gamma_{31}} \right) \\ &\times \left( \frac{1}{\omega_{41} - (\omega_1 + \omega_2 - \omega_3) - i\Gamma_{41}} \right), \quad (9.1) \end{aligned}$$

where we have retained only the resonance denominators relevant for  $\omega_1 \approx \omega_2 \gg \omega_3$ , and we have labeled the  $3p$ ,  $4s$ ,  $7p$  and  $7s$  as levels 1, 2, 3 and 4 respectively. The summation, to be rigorous, should extend over all dipole-allowed transitions through all the energy levels of the ion, but because we are near resonance at each transition, we sum over just the various allowed

pathways through the  $LS$ -split sublevels  $|nLSJM\rangle$  of each of the levels 1, 2, 3 and 4; contributions from other energy levels will be negligible. The dipole moments  $\mu_{ij} = e \hat{\mathbf{e}}_{\mathbf{k}} \cdot \langle j | \mathbf{R} | i \rangle$  (where  $\hat{\mathbf{e}}_{\mathbf{k}}$  is the polarization vector of the relevant field) and the transition frequencies  $\omega_{ji}$  are those for individual transitions from sublevels of one level to those of another. The normalized density matrix element  $\rho_{11}$  is the thermal population of the appropriate sublevel of level 1, as a fraction of the entire Na-like K population. The linewidths  $\Gamma_{ij}$  are given for a dilute plasma by  $\Gamma_{ij} = \frac{1}{2}(\gamma_i + \gamma_j)$ , where  $\gamma_i$  and  $\gamma_j$  are the natural linewidths; in a dense plasma, the lines will be collisionally broadened. For these calculations, we will not include collisional broadening explicitly (we have however evaluated the collisional linewidths in the Bethe approximation and have found typical values somewhat smaller than the thermal (Doppler-broadened) linewidths; their effect on the conversion rates we have found not to be significant until they exceed the thermal widths). Thermal broadening is taken into account by averaging  $\chi^{(3)}$  over the spectrum of appropriately weighted thermally broadened input frequencies.

The generated intensity  $I_4$  at  $\omega_4$  is now given by

$$I_4 = \frac{576\pi^4}{c^4} \omega_4^2 I_1 I_2 I_3 |\chi^{(3)}|^2 N^2 L^2 \frac{\sin^2(\Delta k L/2)}{(\Delta k L/2)^2}, \quad (9.2)$$

assuming undepleted (small signal) operation with wave vector mismatch  $\Delta k$  over an interaction distance  $L$  in a medium of number density  $N$ . In our case  $N$  represents the entire Na-like population, since the factor  $\rho_{11}$  then gives the level 1 population.

### 9.3 Scaling relations

The four-wave conversion process is understood and is known to work practically in the optical regime; in this section we are interested in how the scheme

scales into and within the EUV and soft x-ray regimes. That a scaling law can be established seems to be plausible given that the energy levels and oscillator strengths for ions are fit well along an isoelectronic sequence by a power series in an effective nuclear charge (actual nuclear charge minus a screening constant). Unfortunately, the efficiency of conversion is sensitive to the degree to which line coincidences can be found, and this factor clearly will not scale systematically with frequency or effective nuclear charge since the occurrence of resonances is for the most part random.

Nevertheless, the issue of scaling can be addressed intelligently. From inspection of (2) one can write immediately

$$I_4 \sim I_1 I_2 I_3 \omega_4^2 |\chi^{(3)}|^2. \quad (9.3)$$

For off-resonant frequency conversion, from (1), the susceptibility varies as

$$\chi^{(3)} \sim \frac{\mu_{12} \mu_{23} \mu_{34} \mu_{41}}{\Delta\omega_{21} \Delta\omega_{31} \Delta\omega_{41}}, \quad (9.4)$$

valid as long as interference effects can be ignored (see Figure 3 for a feature attributable to interference). Here the quantities  $\Delta\omega$  represent the appropriate resonance denominators from (1). Now each dipole moment scales approximately as the inverse effective nuclear charge along an isoelectronic sequence, and  $\omega_4$  scales as the square of the effective nuclear charge as long as level 1 and level 4 involve an electronic transition between orbitals which differ by at least one principle quantum number. Using these relationships, we may obtain

$$\chi^{(3)} \sim \frac{1}{\omega_4^2 \Delta\omega_{21} \Delta\omega_{31} \Delta\omega_{41}}. \quad (9.5)$$

How the detunings scale with  $\omega_4$  depends on unpredictable line coincidences; we may therefore adopt an off-resonant scaling relation which includes these features explicitly:

$$I_4 \sim I_1 I_2 I_3 \frac{1}{\omega_4^2 \Delta\omega_{21}^2 \Delta\omega_{31}^2 \Delta\omega_{41}^2}. \quad (9.6)$$

If one believes that the available detunings scale in some average sense as  $\omega_4$ , then the overall scaling is proportional to  $1/\omega_4^8$ . It is this consideration which leads us to the general conclusion that precision of line coincidences is critical for frequency conversion in the EUV; the strong dependence on  $\omega_4$  suggests that the degree of coincidence in the EUV must be better than the corresponding case in the optical regime, and must be improved even further into the soft x-ray regime.

Due to the availability of optical sources over a wide range of frequencies, it should be possible to arrange for  $\Delta\omega_{41}$  to be very small such that the resonant denominator is dominated by the linewidth factor  $\Gamma_{41}$ . Additionally, it is likely based on the results of line searches for resonances for photoexcitation-pumped EUV laser schemes that coincidences can be found for at least one of the two remaining resonances (an ion which matched both would be truly exceptional). For this case, a second detuning factor could be eliminated in favor of a linewidth factor, resulting in

$$I_4 \sim I_1 I_2 I_3 \frac{1}{\omega_4^2 \Delta\omega_{21}^2 \Gamma_{31}^2 \Gamma_{41}^2} \quad (9.7)$$

in the case that  $\Delta\omega_{31}$  was reduced. At this point, some account must be taken of the effects of Doppler broadening, the scaling of which would depend on the particulars of how the converter plasma is created. The basic point of interest in this discussion is that the scaling of the frequency conversion should be able to be improved to vary as  $\sim 1/\omega_4^4$  under the assumptions that the detuning on the remaining transition scales as  $1/\omega_4$  and that  $\Gamma_{31}$  and  $\Gamma_{41}$  scale weakly in  $\omega_4$ .

Our discussion of the scaling of the frequency conversion process would not be complete without some discussion of the intensities  $I_1$ ,  $I_2$  and  $I_3$ . Implicit in our discussion is the assumption that the intensity of the optical laser  $I_3$  can be made to be quite large, hopefully sufficiently large to yield an observable

output signal at the end of the conversion process. The limitations on  $I_1$  and on  $I_2$  are more severe, and are currently imposed by the status of the EUV and soft x-ray laser sources which have been demonstrated to date. Since very high gain amplifiers, laser cavities, multi-stage laser amplifier chains, and short pulse technology have not yet been developed in the soft x-ray regime, essentially all short wavelength sources produce a maximum output which is less than or perhaps on the order of the saturation intensity. The saturation intensity is

$$I_{sat} = \frac{\hbar}{\pi^2 c^2} \omega^3 \Delta\omega n_{sat} \quad (9.8)$$

where  $n_{sat}$  is a parameter which depends on the details of the atomic kinetics and is typically somewhat larger than but on the order of unity for all demonstrated (and quasi-steady-state) EUV and soft x-ray laser systems. Shorter wavelength lasers generally produce higher intensities by a factor of on the order of  $\omega^{7/2}$  for Doppler broadened systems.

Based on this discussion, we may conclude that the frequency converted output scales roughly as

$$I_4 \sim I_3 \frac{\omega_4^5}{\Delta\omega_{21}^2 \Gamma_{31}^2 \Gamma_{41}^2} \quad (9.9)$$

subject to the assumptions outlined above. Overall, this scaling contains an explicit  $\omega_4^3$  dependence assuming as before that the remaining mismatch in line coincidence scales as  $\omega_4$ . We may conclude then that frequency conversion with a matched optical laser ( $\omega_{41} = \omega_1 + \omega_2 + \omega_3$ ) and with one precise EUV or soft x-ray resonance appears from our simple considerations to have a nonlinear susceptibility which decreases strongly at shorter wavelengths, but that with current short wavelength laser sources operating at or above saturation the approach has an excellent chance of working throughout the EUV and soft x-ray regimes.

## 9.4 Matrix elements

We calculate the requisite dipole matrix elements for (1) from tabulated values [65] of the absorption oscillator strengths  $f_{ji}$  by finding the reduced matrix elements and applying the Wigner-Eckart theorem. For  $LS$ -coupled systems such as the alkalis, one can show by use of tensor algebra and sum rules [66] that the orbital reduced matrix elements  $\langle n_j L_j \parallel \mathbf{R} \parallel n_i L_i \rangle$  are related to the tabulated  $f_{ji}$  by

$$\left| \langle n_j L_j \parallel \mathbf{R} \parallel n_i L_i \rangle \right|^2 = \frac{3\hbar}{2m\bar{\omega}_{ji}} (2L_i + 1) f_{ji}. \quad (9.10)$$

Here  $\bar{\omega}_{ji}$  is the transition frequency, averaged over  $J_i$  and  $J_j$  with appropriate weighting factors:

$$\hbar\bar{\omega}_{ji} = \frac{1}{g_j} \sum_{J_j} (2J_j + 1) E_j^{(J_j)} - \frac{1}{g_i} \sum_{J_i} (2J_i + 1) E_i^{(J_i)}, \quad (9.11)$$

where  $E^{(J)}$  is the energy of the sublevel  $|nLSJ\rangle$ , and  $g = (2L + 1)(2S + 1)$  is the total degeneracy of the level  $|nL\rangle$ .

The signs of  $\langle n_j L_j \parallel \mathbf{R} \parallel n_i L_i \rangle$  can be found by Hartree-Fock calculations, or even from Bates and Damgaard [67]. In our case, because we are near resonance and we sum over only sublevels rather than all levels (i.e. we use only one set of four states  $|nL\rangle$ ), thus only one set of  $\langle n_j L_j \parallel \mathbf{R} \parallel n_i L_i \rangle$ , the sign contribution will be the same throughout the summation in (1) and will drop when we consider  $|\chi^{(3)}|^2$ .

The reduced matrix elements  $\langle n_j L_j S_j J_j \parallel \mathbf{R} \parallel n_i L_i S_i J_i \rangle$  are calculated from the orbital reduced matrix elements using the relation

$$\begin{aligned} & \langle n_j L_j S_j J_j \parallel \mathbf{R} \parallel n_i L_i S_i J_i \rangle \\ &= (-1)^{L_j + S_j + J_i + 1} \delta(S_i, S_j) \\ & \quad \times \sqrt{(2J_j + 1)(2J_i + 1)} \begin{Bmatrix} J_j & 1 & J_i \\ L_i & S_j & L_j \end{Bmatrix} \langle n_j L_j \parallel \mathbf{R} \parallel n_i L_i \rangle. \end{aligned} \quad (9.12)$$

	4s	7s
3p	0.38445	0.029795
7p	0.12170	12.261

Table 9.1: Orbital reduced matrix elements  $|\langle n_j L_j || \mathbf{R} || n_i L_i \rangle|$  in units of Bohr radius  $a_0$

Now the individual dipole moments are given by the Wigner-Eckart theorem,

$$\begin{aligned} \mu_{ij} &= e \langle n_j L_j S_j J_j M_j | R_\alpha | n_i L_i S_i J_i M_i \rangle \\ &= e (-1)^{J_j - M_j} \begin{pmatrix} J_j & 1 & J_i \\ -M_j & \alpha & M_i \end{pmatrix} \langle n_j L_j S_j J_j || \mathbf{R} || n_i L_i S_i J_i \rangle, \end{aligned} \quad (9.13)$$

where  $\alpha$  specifies the polarization of the interacting radiation field and must be equal to  $M_j - M_i$  to give a nonzero dipole moment. Similar calculations to those outlined above can be performed to find the matrix elements for *jj*-coupled systems.

For reference, we list in Table 9.1 the calculated values of the orbital reduced matrix elements and in Table 9.2 those of the angular factors which, when multiplied by the orbital reduced matrix elements, give the individual matrix elements.

## 9.5 Numerical evaluation for Na-like K

We now evaluate the susceptibility and converted intensity as a function of the incident frequencies. We assume unidirectional, *z*-polarized radiation fields so that only transitions involving no change in *M* occur. This and the relevant selection rules let us tabulate the allowed closed-loop transition paths through the various levels.

We have constructed a code to solve (10), (11), (12), (13), (1) and (2)

$j \rightarrow$		${}^2S_{1/2}$		${}^2P_{1/2}$		${}^2P_{3/2}$			
		$M = 1/2$	$-1/2$	$1/2$	$-1/2$	$3/2$	$1/2$	$-1/2$	$-3/2$
${}^2S_{1/2}$	$M = 1/2$	—	—	$-1/3$	$-\sqrt{2/9}$	$\sqrt{1/3}$	$\sqrt{2/9}$	$1/3$	—
	$-1/2$	—	—	$\sqrt{2/9}$	$1/3$	—	$1/3$	$\sqrt{2/9}$	$\sqrt{1/3}$
${}^2P_{1/2}$	$1/2$	$1/3$	$\sqrt{2/9}$	—	—	—	—	—	—
	$-1/2$	$-\sqrt{2/9}$	$-1/3$	—	—	—	—	—	—
${}^2P_{3/2}$	$3/2$	$\sqrt{1/3}$	—	—	—	—	—	—	—
	$1/2$	$-\sqrt{2/9}$	$1/3$	—	—	—	—	—	—
	$-1/2$	$1/3$	$-\sqrt{2/9}$	—	—	—	—	—	—
	$-3/2$	—	$\sqrt{1/3}$	—	—	—	—	—	—

Table 9.2: Angular factors for matrix elements. The matrix element  $\langle n_j L_j S_j J_j M_j | R_\alpha | n_i L_i S_i J_i M_i \rangle$  is, for  $\alpha = M_j - M_i$ , given by the product of the appropriate angular factor listed here and the appropriate orbital reduced matrix element (from Table 9.1), and is zero for  $\alpha \neq M_j - M_i$ . The index  $\alpha$  specifies the polarization of the interacting radiation field; thus for  $z$ -polarized radiation ( $\alpha = 0$ ) only those matrix elements corresponding to  $M_j = M_i$  are nonzero.



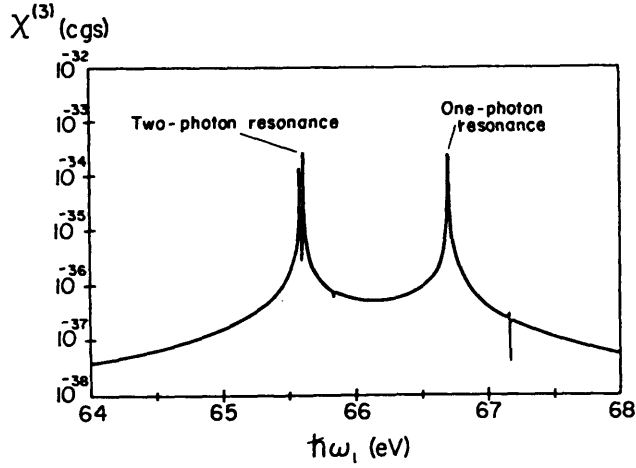


Figure 9.2: Nonlinear susceptibility for the  $\omega_4 = 2\omega_1 - \omega_3$  process as a function of  $\hbar\omega_1$ , assuming that  $2\hbar\omega_1 - \hbar\omega_3 = 129.973$  eV. The ion temperature is taken to be  $2 \times 10^5$  K in this and in the following figures.

numerically in general *LS*-coupled media. We have confirmed the accuracy of the code by reproducing results of Eicher [68], which in turn have been verified experimentally by Puell [69].

We assume an electron and ion temperature of  $2 \times 10^5$  K (20 eV), so that there is a sizeable thermal population in the  $3p$ . This temperature gives thermal linewidths of typically  $\Delta\omega/\omega \approx 10^{-4}$ , as compared to natural linewidths of about  $10^{-7}$ .

The nonlinear susceptibilities per ion in cgs units are graphed for the  $\omega_4 = 2\omega_1 - \omega_3$  process in Figure 9.2 and for the  $\omega_4 = \omega_1 + \omega_2 - \omega_3$  in Figure 9.3. In both cases  $\omega_3$  is always tuned to give exact resonance of the transition paths with  $J = 3/2$  in level 1 rather than  $J = 1/2$ , since, as can be shown from (12), the reduced matrix elements are weighted by  $\sqrt{2J+1}$ . In Figure 9.2, we simply scan  $\omega_1$ ; in Figure 9.3 we fix  $\omega_1$  at 66.50 eV, which is 0.20 eV off the one photon resonance (this seems a reasonable degree of line matching to be expected, being well in the flank of the resonance peak), and we scan  $\omega_2$ .

Both plots show intuitively reasonable behavior. A peak appears at the

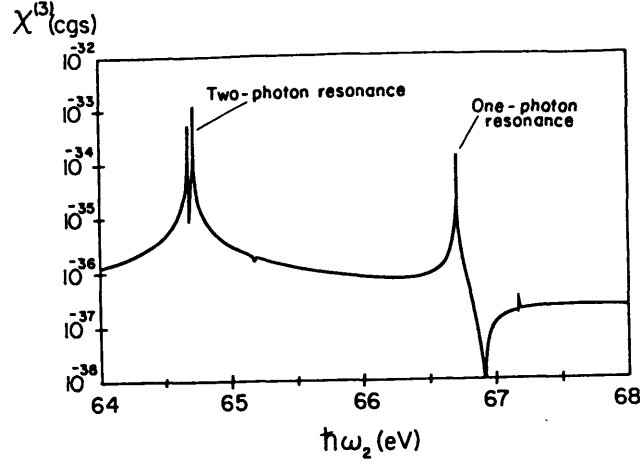


Figure 9.3: Nonlinear susceptibility for the  $\omega_4 = \omega_1 + \omega_2 - \omega_3$  process as a function of  $\hbar\omega_2$ , assuming that  $\hbar\omega_1 = 66.5$  eV and that  $\hbar\omega_1 + \hbar\omega_2 - \hbar\omega_3 = 129.973$  eV.

66.70 eV single photon resonance. Single photon absorption will, of course, limit the usefulness of this peak. Another peak occurs at the respective two-photon resonances with structures stemming from the splitting of the  $3p$  and the  $7p$ ; absorption here will not be so severe as at the single photon resonance. Also, in Figure 9.3 a strong cancellation occurs at 66.90 eV due to interference between the 66.90 eV photon and the other photon at 66.50 eV, since they straddle the 66.70 eV resonance and so contribute resonance denominators of opposite sign in (1).

The typical magnitudes of  $\chi^{(3)}$  of perhaps  $10^{-36}$ - $10^{-35}$  may be compared with the values of  $10^{-34}$ - $10^{-33}$  found by Eicher [68] and by Miles and Harris [58] for frequency tripling in sodium at visible wavelengths. Had we not matched lines closely, the scaling relation (5) would have predicted a far greater disparity between these magnitudes.

As is to be expected, the highest susceptibilities are to be obtained using two soft x-ray lasers to match the transition frequencies as best possible. The  $2\omega_1 - \omega_3$  process has a narrower two-photon peak, and the susceptibility also

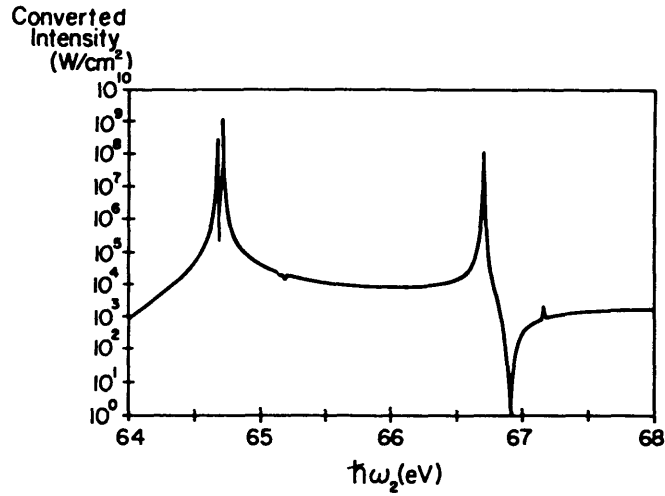


Figure 9.4: Non phase matched conversion for the  $\omega_4 = \omega_1 + \omega_2 - \omega_3$  process as a function of  $\hbar\omega_2$ , assuming that  $\hbar\omega_1 = 66.5$  eV and that  $\hbar\omega_1 + \hbar\omega_2 - \hbar\omega_3 = 129.973$  eV. The intensities for this calculation are taken to be  $I_1 = 10^{10}$  W/cm<sup>2</sup>,  $I_2 = 10^{10}$  W/cm<sup>2</sup>, and  $I_3 = 10^{12}$  W/cm<sup>2</sup>.

falls off faster to the sides. If a fortuitous line match occurred, this process would yield a high conversion without the need for two x-ray lasers. On the other hand, using two x-ray lasers would give far more flexibility in choosing a nonlinear medium and energy level scheme.

As a conversion example, we have calculated the generated intensity (2) for the  $\omega_1 + \omega_2 - \omega_3$  process using incident intensities of  $10^{10}$  W/cm<sup>2</sup> for the x-ray lasers and  $10^{12}$  W/cm<sup>2</sup> for the laser at  $\omega_3$ , and a linewidth of  $10^{-4}$  for the x-ray lasers.

For the case of nonphasematched operation, we plot the converted intensity in Figure 9.4, assuming a K IX density-interaction length product  $NL$  corresponding to  $\Delta kL = \pi$ , the point at which (2) is maximized for nonphasematched operation; this value of  $NL$  is calculated in the next section of this paper. The generated intensity appears high enough to be readily detectable as a demonstration of the effect.

We also show, in Figure 9.5, the necessary values of  $NL$  to achieve 10%

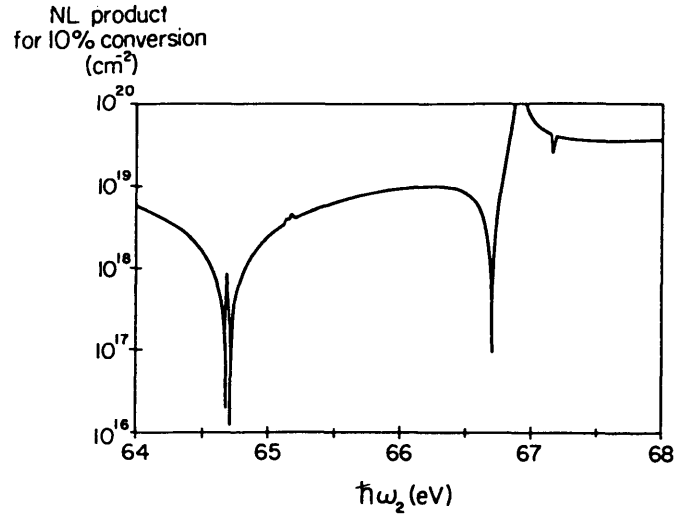


Figure 9.5: Values of  $NL$  in  $\text{cm}^{-2}$  for 10% conversion, assuming that phase matching has been achieved and that other conditions are the same as in Figure 9.4.

conversion (referenced to the total intensity from the two x-ray lasers), assuming that phase matching has been achieved so that large values of  $NL$  are accessible. These values seem reasonable for laboratory plasmas, e.g., a 1 cm cell with a K IX plasma of density  $10^{18} \text{ cm}^{-3}$  at temperature  $2 \times 10^5$  K. It should be borne in mind that we have not taken account here of collisional broadening, which will favor dilute plasmas (and consequently longer interaction distances) over denser plasmas.

## 9.6 Phase matching

Two effects influence the phase velocities of the waves: linear polarization of the ions and the dispersion by the plasma electrons. We find that, even quite near resonance, the latter effect dominates. Using

$$n(\omega) = \epsilon(\omega)^{1/2} \approx 1 - \frac{1}{2} \left( \frac{4\pi N_e e^2}{m\omega^2} \right), \quad (9.14)$$

we can show that the coherence length, which we define as the distance to the first maximum of (2), is determined mostly by the beam at  $\omega_3$  and is given

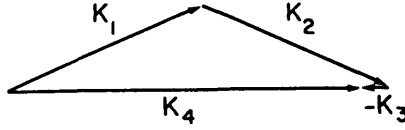


Figure 9.6: Noncollinear phase matching for  $\omega_4 = \omega_1 + \omega_2 - \omega_3$  conversion

roughly by

$$L_c = \frac{\pi}{\Delta k} \approx \frac{\lambda_3}{2(1 - n(\omega_3))} = \frac{\pi}{N_e r_e \lambda_3}, \quad (9.15)$$

where  $r_e$ , the classical electron radius, is given by  $r_e = e^2/mc^2 = 2.8179 \times 10^{-13}$ cm. So for nonphasematched operation, we find that we should choose

$$NL \leq NL_c = \frac{N}{N_e} \frac{\pi}{r_e \lambda_3}, \quad (9.16)$$

where, for Na-like K, the quantity  $N/N_e$ , the ratio of ions to free electrons, is approximately 1/8. The greatest conversion, of course, is obtained at equality in equation (16).

As can be seen from Figure 9.4, attainment of high conversion efficiency will probably require some means of active phase matching, given that the intensities used there are already quite high. Phase matching using some kind of a buffer species with a negative dispersion to counter the positive dispersion of the Na-like K is unlikely to succeed, as the positive dispersion due to the electrons will typically dominate any linear polarization.

Noncollinear phase matching, however, will succeed in this scheme (Figure 9.6). According to (14),  $n_3$  will be less than 1, and in comparison,  $n_1$ ,  $n_2$  and  $n_4$  will be essentially 1. Therefore  $k_3 + k_4 < k_1 + k_2$ , and a figure can be formed to give  $\Delta k = 0$ . The angles may be determined straightforwardly from (14) and will depend upon the electron number density. Observe that this scheme will require two separate x-ray laser beams in all cases; of course, they may be from the same type of laser or even from one single laser with a beam splitter.

The noncollinear approach will not work with sum-frequency ( $\omega_4 = \omega_1 + \omega_2 + \omega_3$ ) or tripling schemes, because the positive dispersion of the plasma makes  $k_4$  greater than the sum of  $k_1$ ,  $k_2$  and  $k_3$ , and the figure cannot be closed. For this reason, the difference-frequency process was chosen over the corresponding sum-frequency process.

## 9.7 Conversion of 155 Å laser by FWM and tripling

### Four-wave mixing in Na-like Ca

The collisionally pumped Ne-like Y laser [72] lases most strongly on the  $J = 2-1$  transition at 154.95 Å and has demonstrated a saturated output of 1-2 mJ. Focused intensities in the  $10^{14}$  W/cm<sup>2</sup> range should be achievable using reflective multilayer focusing optics currently under test at the Lawrence Livermore National Laboratory [70]. The availability of such high intensities makes this laser a promising source for investigations into nonlinear phenomena, and we are therefore examining appropriate plasma species that could give a first demonstration of a nonlinear effect.

These FWM calculations were done in the same way as described above for Na-like K, except that the x-ray laser wavelength was fixed and the optical laser wavelength was varied. The output wavelength is about 78 Å. In Figure 9.7 we plot the susceptibility as a function of the wavelength of the optical laser, with the x-ray laser wavelength fixed at 154.95 Å. We see that peaks appear at 470 nm and 617 nm: the distance between them corresponds to the *LS*-splitting of the Na-like  $3p$  level between the  $^2P_{1/2}$  and  $^2P_{3/2}$ . A strong cancellation occurs between the peaks as a result of interference.

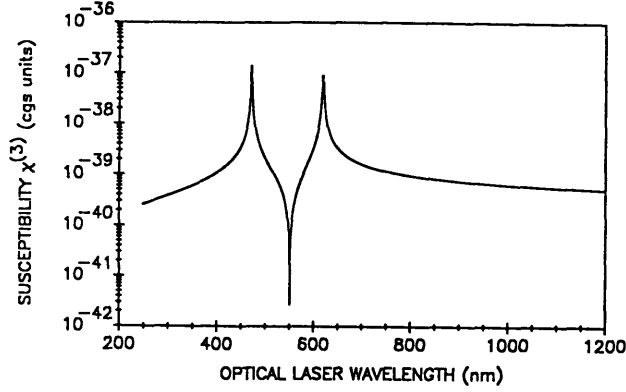


Figure 9.7: Nonlinear susceptibility for four-wave mixing as a function of optical laser wavelength. The x-ray laser wavelength is fixed at 154.95 Å and the ion and electron temperatures at  $2.5 \times 10^5$  K in this and the following figures.

We next calculate the converted intensity for collinearly propagating, linearly polarized plane-wave input beams with intensities of  $10^{14}$  W/cm<sup>2</sup> in both the x-ray laser and the optical laser, assuming no use of phase matching measures. The phase mismatch is dominated by the dispersion of the plasma electrons at the optical wavelength. We use the interaction length-ion density product that gives the peak conversion, namely that which satisfies  $\Delta kL/2 = \pi/2$ . Using  $n(\omega) = 1 - \omega_p^2/\omega^2$  gives  $NL = (N/N_e) \times (\pi/r_e\lambda_{\text{OPT}})$ , where  $N/N_e = 1/9$  for Na-like Ca, and  $r_e$ , the classical electron radius, is given by  $r_e = e^2/mc^2 = 2.8179 \times 10^{-13}$  cm. The results of this calculation are shown in Figure 9.8.

In Figure 9.9 we give the interaction length-ion density products corresponding to (1) the above-mentioned non-phase-matched peak conversion, and (2) the value required to achieve 10% intensity conversion, assuming that phase matching has been achieved.

The predicted non-phase-matched conversion is large near the resonances but small elsewhere. The failure of the resonances to match the wavelengths of

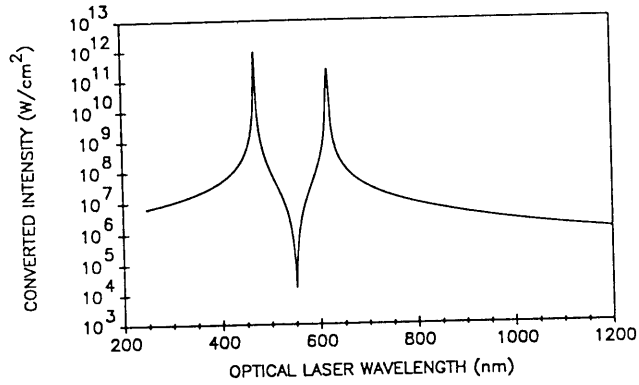


Figure 9.8: Non-phase-matched conversion as a function of optical laser wavelength, assuming that the interaction length-ion density product has been set to give maximum conversion (as plotted in Figure 9.9). The soft x-ray and optical laser intensities are taken to be  $10^{14}$  W/cm<sup>2</sup>.

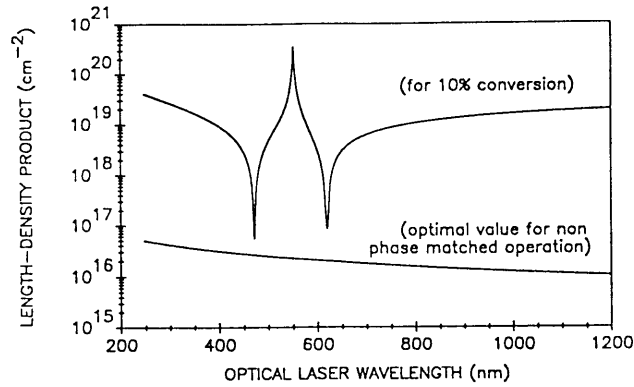


Figure 9.9: Values of length-density product for maximal non-phase-matched conversion and for 10% conversion assuming laser intensities of  $10^{14}$  W/cm<sup>2</sup> and attainment of phase matching.



the Nd: lasers and their harmonics is unfortunate; we would need to consider the use of alternative laser sources to access the required wavelengths and demonstrate the conversion experimentally.

## Frequency tripling in Na-like V

Although our work in tripling in Na-like V parallels that of Shkolnikov and Kaplan [71], we have carried it through in order to verify their result with our codes and to give a more detailed picture of the behavior of the susceptibility as a function of input wavelength in the vicinity of the 154.95 Å laser line. The ground state in this scheme is the 3*s*, and the other states are the 3*p* (very far off the one-photon resonance), the 4*s* (quite near the two-photon resonance), and the 5*p* (near the three-photon resonance). The output wavelength is 51.65 Å.

We used the same formulation and computer codes as for the four wave mixing process with the appropriate modifications for the tripling process, and the calculations are performed under the same assumptions. The energy levels are from [73] and the oscillator strengths from [65]. In Figure 9.10 we show the nonlinear susceptibility as a function of the fundamental laser wavelength. Evident are the two-photon resonance with the 4*s* state, at 153.8 Å, and the three photon resonances with the *LS*-split 5*p*, at 158.6 Å and 158.8 Å. As in the four-wave mixing scheme, a strong cancellation occurs between the *LS*-split resonances. On average the susceptibility is about an order of magnitude less than that for the four-wave mixing process.

At the Y laser wavelength of 154.95 Å, the susceptibility is  $5.785 \times 10^{-41}$  in cgs units. Because the tripling process involves only x-ray wavelengths and no optical beam, the phase mismatch is much less than for four-wave mixing, allowing the use of a higher length-density product and so increasing

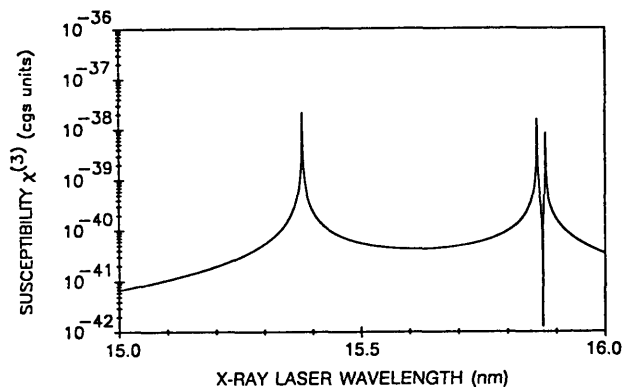


Figure 9.10: Nonlinear susceptibility for frequency tripling as a function of x-ray-laser wavelength.

the conversion. It also allows the potential use of a buffer plasma for phase matching. Shkolnikov and Kaplan [71] have found suitable buffer species for several other x-ray-laser – nonlinear medium tripling couples but none for the Ne-like Y – Na-like V couple; more searching will be necessary to find an appropriate buffer.

For peak non-phase-matched conversion, we find  $NL = 2.3 \times 10^{17} \text{ cm}^{-2}$ . This is higher than the corresponding values for four-wave mixing (compare in Figure 9.9) and roughly makes up for the lower susceptibility in the tripling. An input beam at  $10^{14} \text{ W/cm}^2$  gives rise to a converted intensity of  $1.76 \times 10^6 \text{ W/cm}^2$ . This value is still rather small for detection. For phase-matched conversion, we find that a length-density product of  $NL = 3.41 \times 10^{20} \text{ cm}^{-2}$  gives 10% conversion. This will require either a quite large interaction length or a high plasma density.

Shkolnikov and Kaplan [71] use as a benchmark a non-phase-matched conversion rate of  $10^{-8}$  and find that an input intensity of  $2 \times 10^{14} \text{ W/cm}^2$  is necessary to give this conversion, under assumptions similar to ours. Our code gives for this benchmark an intensity of  $7.5 \times 10^{13} \text{ W/cm}^2$ . We suggest that

the factor-of-three discrepancy arises from their apparent use of summed matrix elements (actually Einstein  $A$  coefficients) for each transition step rather than individual matrix elements for each possible allowed transition pathway. Nonetheless, the agreement is good to an order of magnitude.

## 9.8 Conclusion

We have proposed a four-wave conversion scheme for use in the EUV and soft x-ray regimes and have used standard methods to calculate the susceptibilities and conversions. Moreover we have explored how this scheme scales in frequency and seen that the power law depends strongly on the degree of line matching. In general the trend is unfavorable going from processes in the visible to those in the EUV; because the current ASE-type EUV lasers tend to have outputs of comparable numbers of photons per mode regardless of wavelength, however, we conclude that conversion at short EUV/soft x-ray wavelengths should be no more difficult to achieve than at longer EUV wavelengths.

For the specific case of Na-like K, we have calculated the conversion as a function of frequency. The combination of careful line matching, noncollinear phase matching, and use of a high powered optical laser in the mixing process appears to make reasonable conversion feasible.

We have also calculated conversion rates for a fixed input wavelength corresponding to that of the Ne-like Y laser. The four-wave “doubling” and the tripling rates were evaluated.

Several issues remain to be addressed: (1) incoherent losses due to absorption by the ions, which we have minimized for the first two steps of our scheme by driving the system slightly off resonance, and which can similarly be avoided on the third transition by detuning from resonance by a linewidth

or two (at a small cost in nonlinear conversion); (2) collisional broadening, which we have found not to be significant at the densities considered here, but to become relevant at higher densities; and (3) attainable interaction lengths, considering conversion using focused gaussian beams at the appropriate angles for noncollinear phase matching (which will be functions of the electron density), with the associated Rayleigh lengths and walk-off distances.

Proposed future research includes experimental and theoretical work to find suitable matches between soft x-ray laser systems and candidate nonlinear species, followed by optimization of the conversion process using a design code that accounts for the various considerations mentioned above.

# Chapter 10

## Conclusion

### 10.1 Results of this thesis

The application of the zig-zag slab laser concept to very high-peak-power laser systems has been demonstrated. The laser system constructed in this research effort exceeded virtually all its design goals.

The slab amplifier was run at repetition rates up to 0.3 Hz without significant beam quality degradation due to thermal effects. Single-pass gains up to 7.5 were measured, and the slab is run at gains of up to 6 in normal operation.

The application of techniques used in the laser-fusion field proved to be necessary to address damage and beam propagation concerns. An optical system was developed that combined apodization and relay imaging in order to deliver a near-diffraction-limited beam to the target chamber.

Theoretical efforts were undertaken that included ionization balance calculations and development of a plasma hydrodynamics model. Both of these works are helpful and relevant to the gaining of a simplified, intuitive understanding of the plasma properties and behavior in the regime of interest for x-ray lasers. The hydrodynamics model is, to our knowledge, the first analyt-

ical model to address the cooling phase of the laser-plasma expansion.

A variety of experimental spectroscopic studies were performed. Various strong indications of stimulated amplification at 204 Å were seen in Ni-like Nb. A nonlinear increase in the observed emission with increasing plasma column was observed, as was a sharply defined and relatively early turn-off time of the emission, compared with neighboring lines. Unfortunately, the available power proved insufficient to generate a large gain-length product; the planned increase in laser power addresses this problem.

A theoretical study was performed of four-wave mixing in plasmas in the 150-200 Å regime. It was shown that in spite of an unfavorable scaling of the process to shorter wavelengths, reasonable conversion efficiencies are possible if close line coincidences can be found. In the case of a known, high-power x-ray laser line near 155 Å, it was found that Na-like V has a close line match and has the potential to generate a significant conversion rate to 52 Å.

## 10.2 Future directions

### Laser system

The present laser system can be improved in two ways immediately: the peak power and the energy can be increased by chirped-pulse amplification, and the repetition rate can be increased by installation of the Nd:YLF preamplifier rod. Longer-term activities would include the construction of a greatly improved slab amplifier based on the results of the present research.

Chirped-pulse amplification has been implemented by a number of groups [74] and has considerable potential for our system. Expanding the pulses to 300 psec or more would allow the extraction of much of the stored energy in the amplifier (over 10 J per short pulse). Compressing them to about 15 psec

might give the optimal pulse duration for pumping Ni-like collisional lasers in our wavelength range. The power on each pulse would then be about 20 higher than it is presently.

Tests of the new Nd:YLF rod have been performed, and the rod appears satisfactory. It is planned for the rod to be permanently installed when the chirped-pulse amplification system is implemented. This rod will increase the repetition rate by a factor of 10.

The research and experience from this thesis have pinpointed a number of ways in which the slab amplifier design might be improved for the specific requirements of our system. Since thermal effects have been seen to be insignificant in a slab laser at our relatively low repetition rates, a much higher-gain laser glass could be used, and the slab could be made much thicker. Also, gain uniformity along the slab width need not be a high priority for systems configured as a MOPA rather than as a high-gain regen; therefore much larger flashlamps might be used. Cusped, nonimaging pump reflectors [75] could be used to transfer the flashlamp radiation efficiently to the slab. If a flooded cavity were used, the nonimaging reflector could be designed to act as a concentrator, increasing the irradiance by a factor of  $n$ . The coolant would also greatly decrease the Fresnel reflective losses during pumping and would increase the parasitic threshold, particularly if a 50/50 water/ethylene glycol mixture were used ( $n = 1.38$ ; absorption at 1053 nm about  $0.2 \text{ cm}^{-1}$ , which could be increased using an absorber if necessary). It is expected that very high single-pass gains could be achieved using these proposals, and that at a modest cost, another factor of 10 improvement in energy and intensity could be achieved in addition to the improvement from the chirped-pulse amplification.

## **X-ray lasers**

The immediate continuation to the present work will be to repeat the experiments using the upgraded laser with compressed pulses. If the current observation of about 1.5 gain lengths is correct, then the x-ray laser could be driven into saturation by the resulting power increase. Also, shorter-wavelength x-ray lasers might become accessible.

Pumping schemes that use the available power more efficiently should also be investigated. The present scheme suffers both because much of the incident radiation is reflected, and because the absorption occurs at high density, where much of the energy is transported away. Use of different pump wavelengths and pumping configurations needs to be studied analytically and experimentally.

Experiments and simulations should be also be done to study the gain dependence on the first-pulse energy and duration and the interpulse delay. It might be that an optimal first pulse should be of longer duration and lower energy than the second, in order to generate a very large, cool gain region. It will be possible with the chirped-pulse system to extract pulses either with either long or short durations. If in this way, both output pulses could be derived from one seed pulse from the oscillator, then the any interpulse delay could be used. Moreover, the Nd:YLF preamplifier rod could then be run in deep saturation and at very high output energy.

The hydrodynamics model of Chapter 7 could be expanded upon. It should be tested against more sophisticated codes in order to pinpoint weak assumptions. Any of the following changes might improve the performance of the code: (i) making the code 2-dimensional; (ii) improve the handling of the boundary condition by developing a simple analytical model of the ablation of cold mass by the hot plasma; and (iii) lift the assumption of an isothermal corona when the temperature becomes very low.



It would also be interesting to combine this hydrodynamics model with ionization-balance calculations. An average-ion model [76] might be implemented to determine the ionization balance at the beginning of the second pump pulse. The ionization-balance calculations of Chapter 6 could be improved by accounting for more levels in dielectronic recombination, by using a more accurate autoionization rate, and by repeating the calculations for the Ni-like/Co-like balance. These calculations could also be interfaced with the hydrodynamics model.

The results from this modeling must be compared to those from more complete plasma dynamics and x-ray laser codes such as LASNEX and XRASER at LLNL. This will give some guidance regarding what assumptions are reasonable to make in the simple models.

Various improvements in experimental diagnosis need to be made. The electron temperature needs to be measured more accurately. This could be done by examining closely the thresholds and time behavior of the emission spectra of various ions, and comparing the observations to accurate numerical models. Pump-light absorption should be studied experimentally and numerically. Codes need to be developed that handle heat transport more accurately, using, for example, the methods of Morgenthaler and Hagelstein [53].

The ionization balance must be determined experimentally as a function of time. To do this, the Harada spectrometer should be outfitted with a streak camera so that the 3–4 transitions can be monitored. More experiments using pairs of pump pulses spaced up to 1 nsec apart should be performed to see whether the ionization balance has been optimizing at a time when the temperature has dropped too far.

In conclusion, a high-peak-power laser system with a very high repetition rate has been demonstrated and used in x-ray laser spectroscopy and gain stud-

ies. This work enables a wide variety of future x-ray laser studies which could ultimately lead to the development of the x-ray laser as a useful laboratory tool.

# Bibliography

- [1] R. C. Elton, *X-ray lasers* (Academic Press, San Diego, 1990).
- [2] C. J. Keane, N. M. Ceglio, B. J. MacGowan, D. L. Matthews, D. G. Nilson, J. E. Trebes and D. A. Whelan, *J. Phys. B* 22, 3343 (1989).
- [3] D. L. Matthews, P. L. Hagelstein, M. D. Rosen, M. J. Eckart, N. M. Ceglio, A. U. Hazi, H. Medecker, B. J. MacGowan, J. E. Trebes, B. L. Whitten, E. M. Campbell, C. W. Hatcher, A. M. Hawryluk, R. L. Kauffman, L. D. Pleasance, G. Rambach, J. H. Scofield, G. Stone and T. A. Weaver, *Phys. Rev. Lett.* 54, 110 (1985).
- [4] W. Koechner, *Solid-state laser engineering*, 2nd ed. (Springer-Verlag, Berlin, 1988).
- [5] D. C. Brown, *High-peak-power Nd:glass laser systems* (Springer-Verlag, Berlin, 1981).
- [6] L. M. Frantz and J. S. Nodvik, *J. Appl. Phys.* 34, 2346 (1963).
- [7] Laser Program Annual Reports, Lawrence Livermore National Laboratory (NTIS, Springfield, VA, 1974-1986).
- [8] J. Swain and F. Rainer, *IEEE J. Quantum Electron.* QE-5, 385 (1969).
- [9] D. J. Kuizenga, *IEEE J. Quantum Electron.* QE-17, 1694 (1981).
- [10] A. E. Siegman, *Lasers* (University Science Books, CA, 1986).
- [11] J. H. Goncz, *J. Appl. Phys.* 36, 742 (1965).
- [12] W. S. Martin and J. P. Chernoch, U. S. Patent #3,633,126, (1972).
- [13] See, for example, M. K. Reed, PhD. thesis, G. L. #4695, Stanford University (1990).
- [14] M. Summers and J. Trenholme, private communications.

- [15] J. Eggleston, T. Kane, K. Kuhn, J. Unternahrer, and R. Byer, *IEEE J. Quantum Electron.* QE-20, 289 (1984).
- [16] *CRC Handbook of Tables for Applied Engineering Science* (CRC Press, Boca Raton, 1984).
- [17] H. R. Griem, *Plasma Spectroscopy* (McGraw Hill, New York, 1964).
- [18] I. I. Sobelman, L. A. Vainshtein, and E. A. Yukov, *Excitation of atoms and broadening of spectral lines* (Springer-Verlag, Berlin, 1981).
- [19] P. L. Hagelstein, *Phys. Rev. A* 34, 924 (1986).
- [20] B. J. MacGowan, L. B. Da Silva, D. J. Fields, C. J. Keane, S. Maxon, A. L. Osterheld, J. H. Scofield, and G. Shimkaveg, *Phys. Rev. Lett.* 65, 2374 (1990).
- [21] W. Hodge, private communication.
- [22] A. N. Zherikhin et al, *Sov. J. Quant. Electron.* 6, 82 (1976).
- [23] A. Ilyukin, G. Peregudov, E. Ragozin, I. Sobelman, and V. Chirkov, *JETP Lett.* 25, 535 (1977).
- [24] P. L. Hagelstein and S. Dalhed, *Phys. Rev. A* 37, 1357 (1988).
- [25] P. L. Hagelstein, *Proc. OSA meeting on short wavelength coherent radiation: generation and applications*, R. W. Falcone and J. Kirz, eds. (1988).
- [26] C. E. Max, *Theory of the coronal plasma in laser fusion targets* (NTIS, Springfield, VA, 1982).
- [27] P. L. Hagelstein, *Proc. SPIE 1627*, G. J. Quarles, ed. (1992).
- [28] R. D. Cowan, *The theory of atomic structure and spectra* (University of California Press, Berkeley, 1981).
- [29] P. L. Hagelstein, *Proc. SPIE 1551*, S. Suckewer, ed. (1991).
- [30] W. Kruer, *The physics of laser plasma interactions* (Addison-Wesley, Redwood City, CA, 1988).
- [31] R. Fabbro, C. Max, and E. Fabre, *Phys. Fluids* 28, 1463 (1985).
- [32] L. Spitzer, *Physics of fully ionized gases* (Wiley-Interscience, NY, 1967).

- [33] M. Rosen, P. Hagelstein, D. Matthews, E. M. Campbell, A. Hazi, B. Whitten, B. MacGowan, R. Turner, R. Lee, G. Charatis, G. Busch, C. Shepard, R. Rockett, *Phys. Rev. Lett.* 54, 106 (1985).
- [34] P. Hagelstein, J. Goodberlet, and S. Basu, unpublished.
- [35] P. Hagelstein, S. Basu, and M. Muendel, *Proc. 3rd Intl. Conf. X-ray lasers* (Schliersee, Germany, 1992).
- [36] J. Reader and N. Acquista, *J. Opt. Soc. Am.* 70, 317 (1980).
- [37] L. Golden and D. Sampson, *J. Phys. B* 13, 2645 (1980).
- [38] G. Pert, *J. Phys. B* 23, 619 (1990).
- [39] P. L. Hagelstein, *J. Phys. B* 20, 5785 (1987).
- [40] R. F. Schmalz, *Phys. Fluids* 28, 2923 (1985).
- [41] J.-F. Wyart, *Physica Scripta* 36, 234 (1987).
- [42] U. Litzen and J. Reader, *Phys. Rev. A* 36, 5159 (1987).
- [43] U. Litzen and J. Reader, *Physica Scripta* 39, 73 (1989).
- [44] U. Litzen and J. Reader, *Physica Scripta* 39, 468 (1989).
- [45] K. Rahimullah, M. S. Z. Chaghtai, and S. Khatoon, *Physica Scripta* 18, 96 (1978); also *Physica Scripta* 14, 221 (1976).
- [46] J. Reader and N. Acquista, *J. Opt. Soc. Am.* 71, 434 (1981).
- [47] M. S. Z. Chaghtai, K. Rahimullah, and S. Khatoon, *Physica Scripta* 14, 281 (1976).
- [48] J. Ekberg, J. Hansen, and J. Reader, *J. Opt. Soc. Am.* 62, 1139 (1972).
- [49] S. Basu et al, *Proc. 3rd Intl. Conf. X-ray lasers* (Schliersee, Germany, 1992).
- [50] R. Kelly, *J. Phys. Chem. Ref. Data* 16, Suppl. 1 (1987).
- [51] J. Goodberlet, S. Basu, M. Muendel, S. Kaushik, T. Savas, M. Fleury, and P. Hagelstein, submitted to *Opt. Lett.* (1994).
- [52] G. J. Linfood, E. R. Peressini, W. R. Sooy, and M. L. Spaeth, *Appl. Opt.* 13, 379 (1974).

- [53] A. W. Morgenthaler and P. L. Hagelstein, *Phys. Fluids B* 5, 1453 (1993).
- [54] S. Suckewer, C. H. Skinner, H. Milchberg, C. Keane and D. Voorhees, *Phys. Rev. Lett.* 55, 1753 (1985).
- [55] M. H. Muendel and P. L. Hagelstein, *Phys. Rev. A* 44, 7573 (1991); M. H. Muendel, P. L. Hagelstein, and L. B. Da Silva, *Appl. Opt.* 31, 4969 (1992). Also, the first paper on this topic was M. H. Muendel and P. L. Hagelstein, in *Proceedings of the International Conference on Lasers '89*, D. G. Harris and T. M. Shay, eds. (Society for Optical and Quantum Electronics, McLean, VA, 1990), p. 34.
- [56] S. E. Harris, *Phys. Rev. Lett.* 31, 341 (1973).
- [57] J. F. Ward and G. H. C. New, *Phys. Rev.* 185, 57 (1969).
- [58] R. B. Miles and S. E. Harris, *IEEE J. Quantum Electron.* QE-9, 470 (1973); also R. B. Miles, Ph.D. Thesis, Stanford University (1972).
- [59] J. F. Reintjes, *Nonlinear Optical Parametric Processes in Liquids and Gases*, Academic Press, Orlando, 1984.
- [60] R. Hilbig and R. Wallenstein, *IEEE J. Quantum Electron.* QE-19, 194 (1983); R. Hilbig, A. Lago, and R. Wallenstein, *J. Opt. Soc. Am. B* 4, 1753 (1987).
- [61] J. P. Marangos, N. Shen, H. Ma, M. H. R. Hutchinson, and J. P. Connerade, *J. Opt. Soc. Am. B* 7, 1254 (1990).
- [62] A. McPherson, G. Gibson, H. Jara, U. Johann, T. S. Luk, I. A. McIntyre, K. Boyer, and C. K. Rhodes, *J. Opt. Soc. Am. B* 4, 595 (1987).
- [63] X. Li, A. L'Huillier, M. Ferray, L. A. Lompré, and G. Mainfray, *Phys. Rev. A* 39, 5751 (1989); M. Ferray, A. L'Huillier, X. Li, L. A. Lompré, G. Mainfray, and C. Manus, *J. Phys. B* 21, L31 (1989).
- [64] B. Edlén and E. Bodén, *Physica Scripta* 14, 31 (1976).
- [65] E. Biémont, *Astron. Astrophys. Suppl.* 31, 285 (1978).
- [66] M. Weissbluth, *Atoms and Molecules*, Academic Press, New York, 1978.
- [67] D. R. Bates and A. Damgaard, *Phil. Trans. Roy. Soc. London A*242, 101 (1949); note sign correction by H. B. Bebb, *Phys. Rev.* 149, 25 (1966).
- [68] H. Eicher, *IEEE J. Quantum Electron.* QE-11, 121 (1975).

- [69] H. Puell et al, Phys. Rev. A 14, 2240 (1976).
- [70] L. B. Da Silva, M. H. Muendel, R. W. Falcone, D. J. Fields, J. B. Kortwright, B. J. MacGowan, D. L. Matthews, S. Mrowka, G. M. Shimkaveg, and J. E. Trebes, in *X-ray lasers 1990*, G. J. Tallents, ed. (Institute of Physics, Bristol, England, 1991), p. 177.
- [71] P. L. Shkolnikov and A. E. Kaplan, Opt. Lett. 16, 1973 (1991).
- [72] B. J. MacGowan, J. L. Bourgade, P. Combis, C. J. Keane, R. A. London, M. Louis-Jacquet, D. L. Matthews, S. Maxon, D. Naccache, M. D. Rosen, G. Thiell, and D. A. Whelan, in *Short Wavelength Coherent Radiation: Generation and Applications*, volume 2, R. W. Falcone and J. Kirz, eds. (Optical Society of America, Washington, DC, 1988), p. 2.
- [73] L. Cohen and W. E. Behring, J. Opt. Soc. Am. 66, 899 (1976).
- [74] D. Strickland and G. Mourou, Opt. Comm. 56, 219 (1985).
- [75] A. Rabl, Appl. Opt. 15, 1871 (1976).
- [76] S. Chandrasekhar, *An introduction to the study of stellar structure* (University of Chicago, Chicago, 1939); also D. Post et al, Atom. Data and Nuc. Data Tables 20, 434 (1977).





# Appendix A

## Flashlamp driver circuit schematics

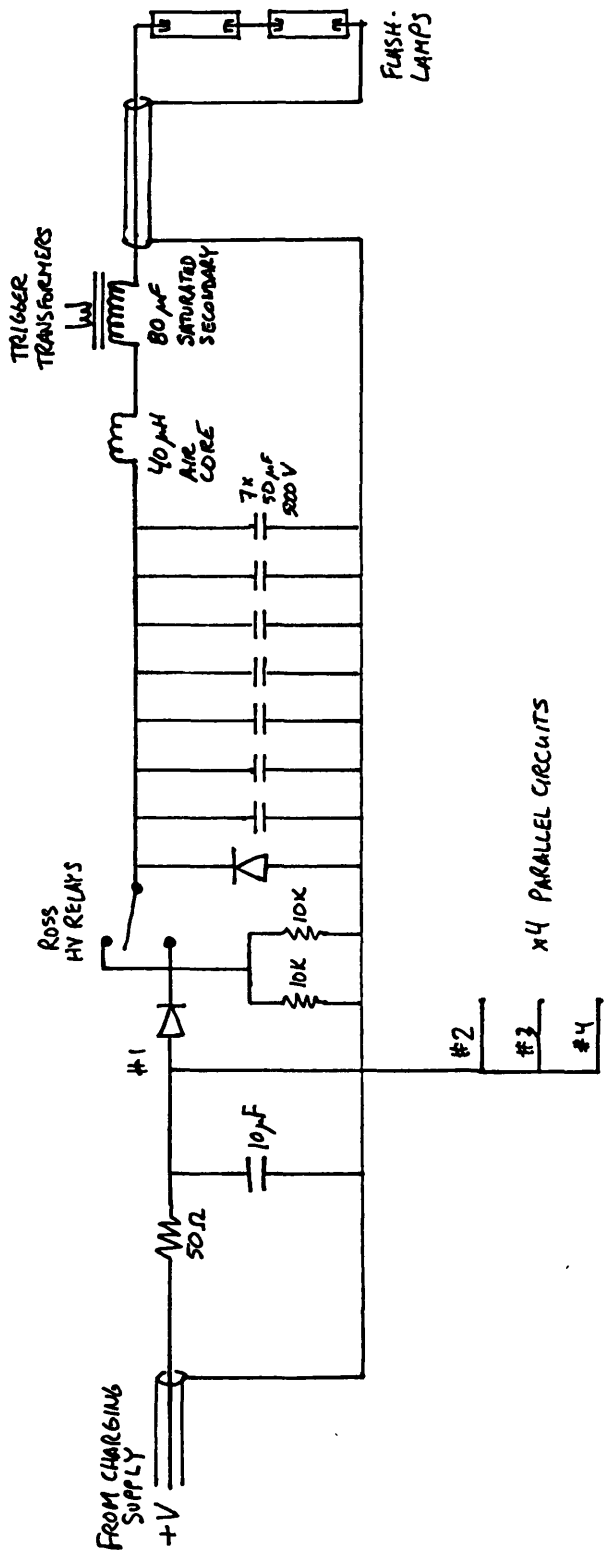
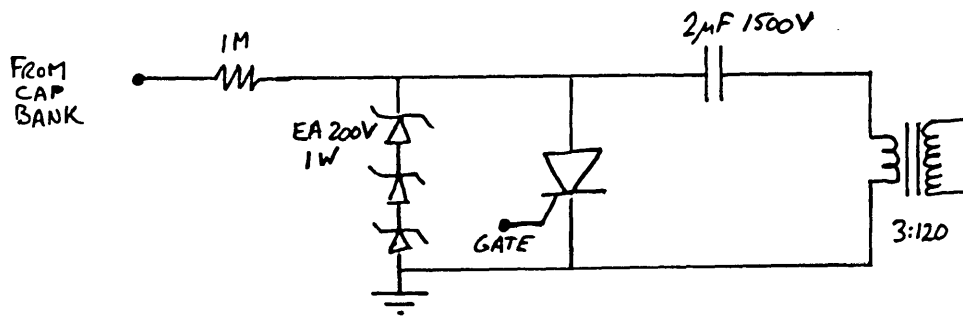
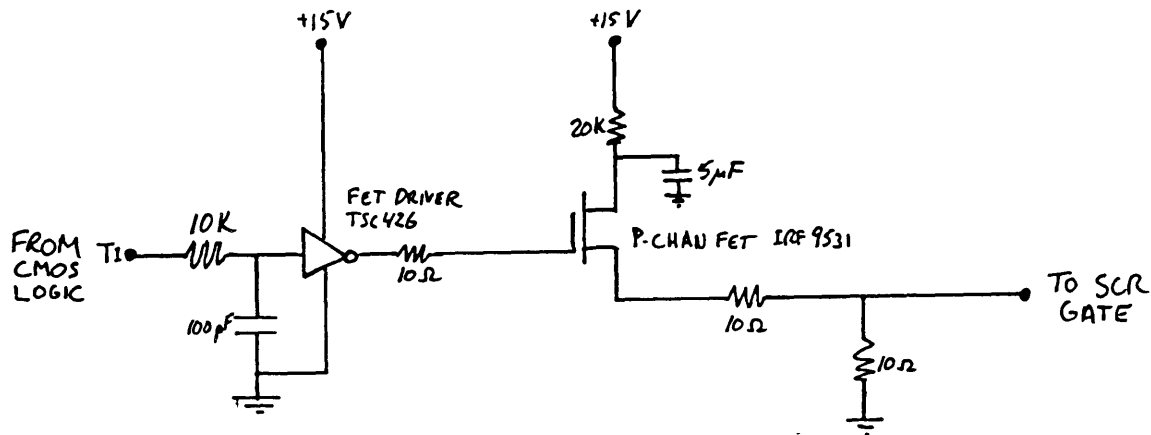


Figure A.1: Main driver circuits. The system is presently configured for two of these circuits, connected to capacitor banks #2 and #4.



TRANSFORMER PRIMARY COIL CIRCUITS (4)



SCR GATE DRIVER CIRCUITS (4)

Figure A.2: Trigger circuits

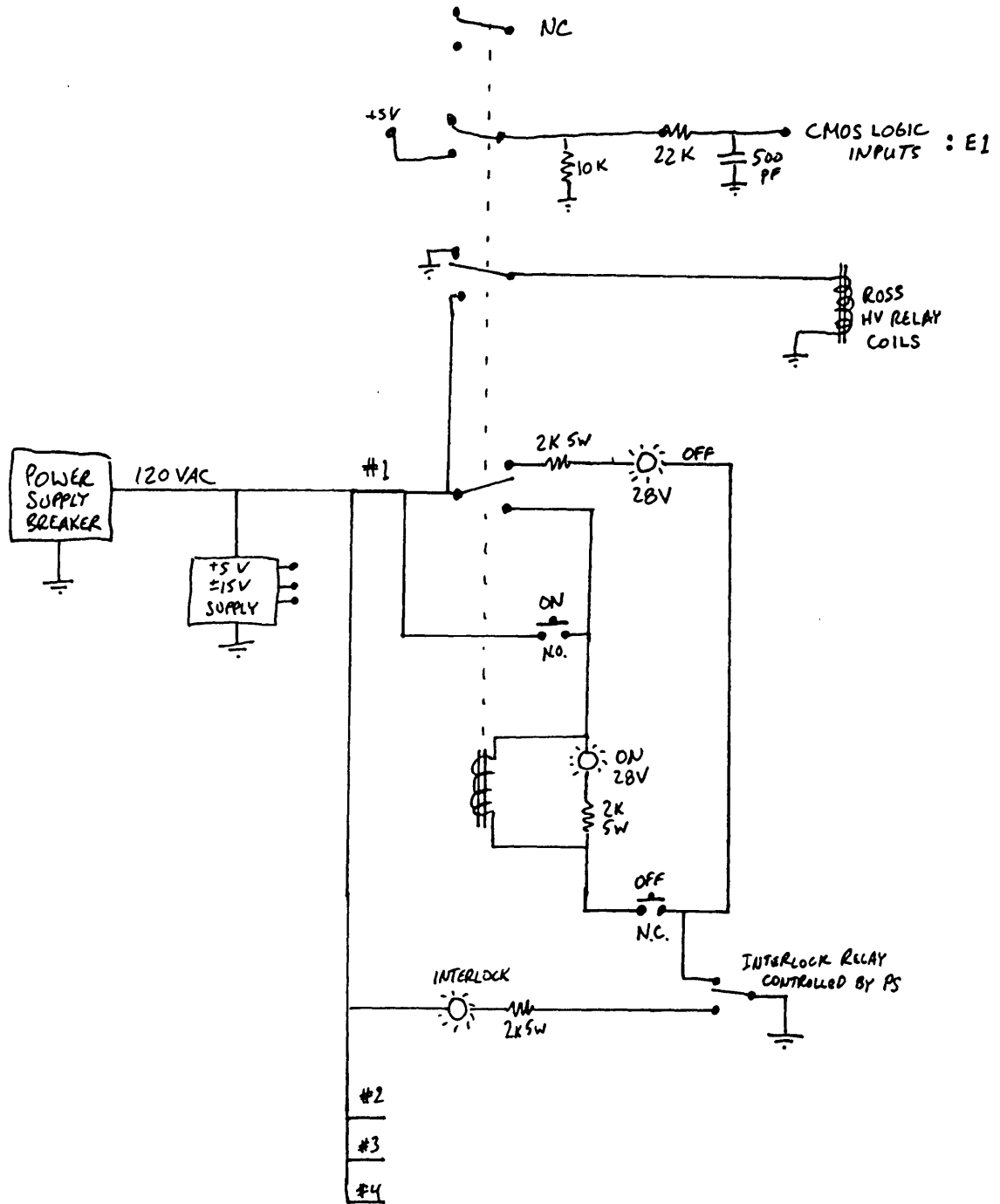


Figure A.3: Relay logic

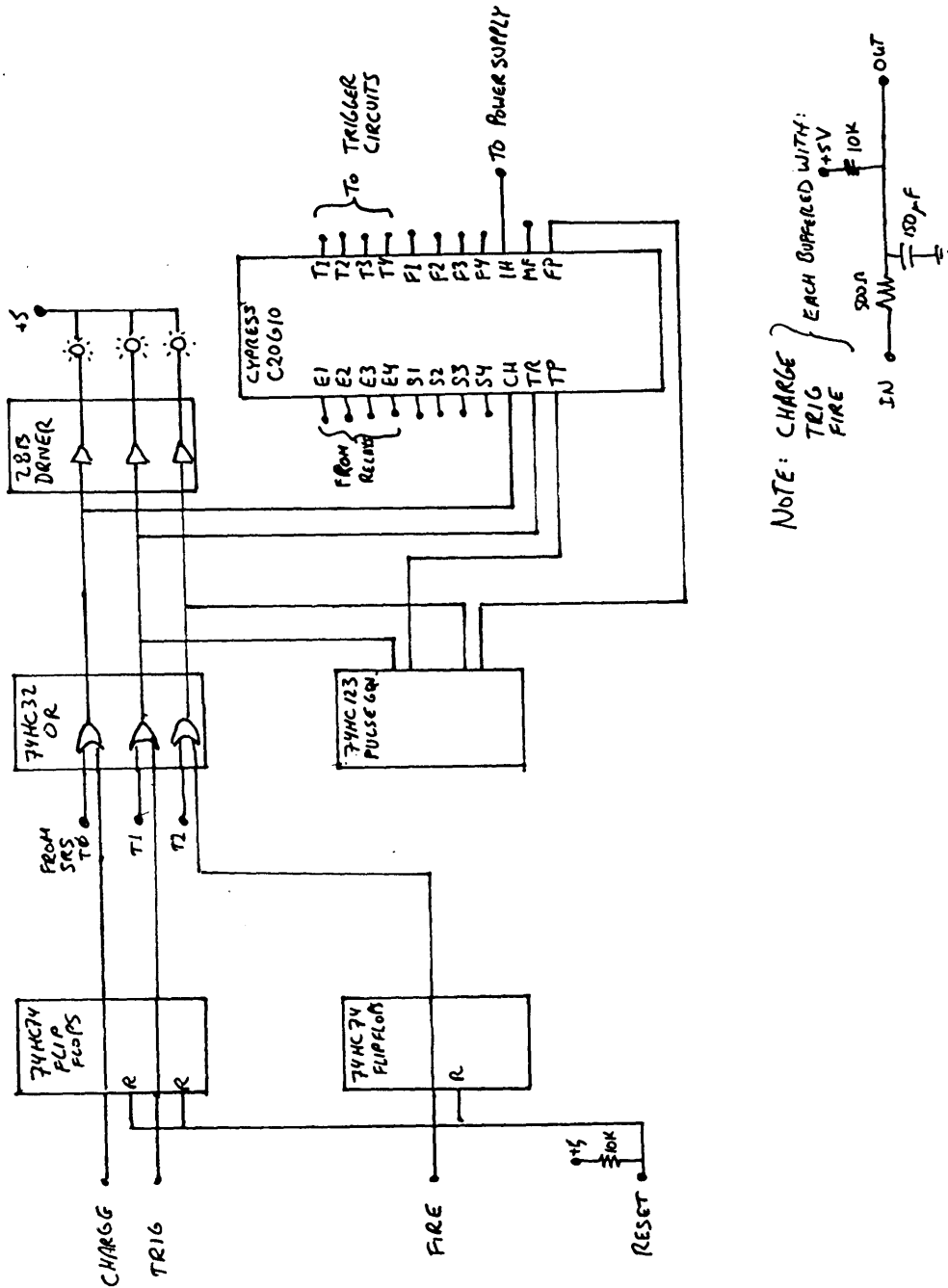


Figure A.4: Digital command logic

```

C20G10;

CONFIGURE;
E1, E2, E3, E4, S1, S2, S3, S4, CH, TR, TP, FP(node=13),
MF(ninv,noreg), IH(ninv,noreg),
F4(ninv,noreg), F3(ninv,noreg), F2(ninv,noreg), F1(ninv,noreg),
T4(ninv,noreg), T3(ninv,noreg), T2(ninv,noreg), T1(ninv,noreg);

EQUATIONS;
MF = <oe>
    <sum> !S1 * !S2 * !S3 * !S4
      + !FP;
IH = <oe>
    <sum> !E1 * !E2 * !E3 * !E4
      + !CH
      + TR;
F4 = <oe>
    <sum> !S1 * !S2 * !S3 * !S4 * FP * E4;
F3 = <oe>
    <sum> !S1 * !S2 * !S3 * !S4 * FP * E3;
F2 = <oe>
    <sum> !S1 * !S2 * !S3 * !S4 * FP * E2;
F1 = <oe>
    <sum> !S1 * !S2 * !S3 * !S4 * FP * E1;
T4 = <oe>
    <sum> TP * E4;
T3 = <oe>
    <sum> TP * E3;
T2 = <oe>
    <sum> TP * E2;
T1 = <oe>
    <sum> TP * E1;

```

Figure A.5: Program for Cypress PLD C 20G10

## Biographical note

Martin H. Muendel was born on July 13, 1964 in Wilmington, Delaware. He graduated from the Alexis I. du Pont High School in Greenville, Delaware, in 1982. From 1982 to 1986, he attended Princeton University, where he majored in physics, rowed on the varsity heavyweight crew, and graduated *summa cum laude*. He was awarded the Class of 1916 Cup (scholar-athlete prize) by the university and the Kusaka Memorial Thesis Prize by the physics department for his senior thesis, "Atmospheric emission and absorption in the 90 GHz range."

He spent the following year on a Fulbright scholarship at the Max Planck Institute for Quantum Optics in Munich, Germany, where he worked in the laboratories of Professor Herbert Walther on high power Nd:YAG lasers and generation of squeezed-state radiation. He commenced study at MIT on an NSF graduate fellowship and was subsequently awarded a Newport Corporation scholarship and a SPIE optical engineering scholarship. In the course of his thesis research, he spent about 15 months with the Laser Program at the Lawrence Livermore National Laboratory constructing a high power Nd:glass laser system. He also served as a class instructor for the MIT freshman physics course and the MIT junior physics laboratory course.

His work experience includes summer employment in the D Division (operations research) of the Lawrence Livermore National Laboratory and in the Space Physics and Astrophysics section of the Jet Propulsion Laboratory, as well as seasonal employment with the National Outdoor Leadership School in Lander, Wyoming, as a mountaineering instructor. He is a member of the Phi Beta Kappa and Sigma Xi societies and of the OSA and SPIE, and is an avid rower, mountaineer, and classical musician.

